SYNTHESIS AND STRUCTURAL STUDIES OF

MALARIA PIGMENT MODEL SYSTEMS

Ratchadaporn Puntharod

A Thesis Submitted in Partial Fulfillment of the Requirements for the

Degree of Doctor of Philosophy in Chemistry

Suranaree University of Technology

Academic Year 2008

การสังเคราะห์และศึกษาโครงสร้างของระบบแบบจำลองสารสีมาลาเรีย

นางสาวรัชดาภรณ์ ปันทะรส

รัชดาภรณ์ ปันทะรส : การสังเคราะห์และศึกษาโครงสร้างของระบบแบบจำลองสารสี
มาลาเรีย. (SYNTHESIS AND STRUCTURAL STUDIES OF MALARIA
PIGMENT MODEL SYSTEMS) อาจารย์ที่ปรึกษา : รองศาสตราจารย์ ดร. เค็นเนท
เจ. แฮลเลอร์, 159 หน้า.

การวิจัยหาโครงสร้างที่แน่นอนและการศึกษาความสัมพันธ์ทางโครงสร้างและสมบัติของ
สารสีมาลาเรียยังไม่ปรากฏถึงคำอธิบายที่ชัดเจนมามากกว่าศตวรรษ งานวิจัยนี้รายงานถึงการ
สังเคราะห์เบตาเฮมาทินเป็นครั้งแรกโดยการทำให้เป็นกรดด้วยกรดแอซีติกเข้มข้น เบตาเฮมาทินซึ่ง
ประกอบด้วยกลุ่มฮีมโพรโทพอร์ไฟรินเก้าเช่นเดียวกับสารสีมาลาเรียซึ่งสารนี้ไม่มีความแตกต่าง
กับเบตาเฮมาทินเมื่อวิเคราะห์ด้วยเทคนิคสเปกโทรสโกปีและเทคนิคการวัดกระเจิงรังสีเอกซ์แบบ
ผลึกผง อย่างไรก็ตาม งานวิจัยนี้ยังไม่สามารถเตรียมผลึกผลิตภัณฑ์ให้มีขนาดที่เหมาะสมสำหรับ
การหาลักษณะเฉพาะโครงสร้างด้วยรังสีเอกซ์ผลึกเชิงเดี่ยว ดังนั้น เพื่อเป็นการศึกษาโครงสร้างที่ยัง
ไม่ชัดเจนของสารสีมาลาเรีย จึงศึกษาระบบแบบจำลองฮีมชีวอนินทรีย์ 5 ชนิดซึ่งอาศัยพื้นฐานของ
เตตระฟีนิลพอร์ไฟรินและออกตะเอธิลพอร์ไฟรินสังเคราะห์ ได้แก่ เตตระฟีนิลพอร์ไฟรินเหล็ก
(III) คลอไรด์ มิวออกโซเตตระฟีนิลพอร์ไฟรินเหล็ก(III) คลอไรด์ ออกตะเอธิลพอร์ไฟรินเหล็ก
(III) คลอไรด์ มิวออกโซออกตะเอธิลพอร์ไฟรินเหล็ก(III) และออกตะเอธิลพอร์ไฟรินเหล็ก(III)
พิกรต จึงถูกสังเคราะห์ขึ้น สารประกอบเชิงซ้อนที่เป็นแบบจำลองมีลักษณะโมเลกุลสารสัมพันธ์ที่
เป็นส่วนสำคัญของสารสีมาลาเรีย (และเบตาเฮมาทิน) โดยสารประกอบเชิงซ้อนทั้งหมดมี
โคออร์ดิเนตเท่ากับห้า รูปร่างโมเลกุลชนิดพีระมิดฐานสี่เหลี่ยม และเหล็กอยู่ในสภาวะสปินสูงของ
สารประกอบเชิงซ้อนเหล็ก(III)พอร์ไฟริน จากการเปรียบเทียบรูปแบบการกระตุ้นของแถบรามาน
ของแบบจำลองสารสีมาลาเรีย พบว่า มีเพียงมิวออกโซออกตะเอธิลพอร์ไฟรินเหล็ก(III) เท่านั้นไม่
ปรากฏสัญญาณการเพิ่มขึ้นของโหมดสมมาตรทั้งหมด ν_4 เมื่อกระตุ้นด้วยรังสีอินฟราเรดย่านใกล้

เมื่อศึกษาเปรียบเทียบอย่างละเอียดของโครงสร้างผลึกเชิงเดี่ยวของคลอโรมอนอเมอร์ และ
มิวออกโซไดเมอร์ สามารถระบุได้ว่า ไม่มีความแตกต่างในเชิงโครงสร้างโมเลกุลฮีมจำลองอย่างมี
นัยสำคัญ อย่างไรก็ตาม พบว่ามิวออกโซออกตะเอธิลพอร์ไฟรินเหล็ก(III) มีอัตรกิริยาที่อ่อนกว่า
เมื่อเปรียบเทียบกับแบบจำลองตัวอื่นๆ ดังนั้น ความเข้มของ ν_4 มีอิทธิพลรุนแรงต่อพันธะ
ไฮโดรเจน C—H···X (เมื่อ X เป็น π และคลอโร) ซึ่งเป็นพันธะทั่วไปในระบบโอลิโกเมอริกที่
แสดงหน้าที่สำคัญในอัตรกิริยาการกระตุ้น ที่สามารถเกิดขึ้นในระบบฮีมที่อยู่ด้วยกันเป็นจำนวน
มาก ความเข้มของโหมด ν_4 เพิ่มขึ้นเป็นผลจากการคู่ควบของการกระตุ้นในฮีมที่ขยายต่อๆ กันไป
ผ่านอัตรกิริยาที่แข็งแรงหรืออัตรกิริยาที่อ่อน ทำให้การเพิ่มขึ้นของโหมด ν_4 ที่ย่านใกล้อินฟราเรด

ใช้เป็นตัวบ่งชี้ของอัตรกิริยาซุปราโมเลกุลาร์ของฮีมที่อยู่รวมกัน มากไปกว่านั้นความเข้มสัมพันธ์ของ V_4 อาจเป็นตัวบ่งชี้ความแข็งแรงของกลุ่มอัตรกิริยาซุปราโมเลกุลาร์ในระบบฮีม ออกตะเอธิลพอร์ไฟรินเหล็ก(III) พิเกรต แสดงแถบสัญญาณเฉพาะเมื่อฮีมถูกแทนที่ที่ตำแหน่งเบตา โดยรูปแบบการเพิ่มขึ้นของสัญญาณรามานคล้ายคลึงกับเบตาเฮมาทินหรือสารสีมาลาเรียเมื่อเปลี่ยนความยาวคลื่นแสงที่กระตุ้น จึงแสดงได้ว่าทั้งออกตะเอธิลพอร์ไฟรินเหล็ก(III) พิเกรต และเบตาเฮมาทินมีโครโมฟอร์ที่เหมือนกันและการจัดเรียงอิเล็กตรอนที่คล้ายคลึงกัน และให้แนวคิดที่ว่าความแข็งแรงของอัตรกิริยาซุปราของสารประกอบทั้งสองนี้คล้ายกัน ผลลัพธ์เหล่านี้เป็นส่วนที่ตรงกันกับเบตาเฮมาทินมีพันธะไฮโดรเจนที่แข็งแรง ซึ่งมีประสิทธิภาพในสนับสนุนการเพิ่มขึ้นของโหมด V_4 ผ่านกลไกการกระตุ้นคู่ควบซุปราโมเลกุลาร์

นี่เป็นครั้งแรกที่พันธะไฮโดรเจนเป็นสาเหตุโดยนัยของการเพิ่มขึ้นของเรโซแนนซ์รามานผ่านโดยกลไกการกระตุ้นคู่ควบ และอาจเป็นแนวคิดที่สำคัญในการออกแบบและติดตามยาต้านมาลาเรียที่ถูกออกแบบเพื่อไปรบกวนพันธะไฮโดรเจนในขั้นการเกิดเฮโมโซอิน มากไปกว่านั้นการค้นพบความสำคัญของพันธะไฮโดรเจนที่มีบทบาทในการเคลื่อนย้ายอิเล็กตรอนในกลุ่มฮีมซุปราโมเลกุลาร์ จะเป็นหนทางไปข้างหน้าของการพัฒนาของเครื่องมือลวดนาโนฮีมและเครื่องรับรู้การเคลื่อนย้ายโฟตอนในช่วงอินฟราเรดย่านใกล้

สาขาวิชาเคมี   ลายมือชื่อนักศึกษา_____

ปีการศึกษา 2551   ลายมือชื่ออาจารย์ที่ปรึกษา_____

RATCHADAPORN PUNTHAROD : SYNTHESIS AND STRUCTURAL STUDIES OF MALARIA PIGMENT MODEL SYSTEMS. THESIS ADVISOR : ASSOC. PROF. KENNETH J. HALLER, Ph.D. 159 PP.

MALARIA/IRON(III) PORPHYRIN/RESONANCE RAMAN ENHANCEMENT/ HEME/SUPRAMOLECULAR INTERACTION

After more than a century of research the precise structure and the relationship between the structure and properties of malaria pigment remain somewhat elusive. This work reports the first hydrothermal synthesis of β-hematin, which contains the same protoporphyrin IX heme group and is indistinguishable from malaria pigment by spectroscopic and X-ray powder diffraction techniques, by glacial acetic acid acidification. Unfortunately, the size of the product crystals is not sufficient for single crystal X-ray structural characterization. To circumvent the structural dilemma, the bioinorganic heme model systems, Fe(TPP)Cl, [Fe(TPP)]$_2$O, Fe(OEP)Cl, [Fe(OEP)]$_2$O, and Fe(OEP)picrate, based on synthetic tetraphenyl- (TPP) and octaethyl-porphyrin (OEP) were studied. The model complexes share the key molecular stereochemical features of malaria pigment (and β-hematin): all are five-coordinate, square-pyramidal, high-spin, iron(III) hemes. Excitation profiles for Raman bands of the malaria pigment models were compared. Only [Fe(OEP)]$_2$O does not show the enhancement of the totally symmetric mode ν_4 at near-IR excitation.

Detailed comparison of the single crystal X-ray structures of the chloro monomers and μ-oxo dimers indicates no significant differences in the molecular geometry of the hemes, but shows that [Fe(OEP)]$_2$O contains less (weaker) intermolecular interactions in

comparison to the other species. Thus, ν_4 intensity is strongly affected by C–H···X hydrogen bonding interactions (X: π, chloro) which in addition to conventional bonds in an oligomeric system play an integral role in enabling excitonic interactions to occur in aggregated heme systems. The enhancement results from excitonic coupling in the extended heme aggregate through either strong or concerted-weak intermolecular interactions, allowing enhancement of ν_4 at near-IR excitation to be used as an indicator of the supramolecular interactions in heme aggregates. Moreover the relative intensity of ν_4 may be an indicator of the strength of concerted supramolecular interactions in heme systems. Fe(OEP)picrate exhibits the characteristic bands assigned to *beta* substituted hemes, and also a Raman enhancement profile similar to β-hematin or malaria pigment on turning the excitation wavelengths, showing them to have the same chromophore and similar electronic structure, and suggesting that the strength of supramolecular interaction of the compounds are similar. These results are consistent with the strong hydrogen bonds in β-hematin being sufficient to support ν_4 enhancements via the supramolecular excitonic coupling mechanism.

This is the first time that hydrogen bonds have been implicated in causing resonance Raman enhancement via the excitonic coupling mechanism. This may have important implications in the design and monitoring of antimalarial drugs designed to disrupt hydrogen bond interaction in the hemozoin formation step. Moreover the discovery of the importance of hydrogen bonding interactions play in energy transfer in heme supramolecular aggregates may pave the way forward to the development of nano-wire heme based assemblies and other near-IR photon transfer sensors.

School of Chemistry   Student's Signature _____

Academic Year 2008   Advisor's Signature _____

ACKNOWLEDGEMENTS

Ratchadaporn Puntharod

CONTENTS

CONTENTS (Continued)

CONTENTS (Continued)

LIST OF TABLES

LIST OF TABLES (Continued)

LIST OF TABLES (Continued)

LIST OF FIGURES

LIST OF FIGURES (Continued)

LIST OF FIGURES (Continued)

LIST OF ABBREVIATIONS

Å	Angstrom
θ	Bragg angle or scattering angle
k	Boltzmann constant
°C	degrees celsius
ρ	electron density
ΔE_Q	quadrupole splitting (QS)
J	rotation quantum number
λ	spin orbit coupling constant
h	Plank's constant (6.626×10^{-34} J s)
S	total spin
T	temperature
$\bar{\lambda}$	wavelength of X-radiation
υ	wavenumbers
Θ	Weiss constant
α, β, γ	unit cell angles
a, b, c	unit cell dimensions
$U[\quad]$	isotropic atomic displacement parameter for the indicated atom
Z	number of formula units in the unit cell or
%	percentage
B3LYP	Becke, three-parameter, Lee-Yang-Parr
calcd	calculated

LIST OF ABBREVIATIONS (Continued)

cm^{-1}	wavenumber (per centimeter)
D	density
DNA	deoxyribonucleic acid
DPDE	3,7,12,17-tetramethylporphyrin-2-18-dipropionic acid
eV	electron voltage
EXAFS	Extended X-ray absorption fine structure
kV	kilovolt
hr	hour
g	gram
K	Kelvin
L	Litre
m^{-3}	per cubic meter
mg	milligram
mA	milliampare
min	minute
mL	milliliter
mmol	millimole
mM	millimolar
mW	millwatt
M.W.	molecular weight
nm	nanometer
No.	number

LIST OF ABBREVIATIONS (Continued)

OEP	2,3,7,8,12,13,17,18-octaethylporphyrin
Pa	Pascal
PPIX	3,8,13,17-tetramethyl-7,12-divinylporphyrin-2,18 dipropionic acid
pyr	pyrrole
rpm	round per minute
sec	second
TPP	2,5,10,15-tetraphenylporphyrin
μm	micrometer
μmol	micromole

CHAPTER I

INTRODUCTION

The chemistry of metalloporphyrins is interesting, partly because these complexes are the key components of systems that perform critical biological functions such as oxygen transport and storage (hemoglobins/myoglobins), oxygen reduction (terminal heme/copper oxidases), electron transfer (b- and c-type cytochromes), monooxygenation (P_{450} cytochromes), and peroxide/superoxide scavenging (catalases and peroxidases), and they are also the key components in light-harvesting dyads. Moreover, they form a diverse class of molecules capable of catalyzing a wide range of chemical processes including oxidations, peroxide degradation, hydroxylation (Kosal, Chou, Wilson, and Suslick, 2002), and electron transport (Mikšovská, Norstrom, and Larsen, 2005). Metalloporphyrins have been inhibitors to β-hematin (hemozoin) formation (Cole, Ziegler, Evans, and Wright, 2000), fabricated into photovoltaic cells (Kim, Kim, Ha, and Lee, 2001) and tested for medical applications such as anticancer agents (Kasugai, Murase, Ohse, Nagaoka, Kawakami, and Kubota, 2002).

Complex metalloporphyrins such as hemoglobin, vitamin B_{12}, and chlorophyll are found in nature, and a large number of simpler derivatives have been synthesized and reported by several authors. Some metalloporphyrins have been used to provide models, which mimic functions of heme proteins, heme enzymes, and the supramolecular assembly of chlorophyll in green plants and photosynthetic bacteria

(Kadish, Smith, and Guilard, 2000). β-hematin, a synthetic metalloporphyrin, is used as a model to understand the structure of malaria pigment, hemozoin, in living cells.

Malaria is one of the most important infectious diseases in the world. The mortality from malaria appears to be increasing in the highest risk groups particularly in African children (Rosenthal, 2003). Although malaria incidence is mostly centered in tropical regions, the impacts, especially economic, of the disease are global (Tekwani and Walker, 2005). There are four species that infect humans, *Plasmodium falciparum, Plasmodium vivax, Plasmodium malariae,* and *Plasmodium ovale*. The malaria parasites multiply within 48−72 hours and destroy red blood cells. Malaria pigment occurs when the parasite infects host red blood cells and ingests and degrades hemoglobin in its acidic digestive vacuole releasing heme. The heme, which is toxic to the parasite, is detoxified by conversion into a solid crystalline form called malaria pigment. Since the formation of hemozoin appears to prevent the toxic effect of heme to the parasite, prevention of its formation is a primary target of antimalarial drug design (Wood, Langford, Cooke, Glenister, Lim, and McNaughton, 2003). Thus, knowledge of the structure and chemistry of the malaria pigment heme system has important implications in modeling and testing of new antimalarial drugs designed to inhibit hemozoin formation.

1.1 Porphyrins and Metalloporphyrins

A porphyrin is a macrocyclic molecule consisting of four pyrrolic rings linked at the *alpha* carbons by methylene bridges as shown in Figure 1.1. The pyrrolic and methine CH groups are named as *beta* and *meso* groups, respectively. The maximun symmetry of the free base porphyrin is D_{2h} (assuming complete planarity). When

coordination occurs, two protons are lost from the pyrrolic nitrogens atoms, leaving two negative charges. The porphyrin dianion is a nearly planar 18 π-electron delocalized system with a core defining a cyclic tetradentate ligand, in which the space available for a coordinated metal has a maximum diameter of approximately 3.7 Å (Falk, 1964).

porphine when   R = R' = H
tetraphenylporphyrin when   R = phenyl
                                        R' = H
octaethylporphyrin when   R = H
                                        R' = ethyl
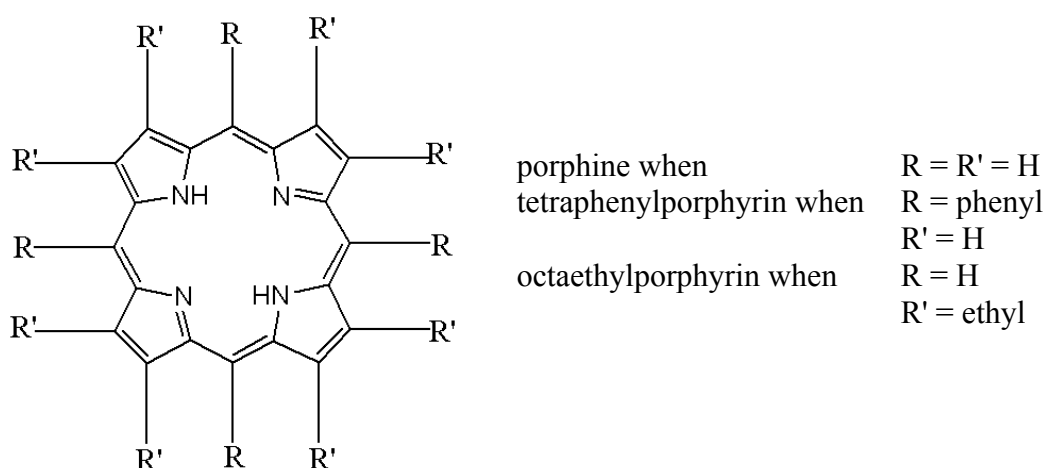
Figure 1.1 Schematic drawing of porphine and porphyrins.

Protons on the periphery of the four-pyrollic ring core of the porphyrin may be substituted by a variety of ligands. Most naturally occuring porphyrins have substituents in all or most of the eight *beta*-positions. Protoporphyrin IX (PPIX) is one of the most abundant naturally occurring porphyrins while *meso*-tetraphenylporphin (TPP) was the earliest common synthetic model employed for the natural porphyrins (Fleischer, 1970) due to its ease of synthesis and low cost. The other common model system is octaethylporphyrin (OEP) with the alkyl substituents on the *beta* carbon atoms making it more comparable to PPIX.

When two pyrrole protons of a porphyrin are removed, coordination between the pyrrole nitrogen atoms and a metal ion can occur. The metal ion coordinates in (or

on) the core nitrogen atoms to provide a metalloporphyrin as exhibited the schematic diagram in Figure 1.2. The idealized symmetry of the macrocyclic core of metalloporphyrins is D_{4h} Thus, the minimum coordination number of metalloporphyrin is four coordinate with a square-planar geometry. The central metal ion can accept an axial ligand in the fifth coordination site to form square-pyramidal or tetragonal-pyramidal geometry, and a sixth ligand to give distorted octahedral geometry. Eight-coordinate sandwich compounds with square antiprismatic geometry are also known (Fleischer, 1970). Metalloporphyrins have been widely studied as models for heme proteins (iron porphyrin derivatives), the various photosynthetic pigments (magnesium complexes), the vitamin B_{12} coenzyme (cobalt corrinoids), and coenzyme F_{430} (nickel corphinoids) (Scheidt and Lee, 1987).
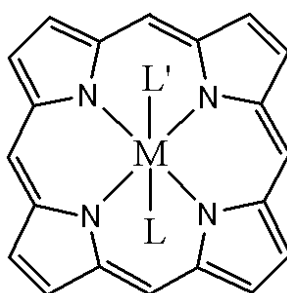
Figure 1.2 Schematic diagram of a metalloporphyrin.

1.2 Iron Porphyrins

Some metal ions, such as iron, chelated in porphyrins may exhibit a variety of oxidation states, for example zerovalent Fe(0) and monovalent Fe(I) (Mashiko, Reed, Haller, and Scheidt, 1984), divalent Fe(II), trivalent Fe(III), and quadrivalent Fe(IV) states. The resulting complexes can be neutral, positively or negatively charged, and can be radicals depending on the type of the axial ligand and counter ion.

Iron porphyrins are the prosthetic groups for a variety of hemoproteins such as hemoglobin, myoglobin, cytochromes, catalases, and peroxidases. Iron protoporphyrin IX, Fe(PPIX), which is shown in Figure 1.3, is an example of a heme complex. It plays an essential role in various biological reactions such as oxygen transport, respiration, drug detoxification, and signal transduction (Trivedi, Chand, Maulik, and Bandyopadhyay, 2005).
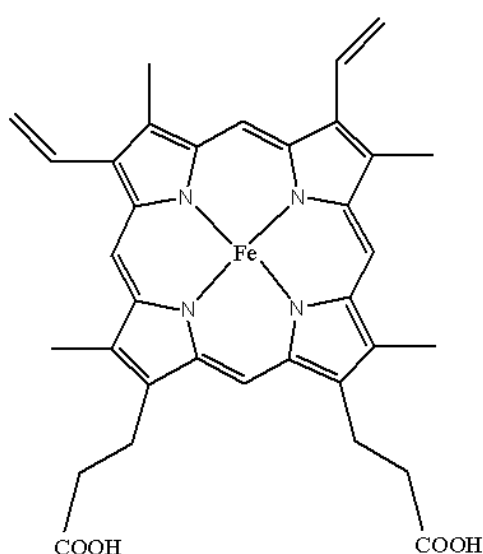
Figure 1.3 Schematic diagram of iron protoporphyrin IX. The iron can exhibit various oxidation states giving iron(0) PPIX; iron(I) PPIX; ferrous PPIX for Fe^{2+}, ferric PPIX for Fe^{3+}, and ferryl PPIX for Fe^{4+}.

Coordination of one axial hydroxide to ferric protoporphyrin IX gives hematin, Fe(PPIX)OH, and of one axial chloride gives ferric protoporphyrin IX chloride, Fe(PPIX)Cl, also known as hemin (Figure 1.4). Synthetic iron porphyrin coordination complexes that have been extensively studied as models of heme systems are Fe(TPP) because of its convenient synthesis and Fe(OEP) because of its similarity to

Fe(PPIX). A variety of axial ligands, oxidation states, spin states, and coordination number of the central metal ions with heme derivatives has been studied.

Typical monomeric metalloporphyrins which have been frequently studied are Fe(TPP)Cl (Hoard, Cohen, and Glick, 1967; Scheidt and Finnegan, 1989) and Fe(OEP)Cl (Senge, 2005). Two dimeric metalloporphyrin structures which have been determined are [Fe(TPP)]$_2$O (Hoffman, Collins, Day, Fleischer, Srivastava, and Hoard, 1972; Swepston and Ibers, 1985) and [Fe(OEP)]$_2$O (Cheng, Hobbs, Debrunner, Erlebacher, Shelnutt, and Scheidt, 1995).
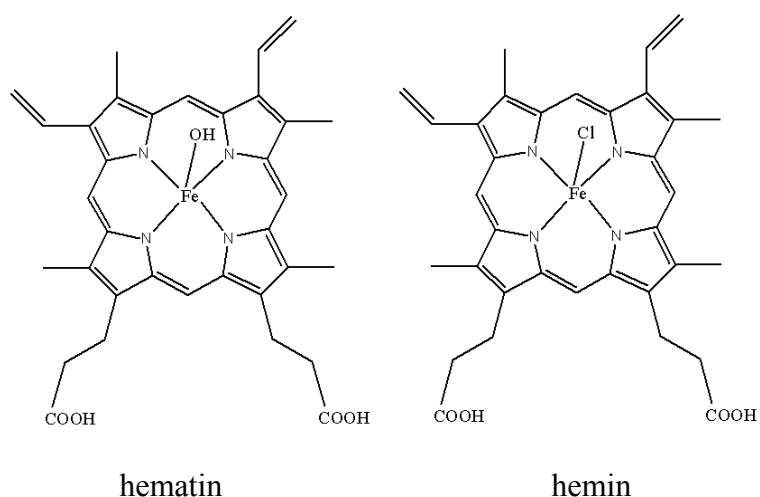
hematin   hemin

Figure 1.4 Schematic diagram of hematin and hemin.

The possible coordination states of natural and synthetic iron porphyrin include four-coordinate (no axial ligands), five-coordinate (one axial ligand), and six-coordinate (two axial ligands) geometries. The number of axial ligands and their nature, as well as the spin state and oxidation state of iron have influence on the Fe−N(porphyrin) bond distances, the Fe−axial ligand bond distances, the displacement of the iron atom out of the porphyrin plane, the stereochemistry, and the resonance Raman spectra (Scheidt and Lee, 1987; Walker, 1994).

A nice example of the variation in Fe−N(porphyrin) bond distances as a function of the spin state of the metal ion in a typical heme complex can be found in the six-coordinate $[Fe(OEP)(3\text{-}Cl\text{-}py)_2]^+$ cation. The low-spin state appears to be lowest in energy. At 98 K, the six-coordinate low-spin iron(III) molecule crystallizes in a triclinic lattice, and the average Fe−N(porphyrin) distance is 1.994 Å, and the axial Fe−N distance is 2.031 Å (Scheidt, Geiger, and Haller, 1982). At 293 K, the crystal lattice of this compound contains a thermal mixture of high-spin and low-spin states, Fe−N(porphyrin) bond distance of 2.014 Å, and axial Fe−N distance is 2.194 Å. The average structure of the two spin states at 293 K was interpreted, showing the low-spin axial Fe−N distance to be 2.043 Å and the high-spin axial Fe−N distance to be 2.316 Å (Scheidt, Geiger, and Haller, 1982). Two different quantum admixed intermediate-spin forms have also been crystallized (Scheidt, Geiger, Hayes, and Lang, 1983; Scheidt, Geiger, Lee, Reed, and Lang, 1987). The intermediate-spin forms exhibit Fe−N(porphyrin) bond distances of 2.005 and 2.006 Å, and axial Fe−N distances of 2.310 and 2.304 Å. The Fe−N bond distances and spin state data are given in Table 1.1. The Fe−N(porphyrin) bond distances are more similar for low- and intermediate-spin forms, while the axial Fe−N distances are more similar for intermediate- and high-spin forms. This can be easily understood on the basis of the location of the d electrons of the d^5 iron(III) atom.

Table 1.1 Iron–Nitrogen Distances vs Spin State in Six-Coordinate

Fe(OEP)(3-Cl-py)$_2$]$^+$ perchlorate.[a]

Spin state	Spin	T (K)	d[Fe–N$_{eq}$] (Å)	d[Fe–N$_{ax}$] (Å)	Sp.Gr.	Z	Reference
Low spin	S=$^1/_2$	98	1.994(6)	2.031(2)	*P*−1	1	[b]
		293	(1.990)	2.043[c]	*P*−1	1	[b]
Intermediate spin	S=$^3/_2$	293	2.005(6)	2.310(17)	*P2$_1$/a*	8	[d]
		292	2.006(8)	2.304[c]	*Pbca*	8	[e]
High spin	S=$^5/_2$	293	(2.045)	2.316	*P*−1	1	[b]
Mixed spin	S=$^1/_2$,$^5/_2$	293	2.014(4)	2.194(2)	*P*−1	1	[b]

[a] Three crystalline forms of this structure have been structurally characterized.
[b] Scheidt, Geiger, and Haller, 1982.
[c] Scheidt and Reed, 1981.
[d] Scheidt, Geiger, Hayes, and Lang, 1983.
[e] Scheidt, Geiger, Lee, Reed, and Lang, 1987.

The one interesting in iron porphyrin is Fe(PPIX) which is exclusively consistent in malaria pigment. Many researchers have studied the formation of malaria pigment to determine the major route of heme detoxification in the parasite and to gain more insight into the structure of this important molecule.

1.3 Malaria Pigment

Study of malaria pigment has a long history. Egan (2008) notes that the pigment was reported in 1717 by Giovanni Maria Lancisi before the malaria parasite was known. Carbone (1891) identified hematin as the first model for malaria pigment by noting the similarity between malaria pigment and hematin based on the parallelism of their solubility. The chemical and spectroscopic nature of malaria pigment has been studied since Brown (1911) confirmed Carbone's work and reported the first

spectroscopic characterization of hemozoin. Brown concluded, "The spectroscopic examination of a solution of malarial pigment proves conclusively that the pigment is hematin." Brown was nearly correct, β-hematin, synthetic malaria pigment, is a blue to blackish-brown compound formed from the reaction of hematin and other related iron(III) protoporphyrin IX complexes by the removal of the axial ligand. Brown studied the solution resulting from dissolving malaria pigment in alcoholic KOH, which would indeed produce hematin. Pagola reports (Pagola, Stephens, Bohle, Kosar, and Madsen, 2000) that in 1949, a model of β-hematin was proposed to be ion paired dimers of a cationic six-coordinate iron to anionic propionates.

1.4 Molecular Structure of Malaria Pigment by X-ray Methods

Hemozoin from the human malaria organism *Plasmodium falciparum* and β-hematin prepared by chemical synthesis under acidic conditions have been characterized by infrared spectroscopy and X-ray diffractometry. The synthetic analog, β-hematin is chemically (Fitch and Kanjananggulpan, 1987), spectroscopically (Wood, Langford, Cooke, Glenister, Lim, and McNaughton, 2003), and from synchrotron powder diffraction, crystallographically (Pagola, Stephens, Bohle, Kosar, and Madsen, 2000) indistinguishable from hemozoin.

The structure of synthetic β-hematin prepared by acidification of hematin in acid was proposed to be a polymeric structure with links between the Fe(III) ion of one heme and a carboxylate side-group oxygen of another heme (Slater, Swiggard, and Orton, 1991). Bohle and Helms (1993) synthesized β-hematin by dehydrohalogenation of hemin in basic media. The infrared spectra also showed

carboxylate ligation, supporting the bridged hypothesis. In 1994, the polymerization of hematin to β-hematin in acidic conditions was reported. The IR spectra of β-hematin prepared under acidic conditions again showed the carboxylate ligation peaks (Egan, Ross, and Adams, 1994). Three years later, Bohle, Dinnebier, Madsen, and Stephens (1997) prepared synthetic β-hematin from hemin by treating with bases in anhydrous conditions, and characterized it and hemozoin from the malarial *Plasmodium falciparum* by synchrotron X-ray powder diffraction. The X-ray diffraction patterns for hemozoin from the malarial *Plasmodium falciparum*, and synthetic β-hematin were indistinguishable leading to the conclusion that hemozoin is a coordination polymer of iron(III) protoporphyrin IX with hydrogen-bonded propionic dimerization between chains as shown in Figure 1.5.

In 2000 the crystal structure of β-hematin, synthesized by dehydrohalogenation of hemin under basic conditions, was determined by placing the known structure of the iron(III) protoporphyrin IX unit (Koenig, 1965) in the unit cell, locating the position of the molecular fragment (finding x, y, z), the best orientation with respect to the unit cell (Euler angles; ϕ, θ, ρ), and finding the best values for the eight torsional angles defining the vinyl and propionic acid groups relative to the porphyrin plane, that is refining 14 parameters to determine the 43 nonhydrogen atom structure using simulated annealing, and refined by the Rietveld method, based on synchrotron powder X-ray diffraction data.

The structure shows the molecules to be linked into dimers through reciprocal iron-carboxylate bonds using a (deprotonated) propionate from one of the propionic acid side chains of each porphyrin. The dimers are linked into chains by hydrogen

bonds between the remaining propionic acid side chains as shown in Figure 1.6 (Pagola, Stephens, Bohle, Kosar, and Madsen, 2000).

β-hematin prepared in acid and base reaction conditions using hemin as starting material were studied. Both crystalline forms have the same space group and unit cell found by Pagola *et al*. and the structures, determined by X-ray powder diffraction, show the molecules to be the same heme dimers (Figure 1.7) containing the same iron-carboxylate and propionic acid links as reported before (Bohle, Kosar, and Stephens, 2002).
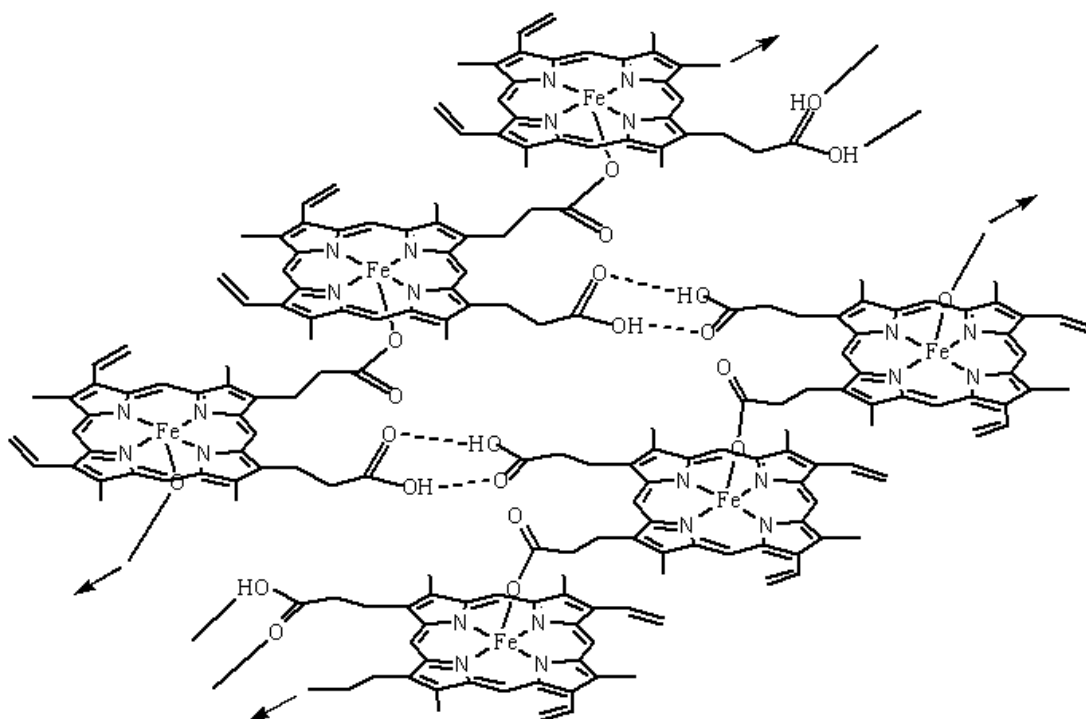
Figure 1.5 Proposed structure of β-hematin. Drawn by ChemDraw after the Slater Swiggard, and Orton (1991) proposal.
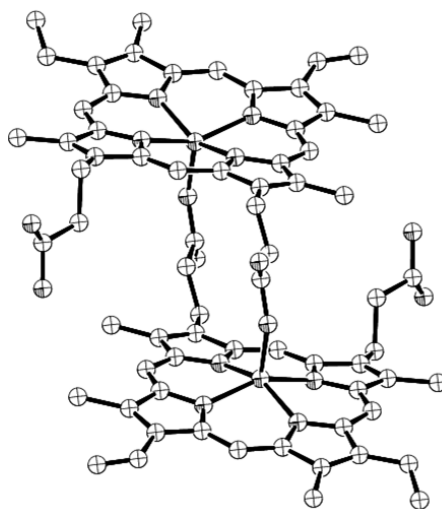
Figure 1.6 β-hematin dimer structure. Drawn by *ORTEP-III* (Burnett and Johnson, 1996) using the coordinates for Refcode XETXUP from the CSD (2006).
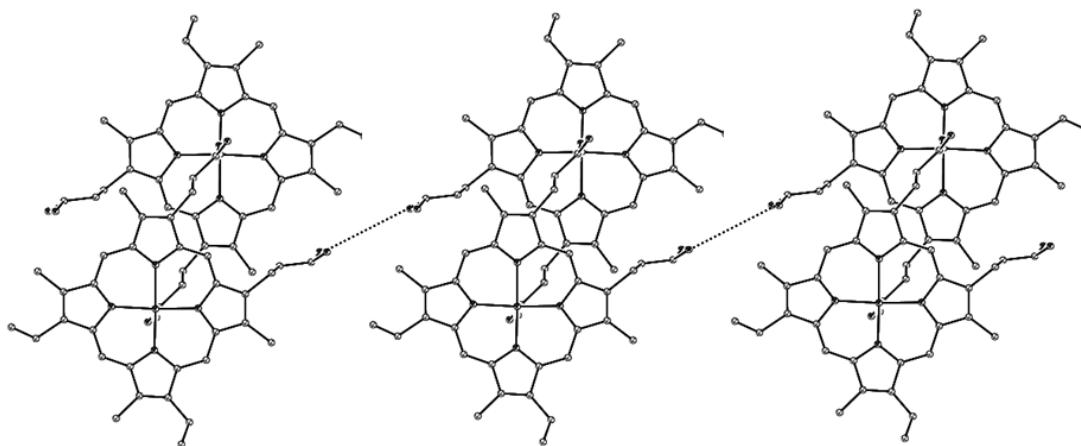
Figure 1.7 Hydrogen bonded chains in the β-hematin dimer structure. Drawn by *ORTEP-III* (Burnett and Johnson, 1996) using the coordinates for Refcode XETXUP from the CSD (2006).

Recently the structures of hemozoin extracted from rabbit and hamster blood, and β-hematin synthesized by dehydrohalogenation of hemin with dimethylsulfoxide

as the catalyst were reported. Synchrotron X-ray diffraction spectra showed that both crystalline materials have the same unit cell and structure as Pagola *et al*. reported. The structure of hemozoin was found to consist of heme dimers bound by the same reciprocal iron-carboxylate interactions and propionic acid hydrogen bonds (Oliveira, Kycia, Gomez, Kosar, and Bohle, 2005).

Several experimental approaches have been described and different methods for characterization employed in the search for the structures of β-hematin and hemozoin over the last century. A summary of recent structural proposals and the unit cell data for synthetic and natural malaria pigment is given in Table 1.2. The structural evidence of the last decade for natural and synthetic malaria pigment from a variety of sources, starting materials, and reaction conditions all exhibit the same structure. While there are common authors on the various reports of dimeric structures they have chosen to represent the same structure with a bewildering arrangement of different views of the structure in the various papers, as shown in Figures 1.6 and 1.7 without attempt to show their commonality or comparison to other proposed models. Moreover, the atomic coordinates in the β-hematin structure are not accurate (Pagola, Stephens, Bohle, Kosar, and Madsen, 2000). To date none of the researchers has been able to grow single crystals of β-hematin large enough to analyze by single crystal X-ray crystallography.

Table 1.2 Summary of Recent Structural Proposals and Unit Cell Data for Synthetic and Natural Malaria Pigment.

Reference	Source	Reaction Type[a]	Reaction Conditions	Structure	Space group	Unit cell
Lemberg *et al.* (1949)				dimer[b]	[c]	[c]
Slater *et al.* (1991)	hematin	AAP	70 ˚C, 12 h	polymer	[c]	[c]
Bohle *et al.* (1993)	hemin	ABM	22 ˚C, 12 h	polymer	[c]	[c]
Egan *et al.* (1994)	hematin	AAP	70 ˚C, 12 h	polymer	[c]	[c]
Bohle *et al.* (1997)	hemin	ABM/ DMSO catalyst	22 ˚C, 12 h	polymer	$P–1$ (Z = 2)	Triclinic a = 12.2176(4) b = 14.7184(5) c = 8.0456(3) α = 90.200(2) β = 96.806(3) γ = 97.813(3)
Pagola *et al.* (2000)	hemin	ABM	22 ˚C, 12 h	dimer	$P–1$ (Z = 2)	Triclinic a = 12.196(2) b = 14.684(2) c = 8.040(1) α = 90.22(1) β = 96.80(1) γ = 97.92(1)
Bohle *et al.* (2002)	hemin	AAP ABM	70 ˚C 22 ˚C	dimer dimer	[c] [c]	[c] [c]
Wood[d] (2004)	hematin			trimers and tetramers[d]	[c]	[c]
Oliveira *et al.* (2005)	hemin	ABM	22 ˚C, 12 h	dimer	$P–1$ (Z = 2)	Triclinic a = 12.198(6) b = 14.681(4) c = 8.013(3) α = 90.65(3) β = 96.74(3) γ = 97.78(1)
	rabbit blood	biological extraction	room temp	dimer	$P–1$ (Z = 2)	Triclinic a = 12.21(2) b = 14.784(15) c = 8.034(9) α = 90.54(15) β = 97.10(12) γ = 97.23(12)
	hamster blood	biological extraction	room temp	dimer	$P–1$ (Z = 2)	Triclinic a = 12.206(12) b = 14.776(8) c = 8.028(5) α = 90.48(9) β = 97.09(7) γ = 97.38(7)

[a] AAP = aqueous acid precipitation, ABM = anhydrous-base-mediated method, DMSO = dimethylsulfoxide. [b] Pagola, Stephens, Bohle, Kosar, and Madsen (2000) reports. [c] Structure assigned on data other than unit cell and space group. Neither unit cell nor space group was reported in this work. [d] Mass spectroscopic results showing trimers and tetramers (Wood, 2004).

1.5 Molecular Structure of Malaria Pigment by Raman Spectroscopy

Resonance Raman (RR) spectroscopy is a powerful tool to investigate the structural features, electronic properties, and functional information of metalloporphyrin complexes, particular iron porphyrins.

RR has been an important tool in the understanding of heme protein structure and function (Spiro and Strekas, 1972). Moreover RR spectroscopy provides the vibrational frequencies of biological chromophores such as hemes, flavins, and metal ions which are at the sites of biological function (Spiro, 1974). The resonance Raman spectra of metallporphyrins provides avenues both to theoretical elucidation of vibronic scattering mechanisms and to structure applications (Burke, Kincaid, and Spiro, 1978). RR spectroscopy has been used to characterize coordination number and small molecules used as axial ligands (Teraoka and Kitagawa, 1980) including the detection of important Fe−CO stretching and Fe−C−O bending vibrations using Soret excitaion laser wavelengths (Armstrong, Irwin, and Wright, 1982; Tsubaki, Srivastava, and Nai-Teng, 1982). In fact, the technique is ideally suited for these studies in as much as it permits one to focus observations directly on the active site in the proteins, owing to its ability to selectively enhance vibrational modes of the chromophoric heme prosthetic group (Kincaid, 2000).

RR spectroscopy was proposed to identify the structure of μ-oxo [Fe(DPDE)]$_2$O which was thought to be the moiety of malaria pigment (Kowalewski, Merlin, Brémard, and Moreau, 1988). The result confirmed that the μ-oxo [Fe(DPDE)]$_2$O was a high spin iron(III) complex and the axial ligation on Fe(DPDE) was concomitant

with the enhancement of the Fe−O−Fe mode. The μ-oxo bridging existing in malaria pigment is ambiguous. Later, Brémard studied the enhancement of Fe−O−Fe mode and found that the enhancement of this mode corresponded to the oxo $\rightarrow$ Fe charge transfer transition (Brémard, Kowalewski, and Merlin, 1992).

RR spectra of malaria pigment at various excitation wavelengths proves that it is indistinguishable to from that of β-hematin (Wood, Langford, Cooke, Glenister, Lim, and McNaughton, 2003). RR has been used to investigate the electronic structure of β-hematin and malaria pigment (Wood, Langford, Cooke, Lim, Glenister, Duriska, Unthank, and McNaughton, 2004). The RR results confirm β-hematin to be a high-spin iron(III) complex bonded with the O atom as the axial ligand. The study reported the enhancement of totally symmetric modes associated with porphyrin ring-breathing vibrations occurring when using near-IR excitation laser wavelengths (782 and 830 nm). The observation that β-hematin exhibits greater enhancement than hemin was explained in terms of aggregation between porphyrin units in β-hematin based on intermolecular excitonic interactions. Enhancement of totally symmetric modes at near-IR wavelengths was also observed in some μ-oxo dimer derivatives such as $[Fe(TPP)]_2O$ but not in $[Fe(OEP)]_2O$ (Webster, 2005). Recently, RR spectra of hemozoin exhibits a mode located at the propionic side chain which links the hemozoin dimers to each other and assigns band with Density Functional Theory (DFT) calculation (Frosh, Koncarevic, Zedler, Schmitt, Schenzel, Becker, and Popp, 2007).

1.6 Malaria Pigment Model Systems

What is a model system? There may be several ways to answer this question. From one point of view a model simply reproduces the form of an object on a different scale. An example would be a scale model of an airplane. Generally, no one expects this model to be a functional airplane, and probably, no one even expects it to be able to fly.

A second view of a model would be that the model contains the essential features of the object being modeled. There may be discussion, and even disagreement, as to what are the essential features of the object. From this point of view one way of defining a model system of a coordination compound would be to require the same (or similar) metal atoms in the same oxidation state and the same spin state, the same (or similar) ligands, the same coordination number, and the same geometrical disposition of the ligands about the central metal. Such a model could be called a structural model.

Malaria pigment is a coordination compound, and from this point of view it can be observed from the structural work reviewed above that malaria pigment contains a porphyrin with alkyl substituents on the *beta* carbon atoms, coordinated to high-spin iron(III) (d[Fe–N] = 2.061 Å) with a monodentate O-bonded axial carboxylate ligand (d[Fe–O] = 1.893 Å) (Pagola, Stephens, Bohle, Kosar, and Madsen, 2000), and exhibits tetragonal pyramidal coordination geometry about the iron atom. Important factors and interactions for stereochemistry in malaria pigment model system are spin state, oxidation state, and coordination number of iron, intermolecular distances and angles, and the nature of the axial ligand above the plane of porphyrin. In addition, since malaria pigment is only known as a solid state compound, the intramolecular

and intermolecular interactions (often called *crystal structure* or *supramolecular structure*) are also important.

In this context, preliminary characterization of Fe(OEP)picrate has been carried out (Puntharod and Haller, 2006). Fe(OEP)picrate consists of a five-coordinate high-spin iron(III) atom displaced above the 4N-coordination plane of octaethylporphyrin towards the axially coordinated O-bonded picrate ligand. The axial Fe−O distance 1.928(2) Å, 0.015 Å larger than the average Fe−O(OAr) value of 1.913 Å found by structure correlation (Bürgi and Dunitz, 1994). The Fe−N distances range from 2.028–2.055 Å compared to 2.050(1) Å for high spin iron(III) in [Fe(OEP)($O_2C_2Cl_3$)]·$CHCl_3$ (Neal, Cheng, Ma, Shelnutt, Schulz, and Scheidt, 1999). Analysis of the crystal structure shows π−π stacking between adjacent porphyrin cores related by an inversion center with a porphyrin to porphyrin contact distance of 3.504(3) Å.

A third type of model is a functional model where the essential feature is some property of the original system, for example a spectroscopic property such as the Raman/resonance Raman spectra mentioned above (Wood, Langford, Cooke, Lim, Glenister, Duriska, Unthank, and McNaughton, 2004). Table 1.3 compares the stereochemistry of the iron(III) porphyrin malaria pigment model systems that are important to this work. All have the same stereochemistry consisting of a high-spin five-coordinate Fe(III). Interestingly, only [Fe(OEP)]$_2$O does not show the enhancement of the totally symmetric $\nu(C_\alpha−N)$ mode which is sensitive to the oxidation marker band, ν_4 when exciting with near-infrared excitation wavelengths.

This thesis investigates the molecular and electronic structure as well as stereochemistry and interaction chemistry of a series of metalloporphyrins to determine what gives rise to enhancement of the totally symmetric modes at near-infrared excitation wavelengths and to attempt to understand why the enhancement occurs. β-hematin was synthesized in this work for spectral comparison to the model compounds by the previously unused hydrothermal method. Unfortunately, the size of synthetic β-hematin is not big enough for single crystal X-ray structural characterization. However, the study of relative Raman intensity of the totally symmetric mode, ν_4 which is strongly affected by supramolecular interactions may reveal the next important factor to answer the remaining questions on the structure of β-hematin.

The model system for this thesis incorporates essential structural features and essential functional features as a basis to model malaria pigment. An important aspect to this work is a detailed examination of the solid state crystallographic structures of Fe(TPP)Cl, [Fe(TPP)]$_2$O, Fe(OEP)Cl, [Fe(OEP)]$_2$O, and Fe(OEP)picrate which contain the essential structural features (five-coordinate, square-pyramidal, high-spin, iron(III)porphyrin complexes), and correlating this data with the relative RR enhancement of the totally symmetric pyrrole half-ring stretching vibration known as ν_4 at approximately at 1375–1370 cm^{-1}. The models contain the same essential features that show the enhancement of ν_4 when applying with near-IR excitation wavelengths. The critical observation was that of the compounds investigated the dimer [Fe(OEP)]$_2$O did not show the enhancement of ν_4. On the other hand the

monomer Fe(OEP)Cl did show the enhancement when applying with near-IR excitation lasers.

Table 1.3 Comparison of Stereochemistry for Iron(III) Porphyrin Malaria Pigment Model Systems Used in this Work.

Heme derivatives	OS^a of Fe	CN^a of Fe	Axial ligand	d[Fe–N] (Å)	d[Fe–O] (Å)	Displacement of Fe (Å)	Intermolecular distance between porphyrin rings	Enhancement of ν_4 band at near-IR excitation wavelengths
β-hematin P–1, Z = 2 Pagola et al (2000)	3+	5	O	2.061	1.886(2)	0.47	3.43	✓
Hematin	3+	5	O	[b]	[b]	[b]	[b]	✓
Fe(TPP)Cl $P2_1/n$, Z = 4 Scheidt et al. (1989)	3+	5	Cl	2.070(9)	–	0.57	4.5779	✓
[Fe(TPP)]$_2$O C2ca, Z = 4 Hoffman et al. (1972)	3+	5	O	2.087(3)	1.763(1)	0.54	5.20	✓
Fe(OEP)Cl $P2_1/c$, Z = 4 Senge (2005)	3+	5	Cl	2.071(2)	–	0.494(1)	4.02(1)	✓
[Fe(OEP)]$_2$O P–1, Z = 2 $P2_1/c$, Z = 4 Cheng et al. (1995)	3+	5	O	2.077(3) 2.080(5)	1.756(3) 1.755(10)	0.50 0.54	4.5 4.6	✗
Fe(OEP)picrate C2/c, Z = 8	3+	5	O	2.044(2)	1.928(2)	0.403	3.504(3)	✓

[a] OS = oxidation state; CN = coordination number. [b] No crystal data of hematin.

Because of the bioinorganic model systems known as a solid state TPP and OEP derivatives, the intermolecular interaction is very important. However, the intramolecular interaction was also considered. According to study the delocalization between the phenyl and porphyrin π system, and the steric hindrance from the substituent groups, it was found that the intramolecular interactions are not a contributing factor to the enhancement of oxidation state marker band, ν_4 particularly at near-IR excitation wavelengths. The critical finding in this thesis is that

intermolecular interactions are pivotal in explaining the excitonic enhancement of ν_4. It was not possible to record solution phase spectra of the monomers and dimers Fe(TPP) and Fe(OEP) even at high concentrations (> 10 mM) and laser power 20 mW. This provides supporting evidence that the enhancement of ν_4 at near-IR excitation in a solid state phenomenon involving supramolecular interactions.

1.7 Supramolecular Interactions

Noncovalent interactions play an important role in chemistry, particularly in the structure of bio-macromolecules such as DNA and proteins. Such interactions are used in the assembly of supramolecular species in such structures, as well as in solid state aggregates. Lehn (1987) defined noncovalent chemistry as supramolecular chemistry. Supramolecular chemistry has played an important role in crystal engineering of cocrystals which are useful in pharmaceutical applications, and has also served as an important model and mimic biological processes in biological chemistry. Supramolecular chemistry offers incredible applications such as medical chemistry (drug delivery systems), host-guest chemistry, catalysis, and molecular electronics (Müller-Dethlefs and Hobza, 2000) and efficient near-IR light scatterers as demonstrated in this thesis.

The various types of supramolecular interactions are commonly called π–π stacking, C–H···π hydrogen bond interaction, and C–H···X hydrogen bond interaction (when X is an electron donating atom), electrostatic interactions, hydrophobic interactions, charge-transfer interactions, and metal coordination (Müller-Dethlefs and Hobza, 2000) which can be determined by X-ray crystallography. These interactions can be found in metalloporphyrin compounds including the monomers

and dimers of Fe(TPP) and Fe(OEP), which show C–H···Cl hydrogen bond interaction, and C–H···π hydrogen bond interaction, respectively. On the other hand Fe(OEP)picrate shows π–π and C–H···O hydrogen bond interactions.

Supramolecular chemistry of porphyrin systems can also associate with noncovalent interactions such as ligand-to-metal coordination, hydrogen bonding, dipole–dipole interaction, π–π interaction, C–H···π interaction, and van der Waals (Ogoshi, Mizutani, Hayashi, and Kuroda, 2000).

The malaria pigment model used herein contains a porphyrin with alkyl or aryl substituents on the *alpha* and/or *beta* or *meta* carbon atoms, coordinated to high spin iron(III) with a monodentate axial ligand and exhibits square-pyramidal five-coordinate geometry, the important factors that affect the interactions in malaria pigment model are the type of substituent group and the nature of the axial ligand above the plane of the porphyrin. In addition, the crystal structure or supramolecular structure is useful for modeling the interaction in malaria pigment. However, the nature of the axial ligand is not an essential factor for the enhancement of the totally symmetric, v_4 band. Nonetheless, the enhancement of v_4 at near-IR excitation can be used as an indicator of the supramolecular interactions in heme aggregates. Moreover the relative intensity of v_4 may be an indicator of the strength of concerted supramolecular interactions in heme systems (Webster, Tilley, Deed, McNaughton, and Wood, 2008). This is the first time that hydrogen bonds have been implicated in causing resonance Raman enhancement via the excitonic coupling mechanism.

This work has covered the general structural properties of malaria pigment model as the five-coordinate, square-pyramidal, high-spin, iron(III) porphyrine by RR spectroscopy and crystallography. This information can be usefully employed in the

interpretation of the chemistry of the iron(III) porphyrin and also aid the understanding of the biological action of the iron(III) porphyrins including malaria pigment. Moreover the discovery of the important role that hydrogen bonding interactions play in energy transfer in heme supramolecular aggregates may well pave the way forward to the development of nano-wires heme based assemblies and other near-IR photon transfer sensors.

1.8 References

Armstrong, R. S., Irwin, M. J., Wright, P. E. (1982). Soret-excited resonance Raman spectrum of (carbonnonoxy)leghemoglobin : Assignment of ν_{Fe-CO}. **J. Am. Chem. Soc.** 104(2): 626−627.

Bohle, D. S., Dinnebier, R. E., Madsen, S. K., Stephens, P. W. (1997). Characterization of the products of the heme detoxification pathway in malarial late trophozoites by X-ray diffraction. **J. Bio. Chem.** 272(2): 713−716.

Bohle, D. S., Helms, J. B. (1993). Synthesis of β-hematin by dehydrohalogenation of hemin. **Biochem. Biophys. Res. Commun.** 193(2): 504−508.

Bohle, D. S., Kosar, A. D., Stephens, P. W. (2002). Phase homogeneity and crystal morphology of the malaria pigment β-hematin. **Acta Cryst. D** 58(10−1): 1752−1756

Brémard, C., Kowalewski, P., Merlin, J. C. (1992). Resonance Raman enhancement of the oxo-bridged dinuclear iron center: Vibrational modes in iron(III) physiological -type porphyrin complexes. **J. Raman Spectrs.** 23: 325−333.

Brown, W. H. (1911). Malarial pigment (so-called melanin): its nature and mode of production. **J. Exp. Med.** 13: 290–299.

Bürgi, H. B., Dunitz, J. D. (1994). **Structure Correlation**. Vol. 2, VCH, pp. 817.

Burke, J. M., Kincaid, J. R., Spiro, T. G. (1978). Resonance Raman spectra and vibrational modes of iron(III) tetraphenylporphine μ-oxo dimer. Evidence for phenyl interaction and lack of dimer spitting. **J. Am. Chem. Soc.** 100(19): 6077−6083.

Burnett, M. N., Johnson, C. K. (1996). *ORTEP-III*: *Oak Ridge Thermal Ellipsoid Plot Program for Crystal Structure Illustrations*, Report ORNL-6895, Oak Ridge National Laboratory, Oak Ridge TN.

Callahan, P. M., Badcock, G. T. (1981). Insights into heme structure from Soret excitation Raman spectroscopy. **Biochem.** 20(4): 952−958.

Cambridge Structural Database. (2006) version 5.27, updates August 2006.

Carbone, T. (1891). Sulla natura chimica del pigmento malarico. Giornale della R. **Accad. di med. di Torino.** 39(3): 901−906.

Cheng, B., Hobbs, J. D., Debrunner, P. G., Erlebacher, J., Shelnutt, J. A., Scheidt, W. R. (1995). An unusual near-eclipsed porphyrin ring orientation in two crystalline forms of (μ-oxo)bis[(octaethylporphinato)iron(III)]. Structural and molecular mechanics studies. **Inorg. Chem.** 34(1): 102−110.

Cole, K. A., Zieglar, J., Evans, C. A., Wright D. W. (2000). Metalloporphyrins inhibit β-hematin (hemozoin) formation. **J. Inor. Bio.** 78(2): 109−115.

Egan, T. J. (2008). Recent advances in understanding the mechanism of hemozoin (malaria pigment) formation. **J. Inor. Bio.** 102(5−6): 1288−1299.

Egan, T. J., Ross, D. C., Adams, P. A. (1994). Quinoline anti-malarial drugs inhibit spontaneous formation of β-hematin (malaria pigment). **FEBS Letters** 352(1): 54−57.

Falk, J. E. (1964). **Porphyrins and Metalloporphyrins**. Vol. 2, Elsevier, pp. 30.

Fitch, C. D., Kanjananggulpan, P. (1987). The state of ferriprotoporphyrin IX in malaria pigment. **J. Bio. Chem.** 262(32): 15552−15555.

Fleischer, E. B. (1970). The structure of porphyrins and metalloporphyrins. **Acc. Chem. Res.** 3: 105−112.

Frosh, T., Koncarevie, S., Zedler, L., Schmitt, M., Schenzel, K., Becker, K., Popp, J. (2007). In *Situ* localization and structural analysis of the malaria pigment hemozoin. **J. Phys. Chem. B** 111(39): 11407−11056.

Fuhrhop, J. H., Endisch, C. (2000). **Molecular and Supramolecular Chemistry of Natural Products and Their Model Compounds** Marcel Dekker, Inc, New York.

Hoard, J. L., Cohen, G. H., Glick, M. D. (1967). The stereochemistry of the coordination group in an iron(III) derivative of tetraphenylporphine. **J. Am. Chem. Soc.** 89(9): 1992−1996.

Hoffman, A. B., Collins, D. M., Day, V. W., Fleischer, E. B., Srivastava, T. S., Hoard, J. L. (1972). The crystal structure and molecular stereochemistry of μ-oxo- bis[$\alpha,\beta,\gamma,\delta$-tetraphenylporphinatoiron(III)]. **J. Am. Chem. Soc.** 94(10): 3620−3626.

Kadish, K. M., Smith, K. M., Guilard, R. (2000). **The Porphyrin Handbook.** Vol. 6, Academic Press, pp. 280.

Kasugai, N., Murase, T., Ohse, T., Nagaoka, S., Kawakami, H., Kubota, S. (2002). Selective cell death by by water-soluble Fe-porphyrins with superoxide dismutase (SOD) activity. **J. Inor. Bio.** 91(2): 349−355.

Kim, H. S., Kim, C. H., Ha, C. S., Lee, J. K. (2001). Organic solar cell devices based on PVK/porphyrin system, **Synthetic Metals** 117(1−3): 289−291.

Kincaid, J. R. (2000). **The Porphyrin Handbook**. Vol. 7, Academic Press.

Koenig, D. F. (1965). The structure of α-Chlorohemin. **Acta Cryst**. 18: 663−673.

Kosal, M. E., Chou, J. H., Wilson, S. C., Suslick, K. S. (2002). A functional zeolite analogue assembled from metalloporphyrins. **Nat. Mater.** 1: 118−121.

Kowalewski, P., Merlin, J. C., Bremard, C., Moreau, S. (1988). Resonance Raman evidence for μ-oxo linkage in ferriporphyrins. **J. Mol. Struct.** 175: 55−60.

Lehn, J-M. (1987). Supramolecular Chemistry - Scope and perspectives molecules - supermolecules - molecular devices. **Nobel Lecture**, Institut Le Bel, Université Louis Pasteur, Paris.

Lemberg, R., Legge, J. W. (1949). **Haematin Compounds and Bile Pigments**. Interscience, New York.

Mashiko, T., Reed, C. A., Haller, K. J., Scheidt, W. R. (1984). **Inorg. Chem.** 23(20): 3192−3196.

Mikšovská, J., Norstrom, J., Larsen, R. W. (2005). Thermodynamic profiles for CO photodissociation from heme model compounds: Effect of proximal ligands. **Inorg. Chem.** 44(4): 1006−1014.

Müller-Dethlefs, K., Hobza, P. (2000). Noncovalent interactions: A challenge for experiment and theory. **Chem. Rev.** 100(1): 143−167.

Neal, T. J., Cheng, B., Ma, J. G., Shelnutt, J. A., Schulz, C. E., Scheidt, W. R. (1999). Conformational diversity in (octaethylporphinato)(trichloroacetato)iron(III) derivatives. **Inorg. Chim. Acta** 291(1−2): 49−59.

Ogawa, K. Kobuke, Y. (2004). **Encyclopedia of Nanoscience and Nanotechnology: Self-Assembled Poprhyrin Arrays** Vol. 9, American Scientific Publishers, pp. 561.

Ogoshi, H., Mizutani, T., Hayashi, T., Kuroda, Y. (2000). **The Porphyrin Handbook: Porphyrins and Metalloporphyrins as Receptor Models in Molecular Recognition**, Vol. 6 Applications: Past, Present and Future, Academic Press, pp. 280.

Oliveira, M. F., Kycia, S. W., Gomez, A., Kosar, A. J., Bohle, D. S., Hempelmann, E., Menezes, D., Vannier-Santos, M. A., Oliveira, P. L., Ferreira, S. T. (2005). Strucural and morphological characterization of hemozoin produced by *Schistosoma mansoni* and *Rhodnius prolixus*. **FEBS Letters** 579(27): 6010−6016.

Pagola, S., Stephens, P. W., Bohle, D. S., Kosar, A. D., Madsen, S. K. (2000). The structure of malaria pigment β-hematin. **Nature** 404(6775): 307−310.

Puntharod, R., Haller, K. J. (2006). Packing interactions of 2,3,7,8,12,13,17,18-octa-ethyphenylporphyrininato(picrato)iron(III), ACA 2006 Annual Meeting, Hawaii, Poster Presentation.

Rosenthal, P. J. (2003). Antimalarial drug discovery: old and new approaches. **J. Exp. Bio.** 206(21): 3735−3744.

Scheidt, W. R., Geiger, D. K., Haller, K. J. (1982a). Structural characterization of a variable-spin (porphinato)iron(III) complex. Molecular stereochemistry of

bis(3-chloeopyridine)(octaethylporphinato)iron(III) perchlorate at 98 K (S = 1/2) and 293 K (S = 1/2, S = 5/2). **J. Am. Chem. Soc.** 104(2): 495−499.

Scheidt, W. R., Geiger, D. K., Haller, K. J. (1982b). Iron(III) Porphyrin Structural Changes Accompanying the Low−Spin―High−Spin Transition, in **Interactions Between Iron and Proteins in Oxygen and Electron Transport**. C. Ho, *et al*. editors, El Sevier/North Holland, New York.

Scheidt, W. R., Geiger, D. K., Hayes, R. G., Lang, G. (1983). Control of spin state in (porphinato)iron(III) complexes. An axial ligand orientation effect leading to an intermediate-spin complex. Molecular structure and physical characterization of the monoclinic form of bis(3-chloropyridine) (octaethylporphinato) iron(III) perchlorate. **J. Am. Chem. Soc.** 105(9): 2625−2632.

Scheidt, W. R., Geiger, D. K., Lee, Y. J., Reed, C. A., Lang, G. (1987). On the preparation of five-coordinate (3-chloropyridine)(porphinato)iron(III) complexes. **Inorg. Chem.** 26(7): 1039−1045.

Scheidt, W. R., Lee, Y. J. (1987). Recent advances in the stereochemistry of metallotetrapyrroles. **Struct. Bond**, 64, Springer-Verlag, pp. 1−70.

Scheidt, W. R., Finnegan, M. G. (1989). Structure of monoclinic chloro(meso-tetraphenylporphyrinato)iron(III). **Acta Cryst. C** 45: 1214−1216.

Senge, M. O. (2005). Chloro(2,3,7,8,12,13,17,18-octaethylporphinato)iron(III). **Acta Cryst. E** 61: m399−m400.

Slater, A. F. G., Swiggard, W. J., Orton, B. R. (1991). An iron-carboxylate bond links the heme units of malaria pigment. **Proc. Natl. Acad. Sci. USA** 88(2): 325−329.

Spaulding, L. D., Chang, C. C., Yu, N., Felton, R. H. (1975). Resonance Raman spectra of of metalloporphyrins. A structure probe of metal displacement. **J. Am. Chem. Soc.** 97(9): 2517−2525.

Spiro, T. G. (1974). Resonance Raman spectroscopy: A new structure probe for biological chromophores. **Acc. Chem. Res.** 7(10): 339−344.

Spiro, T. G., Li, X-Y. (1988). **In Biological Applications of Raman Spectroscopy**; Spiro, T. G., Ed., Vol. 3, John Wiley & Sons, pp. 1−38.

Spiro, T. G., Strekas, T. C. (1972). Resonance Raman spectra of hemoglobin and cytochrome c: Inverse polarization and vibronic scattering. **Proc. Nat. Acad. Sci. USA** 69(9): 2622−2626.

Swepston, P. N., Ibers, J. A. (1985). Redetermination of the structure of μ-oxo-bis [(5,10,15,20-tetraphenylporphyrinato)iron(III)] at 122 K, [$Fe_2O(C_{44}H_{28}N_4)_2$]. **Acta Cryst. C** 41: 671−673.

Tekwani, B. L., Walker, L. A. (2005). Targeting the hemozoin synthesis pathway for new antimalarial drug discovery: Technologies for *in vitro β*-hematin formation assay, **Comb. Chem. High Throughput Screening** 8(1): 63−79.

Teraoka, J., Kitagawa, T. (1980). Raman characterization of axial ligands for penta- and hexacoordinate ferric high- and intermediate-spin (octaethylporphyrinato) iron(III) complexes. Elucidation of unusual resonance Raman spectra of cytochrome *c'*. **J. Phys. Chem.** 84: 1928−1935.

Trivedi, V., Chand, P., Maulik, P. R., Bandyopadhyay, U. (2005). Mechanism of horseradish peroxidase-catalyzed heme oxidation and polymerization (β-hemaitn formation). **Biochem. et Biophy. Acta** 1723(1−3): 221−228.

Tsubaki, M., Srivastava, R. B., Yu, N-T. (1982). Resonance Raman investigation of carbon monoxide bonding in (carbon monoxy)hemoglobin and -myoglobin: detection of iron-carbon monoxide stretching and iron-carbon-oxygen bending vibrations and influence of the quaternary structure change. **Biochem.** 21(6): 1132−1140.

Walker, F. A. (1994). **Encyclopedia of Inorganic Chemistry: Iron Porphyrin Chemistry.** Vol 4, John Wiley & Sons, pp. 1785−1786.

Webster, G. T. (2005). **Resonance Raman Micro-Spectroscopy in Malaria Research.** Bachelor Thesis, Monash University, Clayton, Victoria.

Webster, G. T., Tilley, L., Deed, S., McNaughton, D., Wood, B. R. (2008). Resonance Raman spectroscopy can detect structural changes in haemozoin (malaria pigment) following incubation with chloroquine in infected erythrocytes. **FEBS Letters** 582(7): 1087−1092.

Wood, B. R. (2004). Personal communication, unpublished results.

Wood, B. R., Langford, S. J., Cooke, B. M., Glenister, F. K., Lim J., McNaughton, D. (2003). Raman imaging of hemozoin within the food vacuole of *Plasmodium falciparum* trophozoites. **FEBS Letters** 554(3): 247−252.

Wood, B. R., Langford, S. J., Cooke, B. M., Lim, J., Glenister, F. K., Duriska, M., Unthank, J. K., McNaughton, D. (2004). Resonance Raman spectroscopy reveals new insight into the electronic structure of β-hematin and malaria pigment. **J. Am. Chem. Soc.** 126(30): 9233−9239.

CHAPTER II

EXPERIMENTAL

2.1 Synthesis of *β*-Hematin

Synthesis of *β*-hematin was based on the literature method of Slater, Swiggard, and Orton (1991) using hematin from Sigma Aldrich. Hematin (0.0767 g, 0.2415 mmol) was dissolved in 24.5 mL 0.1 M aqueous sodium hydroxide and the porphyrin was then precipitated by the slow addition of glacial acetic acid (100 mmol, 5.7 mL). The suspension was then heated overnight at 70 °C, centrifuged at 5000 rpm for 5 min, and the supernatant decanted. The pellet was washed four times with distilled water, centrifuged and the solvent discarded. It was then re-suspended in 0.1 M Tris-hydrochloric acid buffer (0.16 g, 10 mL, 2 mmol) containing 2.5% sodium dodecyl sulfate and incubated at 37 °C for 30 min. The suspension was centrifuged at 5000 rpm for 5 min and the supernatant discarded. The solid was re-suspended in alkaline 0.1 M sodium bicarbonate buffer (10 mL, pH 8.6), centrifuged at 5000 rpm for 5 min, and the supernatant discarded. Washing with distilled water was repeated until the decantate became clear. The *β*-hematin pellet was dried over phosphorous pentaoxide overnight to give 84% yield.

Hydrothermal synthesis is another method to synthesize *β*-hematin. Hematin (~0.0377 g, 60 μmol) in 8 mL 0.1 M aqueous sodium hydroxide acidified with 2.8

mL of glacial acetic acid (49 mmol) or 4.0 mL of propionic acid (49 mmol) was placed in a reaction bomb and heated in the oven at 180 °C for 2, 3, and 5 days.

Preparation of 0.1 M Aqueous Sodium Hydroxide

0.40 g solid sodium hydroxide (BDH, M.W. = 40.00) was dissolved in 40 mL of distilled water

Preparation 0.1 M Tris-hydrochloric Acid Buffer

0.16 g Tris-hydrochloric acid buffer (Trizma® hydrochloride, reagent grade, minimum 99% redox titration, M.W. = 157.6) was dissolved in 10 mL of distilled water.

Preparation of 2.5% Sodium Dodecyl Sulfate

0.25 g sodium dodecyl sulfate (Sigma Aldrich, M.W. = 288.38) was dissolved in 10 mL of 0.1 M Tris-hydrochloric acid buffer.

Preparation of 0.1 M Sodium Bicarbonate Buffer

0.084 g sodium bicarbonate (BDH, M.W. = 84.01) was dissolved in 10 mL of distilled water. The measured pH of the buffer was 8.6.

2.2 Synthesis of μ-Oxo Dimer [Fe(TPP)]$_2$O and [Fe(OEP)]$_2$O

Fe(TPP)Cl and Fe(OEP)Cl were purchased from Sigma Aldrich. The synthesis of μ-oxo dimers followed the method of Cheng, Hobbs, Debrunner, Erlebacher, Shelnutt, and Scheidt (1995). Monomer (approximately 20 mg) was dissolved in 0.5 mL dichloromethane and shaken vigorously with 5 mL 2 M potassium hydroxide, in a separatory funnel for 10 min. Distilled water was added, the dichloromethane layer was separated from the mixture, and sodium sulfate was added to remove water. The

product was filtered on a fritted glass filter to remove the sodium sulfate. The microcrystalline μ-oxo dimers were recrystallized from dichloromethane by vapor diffusion with hexane.

Preparation of 2 M Potassium Hydroxide

1.12 g solid potassium hydroxide (BDH, M.W. = 56.11) was dissolved in 10 mL of distilled water.

2.3 Synthesis of Fe(OEP)picrate

Fe(OEP)Cl from Sigma Aldrich (0.0153 g, 25 μmol) was dissolved in 5 mL of dichloromethane followed by addition of 2 mL 0.0185 M (37 μmol) of picric acid solution. Subsequently, ~4 mL ethanol and ~6−8 mL dimethylsulfoxide were added. The mixture was stirred vigorously until it was homogenous, then 1 mL methanol was added and the solution allowed to stand at room temperature for 3 days. The dark blue solid product was filtered off and washed with ethanol.

Preparation of 0.0185 M Picric Acid

13 g picric acid (Fluka, M.W. = 229.11, D = 1.005 g/cm^3) was dissolved in 1 L of distilled water.

2.4 Instrumentations

Scanning Electron Microscopy

Scanning electron microscopy utilized a JEOL 5410LV instrument with an accelerating voltage of 25,000 for β-hematin and a JSM 6400 instrument with an accelerating voltage of 20,000 for hematin, respectively. Samples were coated with

carbon black to avoid surface charging and images obtained in low vacuum mode. Typical vacuum conditions for image acquisition were 20 Pa in the sample chamber.

Electronic Absorbance Spectra for Solid Phase

Electronic absorption spectra of samples were recorded using a J&M MSP800 UV−visible spectrometer equipped with a Leica DM4000M microscope and an ×40 quartz UV−visible objective with a 7×7 μm aperture size. UV−visible absorbance spectra were recorded in the spectral range 940−500 nm as 20 scan accumulations using a 1.2 sec integration time per scan.

Electronic Absorbance Spectra for Solution Phase

Electronic absorption spectra of samples were recorded on a Cary 100 Bio UV−visible spectrometer using dichloromethane as solvent except picric acid solution using distilled water as a solvent.

Attenuated Total Reflection Fourier Transform Infrared Spectroscopy (ATR/FTIR)

ATR/FTIR spectra of solid products were recorded on a Bruker Equinox spectrometer by placing sample on the window of an ATR cell and recording spectra in absorption mode at 5 cm^{-1} resolution with 60 scans.

Fourier Transform Infrared Spectroscopy (FTIR)

FTIR spectra of solid products were recorded on a Spectrum GX Perkin Elmer spectrometer. KBr pellets were prepared from each dried sample and placed on the window for recording spectra in transmission mode at 5 cm^{-1} resolution with 50 scans.

Fourier Transform Infrared Microscope Spectroscopy

FTIR spectra of samples were recorded with a Varian 600-UMA FTIR microscope equipped with an HgCdTe detector and coupled to a Varian 7000 FTIR spectrometer. Spectra were recorded in reflection mode on Kevley^{TM} "low e" IR reflective slide substrates at 6 cm^{-1} resolution with 128 co-added scans, apodized using a Blackman Harris 4 term function and zero filled by a factor of 2.

Synchrotron Fourier Transform Infrared Spectroscopy (Synchrotron-FTIR)

Synchrotron-FTIR spectra of solid products were recorded on a Nicolet Magna-IR860 FTIR microspectrometer in reflection mode by placing sample on a Kevley^{TM} IR reflective slide and recording spectra in absorption mode at 4 cm^{-1} resolution with 80 scans.

Resonance Raman (RR) Spectroscopy

RR spectra of products were recorded on a Renishaw system 2000 spectrometer using a 413 nm (or 514 nm) excitation line (Spectra Physics Ar^{+} Stabilite 2017 laser system), a 633 nm excitation line generated by Coherent 45 mW helium-neon laser, or a 782 nm (or 830 nm) excitation line generated by diode lasers (Renishaw RM2000) in a back scattering geometry. The laser power on the sample was approximately 39, 130, 160, 500, and 600 μW for the excitation wavelengths 413, 514, 633, 782, and 830 nm, respectively. The system was equipped with an Olympus optical microscope and a Zeiss ×60 water immersion objective to enable spectral acquisition in water to prevent the thermal degradation of the solid samples. All spectra presented have been smoothed and normalized after interactive baseline correction using the concave rubber band algorithm in the OPUS software.

Cambridge Structural Database Search

The Cambridge Structural Database, CSD, Version 5.27 (Cambridge Structure Database, 2006) was searched to give an indication of the frequency of Fe(TPP) and Fe(OEP) derivatives in the structural literature. Four structural fragments were utilized to search for five-coordinate Fe(TPP) (Figure 2.1), five-coordinate Fe(OEP) (Figure 2.2), five-coordinate Fe(OEP) with an oxygen bound axial ligand (Figure 2.3), and oxo bridged iron porphyrin dimers (Figure 2.4). The number of hits for each of these fragments is 144, 152, 20, and 33, respectively.
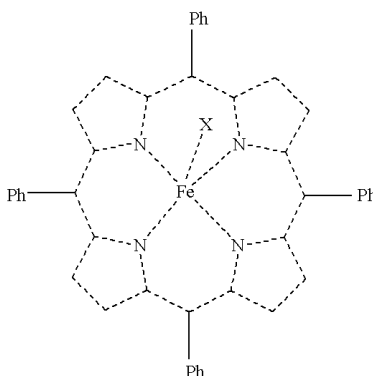
Figure 2.1 The Fe(TPP)X fragment for the CSD search.
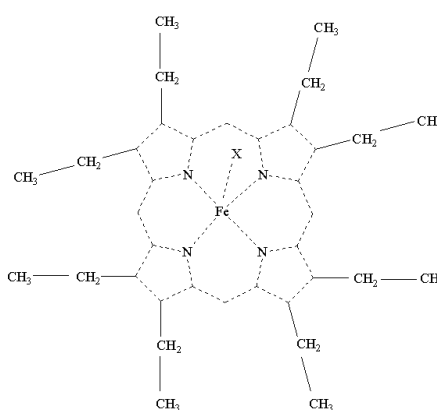
Figure 2.2 The Fe(OEP)X fragment for the CSD search.
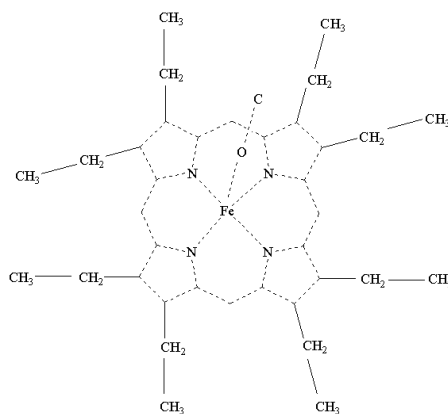
Figure 2.3 The Fe(OEP)(OC) fragment for the CSD search.
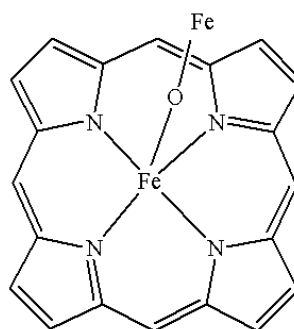
Figure 2.4 The Fe−O−Fe fragment of iron porphyrin for the CSD structure search.

Refcodes are XETXUP, KANYUT, PPORFE01, TOYRUU, YIKJOR, and YIKJOR01 for β-hematin, Fe(TPP)Cl, [Fe(TPP)]$_2$O, Fe(OEP)Cl, triclinic [Fe(OEP)]$_2$O, and monoclinic [Fe(OEP)]$_2$O, respectively as the lists in Table 2.1.

Crystallographic Geometry Calculations

Supramolecular interaction contact distances and angles were calculated with *ORTEP-III* (Burnett and Johnson, 1996) and are reported with the conventional D−H···A notation or with D−H···(A−A') notation where the acceptor position is the midpoint of the A−A' bond of the relevant aromatic system. Coordinates for Fe(TPP)Cl (Scheidt and Finnegan, 1989), [Fe(TPP)]$_2$O (Swepston and Ibers, 1985),

Fe(OEP)Cl (Senge, 2005), triclinic [Fe(OEP)]$_2$O, monoclinic [Fe(OEP)]$_2$O (Cheng, Hobbs, Debrunner, Erlebacher, Shelnutt, and Scheidt, 1995), and β-hematin (Pagola, Stephens, Bohle, Kosar, and Madsen, 2000) were obtained from the CSD where they are identified by the Refcodes given in Table 2.1.

The intermolecular distance between porphyrin cores in Fe(TPP)Cl for refcode KANYUT (Scheidt and Finnegan, 1989) and β-hematin for XETXUP (Pagola, Stephens, Bohle, Kosar, and Madsen, 2000) were not given in the original papers. They were calculated by *DIAMOND* (Crystal Impact, 2006). The porphyrin core consisting of 24 atoms of the macrocylic ring which parallel with another porphyrin core is selected. The "Plan Through Atoms" is open to create the first plane in the structure picture. Another porphyrin core is selected for the second plane. When both first and second plane were selected, the distance and angle between planes would be displayed.

The distance between adjacent mean planes was calculated as the perpendicular interplanar separation between inversion related porphyrin cores as illustrated in Figure 2.5.

Density Functional Theory (DFT) Calculations

To assist in the analysis of IR and Raman spectra, a series of density functional theory calculations were performed at the B3LYP/6-31G(d) level using the Gaussian03 suite of programs (Frisch *et al.*, 2004). Geometry optimizations preceded vibrational frequency calculations, with wavenumber values scaled by factor 0.97.

Time-dependent Density Functional Theory (TD-DFT)

The structure of Fe(TPP)Cl was optimized at the B3LYP/TZVP level of theory using the program package Gaussian 03 (Revision E.01) (Frisch *et al.*, 2004)

starting from a X-ray crystallography structure derived from Scheidt and Finnegan (1989). The optimization was followed by frequency calculation at the corresponding level to assure finding the local minimum on the potential energy surface. Excited state calculations were performed using TD-DFT at the same level of theory. The number of excited states was limited to 50 which covers the energy states up to 361 nm.

Table 2.1 Published Structures for Malaria Pigment Model Systems Used in this Study.

Model Complex	Temperature (K)	Unit cell	Space group number	#[a]	Refcodes
β-hematin Pagola *et al.* (2000)	room temp	Triclinic Z = 2	*P−1*	2	XETXUP
Fe(TPP)Cl Hoard *et al.* (1967)		Tetragonal Z = 2	*I4, I−4, I4/m*[b]	87[b]	[c]
Fe(TPP)Cl Scheidt *et al.* (1989)	293	Monoclinic Z = 4	*P2₁/n*	14	KANYUT
[Fe(TPP)]₂O Fleischer *et al.* (1969)		Orthorhombic Z = 4	*C2cb*[d]	41	[c]
[Fe(TPP)]₂O Hoffman *et al.* (1972)	295	Orthorhombic Z = 4	*C2ca*[d]	41	PRORFE10
[Fe(TPP)]₂O Swepston *et al.* (1985)	122	Orthorhombic Z = 4	*C2cb*[d]	41	PRORFE01
Fe(OEP)Cl Senge (2005)	126	Monoclinic Z = 4	*P2₁/c*	14	TOYRUU
[Fe(OEP)]₂O Cheng *et al.* (1995)	20	Triclinic Z = 2	*P−1*	2	YIKJOR
[Fe(OEP)]₂O Cheng *et al.* (1995)	20	Monoclinic Z = 4	*P2₁/c*	14	YIKJOR01

[a] Space group number in the *International Tables for Crystallography* (Hahn, 2002).
[b] Space group not unambiguously determined by the X-ray diffraction data. The centrosymmetric *I4/m* was assumed for the structure refinement.
[c] No Refcodes in CSD.
[d] Same space group. Space group No. 41 contains a double glide plane, sometimes represented with diffraction symbol *C−c(ab)*. Fleischer and Srivastava (1969) and Swepston and Ibers (1985) chose to resolve the symbol ambiguity by using the *C2cb* symbol while Hoffman, Collins, Day, Fleischer, Srivastava and Hoard (1972) chose the *C2ca* symbol. The standard symbol for this double glide space group has been changed to *Aea2* in the 2002 edition of the *International Tables for Crystallography* (Hahn, 2002).
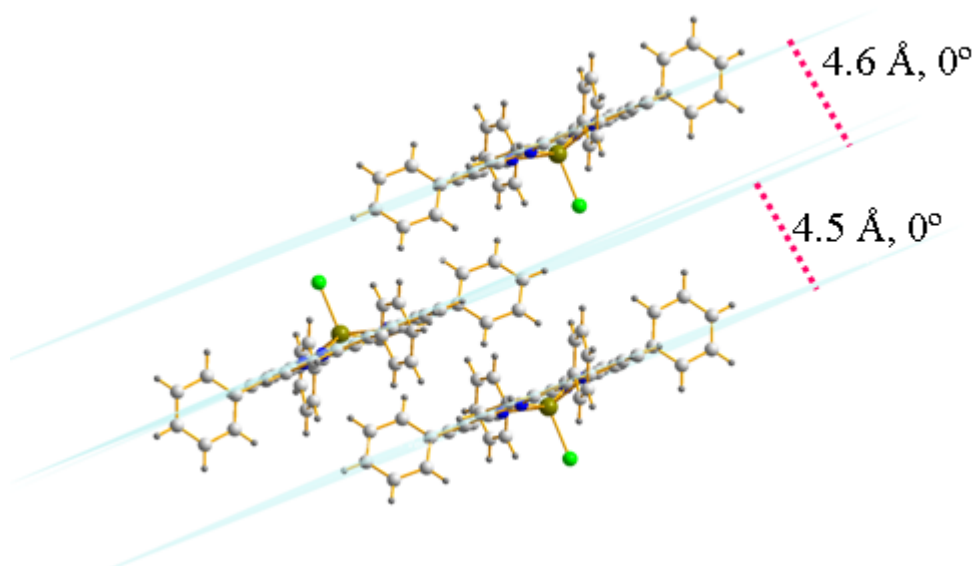
Figure 2.5 Mean plane separation in Fe(TPP)Cl. (not reported by Scheidt and Finnegan (1989), but based on their X-ray crystal structure).

2.5 References

Beurskens, P. T., Beurskens, G., Bosman, W. P., de Gelder, R., Granda, S., Gould, R. O., Israël, R., Smits, J. M. M. (1996). *DIRDIF-96*: *A Computer Program System for Crystal Structure Determination by Patterson Methods and Direct Methods Applied to Difference Structure Factors*, Technical Report of the Crystallography Laboratory, University of Nijimegen, Nijmegen, The Netherlands.

Blessing, R. H. (1997). Outlier treament in data merging. **J. Appl. Cryst.** 30(4): 421–426.

Burnett, M. N., Johnson, C. K. (1996). *ORTEP-III*: *Oak Ridge Thermal Ellipsoid Plot Program for Crystal Structure Illustrations*, Report ORNL-6895, Oak Ridge National Laboratory, Oak Ridge TN.

Cambridge Structural Database. (2006) version 5.27, updates August 2006.

Cheng, B., Hobbs, J. D., Debrunner, P. G., Erlebacher, J., Shelnutt, J. A., Scheidt, W. R. (1995). An unusual near-eclipsed porphyrin ring orientation in two crystalline forms of (μ-oxo)bis[(octaethylporphinato)iron(III)]. Structural and molecular mechanics studies. **Inorg. Chem.** 34(1): 102−110.

Crystal Impact. (2006). *DIAMOND*. version 3.1. Crystal Impact GbR. Bonn, Germany.

Duisenberg, A. J. M. (1992). Indexing in single-crystal diffractometry with an obstinate list of relections. **J. Appl. Cryst.** 25(2): 92−96.

Duisenberg, A. J. M., Kroon-Batenburg, L. M. J., Schreurs, A. M. M. (2003) An intensity evaluation method: *EVAL*-14. **J. Appl. Cryst.** 36: 220−229.

Hoard, J. L., Cohen, G. H., Glick, M. D. (1967). The stereochemistry of the coordination group in an iron(III) derivative of tetraphenylporphine. **J. Am. Chem. Soc.** 89(9): 1992−1996.

Hoffman, A. B., Collins, D. M., Day, V. W., Fleischer, E. B.; Srivastava, T. S., Hoard, J. L. (1972). The crystal structure and molecular stereochemistry of μ-oxo-bis[$\alpha,\beta,\gamma,\delta$-tetraphenylporphinatoiron(III)]. **J. Am. Chem. Soc.** 94(10): 3620−3626.

Farrugia, L. J. (1997) *ORTEP*-3 for Windows- a version of *ORTEP-III* with a graphic user interface (GUI). **J. Appl. Cryst.** 30(1): 565.

Fleischer, E. B., Srivastava, T. S. (1969). The structure and properties of μ-oxo-bis(tetraphenylporphineiron(III)). **J. Am. Chem. Soc.** 91(9): 2403−2405.

Frisch, M. J., Trucks, G. W., Schlegel, H. B., Scuseria, G. E., Robb, M. A., Cheeseman, J. R., Montgomery, Jr., J. A., Vreven, T., Kudin, K. N., Burant, J. C., Millam, J. M., Iyengar, S. S., Tomasi, J., Barone, V., Mennucci, B., Cossi, M., Scalmani, G., Rega, N.; Petersson, G. A., Nakatsuji, H., Hada, M., Ehara, M., Toyota, K., Fukuda, R., Hasegawa, J., Ishida, M., Nakajima, T., Honda, Y., Kitao, O., Nakai, H., Klene, M., Li, X., Knox, J. E., Hratchian, H. P., Cross, J. B., Bakken, V., Adamo, C., Jaramillo, J., Gomperts, R., Stratmann, R. E., Yazyev, O., Austin, A. J., Cammi, R., Pomelli, C., Ochterski, J. W., Ayala, P. Y., Morokuma, K., Voth, G. A., Salvador, P., Dannenberg, J. J., Zakrzewski, V. G., Dapprich, S., Daniels, A. D., Strain, M. C., Farkas, O., Malick, D. K., Rabuck, A. D., Raghavachari, K., Foresman, J. B., Ortiz, J. V., Cui, Q., Baboul, A. G., Clifford, S., Cioslowski, J., Stefanov, B. B., Liu, G., Liashenko, A., Piskorz, P., Komaromi, I., Martin, R. L., Fox, D. J., Keith, T., Al-Laham, M. W., Johnson, B., Chen, W., Wong, M. W., Gonzalez, C., and Pople, J. A. (2004). Gaussian, Inc., Wallingford CT.

Hahn, T., (2002). **International Tables for Crystallography: Space-Group Symmetry**. Volume A, fifth edition, International Union of Crystallography/Kluwer Academic Publishers, Dordrecht/Boston/London.

Pagola, S., Stephens, P. W., Bohle, D. S., Kosar, A. D., Madsen, S. K. (2000). The structure of malaria pigment β-hematin. **Nature** 404(6775): 307–310.

Scheidt, W. R., Finnegan, M. G. (1989). Structure of monoclinic chloro(meso-tetraphenylporphyrinato)iron(III). **Acta Cryst. C** 45: 1214–1216.

Senge, M. O. (2005). Chloro(2,3,7,8,12,13,17,18-octaethylporphinato)iron(III). **Acta Cryst. E** 61: m399–m400.

Slater, A. F. G., Swiggard, W. J., Orton, B. R. (1991). An iron-carboxylate bond links the heme units of malaria pigment. **Proc. Natl. Acad. Sci. USA** 88(2): 325−329.

Swepston, P. N., Ibers, J. A. (1985). Redetermination of the structure of μ-oxo-bis [(5,10,15,20-tetraphenylporphyrinato)iron(III)] at 122 K, [$Fe_2O(C_{44}H_{28}N_4)_2$]. **Acta Cryst. C** 41: 671−673.

CHAPTER III

β-HEMATIN SYSTHESIS AND CHARACTERIZATION[*]

3.1 Introduction

Malaria is an infectious disease that still represents a serious public health problem especially for sub-Saharan Africa and Southeast Asia, including Thailand and its bordering nations. Malaria interferes with the oxygen transport mechanism as the parasites (such as *Plasmodium falciparum*) degrade hemoglobin. The degradation releases ferrous protoporphyrin IX, Fe(PPIX), which is potentially toxic to the parasite. The parasite converts Fe(PPIX) to hemozoin, an inert crystalline solid also called malaria pigment, that deposits in the food vacuole of the parasite (Slater Swiggard, and Orton, 1991). Egan (2008) reports that malaria pigment had been observed earlier than the malaria parasite itself by Italian physician Lancisi in the early 18th century. There has been great interest in studying malaria pigment which is chemically (Fitch and Kanjanaggulpan, 1987), spectroscopically (Wood, Langford, Cooke, Glenister, Lim, and McNaughton, 2003), and from synchrotron powder diffraction, crystallographically (Pagola, Stephens, Bohle, Kosar, and Madsen, 2000) indistinguishable from β-hematin. Knowledge of the structure of hemozoin is important in developing new antimalarial drugs to target hemozoin formation.

---

[*] Published as Conference Proceedings, Puntharod, R., Haller, K. J., McNaughton, D., Wood, B. R. (2008). 34th Congress on Science and Technology of Thailand.

A challenge that remains is to produce single crystals of β-hematin of suitable size to study by single crystal X-ray crystallography to obtain a definitive structure. Several reports exhibit the size and images of malaria pigment and β-hematin crystals. The approximate size of β-hematin obtained by acidification of hematin (iron(III) protoporphyrin IX hydroxide, Fe(PPIX)OH) and hemin (iron(III) protoporphyrin IX chloride, Fe(PPIX)Cl) with acetic acid is 1 μm (Egan, Hempelmann, and Mavuso, 1999) and 0.2 μm in length (Bohle, Kosar, and Stephens, 2002), respectively. In contrast the crystals resulting from the abstraction of hydrochloric acid from hemin with anhydrous noncoordinating-base are up to 20 times larger (Bohle, Kosar, and Stephens, 2002). The size of β-hematin grown in methanol-dimethysulfoxide and chloroform is 0.5−10 μm long and 0.05−0.5 μm wide (Solomonov, Osipova, Feldman, Baehtz, Kristian, Robinson, Webster, McNaughton, Wood, Weissbuch, and Leiserowitz, 2007). β-hematin was synthesized by anhydrous dehydrohalogenation of hemin which gave a crystal length of about 5−30 μm (Frosh, Koncarevic, Zedler, Schmitt, Schenzel, Becker, and Popp, 2007). Unfortunately, no method has succeeded in providing a single crystal suitable for single crystal X-ray crystallography.

Hydrothermal synthesis is currently very popular to synthesize inorganic compounds, especially those with low solubility. Hydrothermal synthesis is the only technique known today to synthesize a large single crystal of quartz. The conditions of the method utilize elevated pressure and temperature in the presence of water (Byrappa and Yoshimaru, 2001). The hydrothermal method has not been reported previously as a method to synthesize β-hematin. In this work β-hematin was

synthesized by the hydrothermal method from dissolved solid hematin in 0.1 M NaOH solution by acidifying with acetic acid or propionic acid followed by heating in the oven for various times at various temperatures. The method succeeded in producing β-hematin as verified by a comparison of FTIR spectra of the products and β-hematin from the literature. Unfortunately, the size of the product crystals is not sufficient for single crystal X-ray structural characterization.

The structure of hematin, shown in Figure 3.1, consists of an iron ion and the porphyrin core is another example of a heme complex. Fe(PPIX) is the prosthetic group for a variety of hemoproteins such as hemoglobin, myoglobin, cytochromes, catalases, and peroxidases (Trivedi, Chand, Maulik, and Bandyopadhyay, 2005). Hematin has a hydroxide ligand at the axial position of the central iron(III) nucleus and two propionic acid groups in the periphery of the porphyrin ring. Hematin is used as the starting material to synthesize β-hematin by polymerization under acidic conditions (Slater, Swiggard, and Orton, 1991).

Resonance Raman (RR) spectroscopy is a powerful tool to provide stereochemical and electronic structural information for metalloporphyrins. Iron porphyrins have been especially studied (Spiro and Li, 1988). The vibrational frequencies of a number of structure-sensitive metallpophyrin Raman marker lines are observed to shift in response to changes in bond strength, geometry, oxidation state, coordination number, and spin state of the central metal ion (Spiro and Strekas, 1974; Kitagawa and Ozaki, 1987). The correlation between the positions of these Raman bands and metal oxidation state or metal-to-porphyrin plane distances makes structural information accessible by RR spectroscopy (Spaulding, Chang, Yu, and

Felton, 1975). This information is complementary to that obtained from infrared spectroscopy and X-ray crystallography.
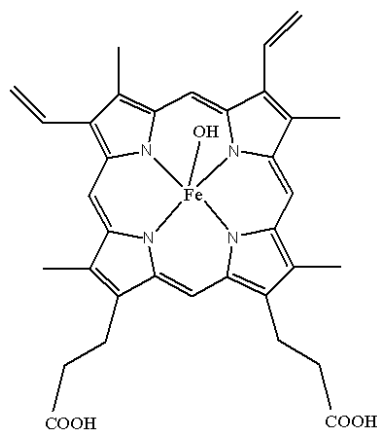
Figure 3.1 Schematic diagram of the structure of hematin.

RR spectroscopy reports have suggested new insight into the electronic structure of β-hematin and malaria pigment may be gained from the extraordinary band enhancement observed when exciting with near-IR excitation wavelengths in β-hematin compared with hemin. Of particular interest is the appearance of much greater enhancement of the totally symmetric vibrational mode, ν_4 in the Raman spectra of β-hematin compared to hemin when applying near-IR excitation wavelengths (Wood, Langford, Cooke, Lim, Glenister, Duriska, Unthank, and McNaughton, 2004). This motivated us to study the enhancement of the β-hematin spectral modes compared to these of hematin (Fe(III) with the hydroxide ligand at the axial position), the starting material to synthesize β-hematin under acidic conditions.

3.2 Experimental

Synthesis of *β*-hematin

Synthesis of *β*-hematin was based on the literature method (Slater, Swiggard, and Orton, 1991) using hematin from Sigma Aldrich.

Hydrothermal is another method to synthesize *β*-hematin by dissolving solid hematin in 0.1 M NaOH solution then acidifying with glacial acetic acid or propionic acid in a bomb reactor, followed by heating in the oven at 180 °C for various times.

Characterization of *β*-hematin

Scanning Electron Microscopy (SEM). SEM utilized a JEOL instrument model JEOL-5410LV. Operating conditions were an accelerating voltage of 25,000 eV for *β*-hematin and 20,000 eV for hematin. The sample was coated with carbon black to avoid surface charging and images were obtained in low vacuum mode. Typical vacuum conditions for image acquisition were 20 Pa in the sample chamber.

Attenuated Total Reflection Fourier Transform Infrared Spectroscopy (ATR/FTIR). ATR/FTIR spectra of solid products were recorded on a Bruker Equinox by placing the sample on the window of an ATR cell and recording spectra in absorption mode at 5 cm^{-1} resolution with 60 scans.

Fourier Transform Infrared Spectroscopy (FTIR). FTIR spectra of solid products were recorded on a Spectrum GX Perkin Elmer. KBr pellets were prepared from each dried sample and placed on the window and the spectra recorded in transmission mode at 4 cm^{-1} resolution with 50 scans.

Synchrotron Fourier Transform Infrared Spectroscopy (Synchrotron-FTIR). Synchrotron-FTIR spectra of solid products were recorded on a Nicolet

Magna-IR860 FTIR microspectrometer in reflection mode by placing the sample on a Keveley IR reflective slide and recording spectra in absorption mode at 4 cm^{-1} resolution with 80 scans.

Resonance Raman (RR) Spectroscopy. RR spectra of products were recorded on a Renishaw system 2000 spectrometer using a 413 nm (or 514 nm) excitation line (Spectra Physics Ar^{+} Stabilite 2017 laser system), a 633 nm excitation line generated by Coherent 45 mW helium-neon laser, or a 782 nm (or 830 nm) excitation line generated by diode lasers (Renishaw RM2000) in a back scattering geometry. The laser power on the sample was approximately 39, 130, 160, 500, and 600 μW for the excitation wavelengths 413, 514, 633, 782, and 830 nm, respectively. The system was equipped with an Olympus optical microscope and a Zeiss ×60 water immersion objective to enable spectral acquisition in water to prevent the thermal degradation of the solid samples only at 830 nm excitation wavelength. All spectra presented have been smoothed and normalized after interactive baseline-correction using the concave rubber band algorithm in the OPUS software.

3.3 Results and Discussion

The SEM image in Figure 3.2(a) illustrates the hematin starting material, while Figure 3.2(b) displays the crystalline β-hematin obtained from glacial acetic acid precipitation. The approximate size is 1 μm in length similar to typical malaria pigment crystallites (Bohle, Kosar, and Stephens, 2002). The SEM images of β-hematin are similar to images of crystallites from acid precipitation using hemin as starting chemical (Egan, Hempelmann, and Mavuso, 1999; Bohle, Kosar, and Stephens, 2002), except the sizes are different. In contrast the two alternative

procedures, acid-catalyzed method and anhydrous method in methanol, give significantly different morphologies and sizes (Bohle, Kosar, and Stephens, 2002). The morphology of the prepared β-hematin does not correspond to the morphology of the starting materials.

Figure 3.3 shows SEM images of synthetic β-hematin prepared by the hydrothermal method with acidification of hematin by glacial acetic acid followed by heating at 180 °C for 2, 3, and 5 days, and Figure 3.4 shows SEM images for analogous preparations using propionic acid with 2 and 3 day heating for comparison. Glacial acetic and propionic acid acidification provides crystals approximately 1 μm in length. In contrast the morphology of β-hematin prepared by acid precipitation, with glacial acetic acid acidification provided needles with better defined edges than those with propionic acid acidification.

(a)   (b)
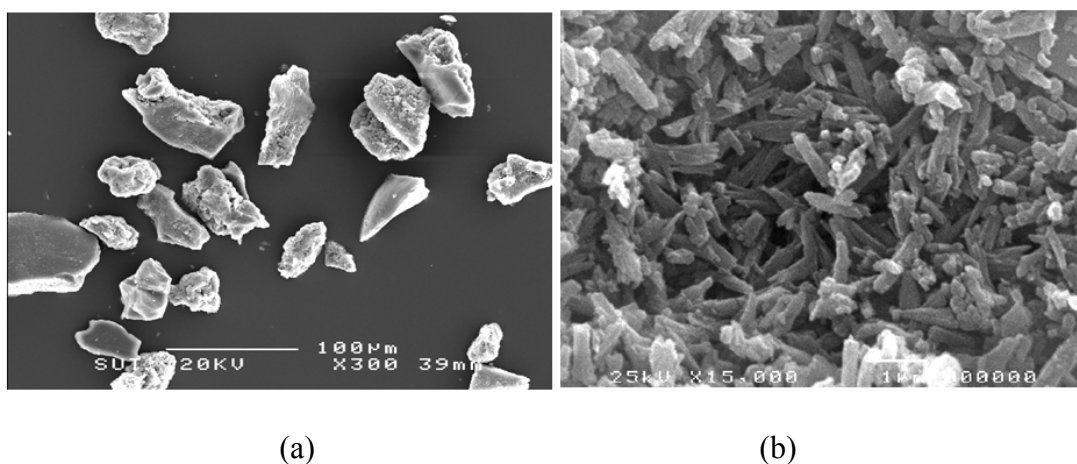
Figure 3.2 SEM images of hematin and β-hematin product from glacial acetic acid precipitation. (a) hematin starting material. (b) β-hematin.

(a)   (b)

(c)
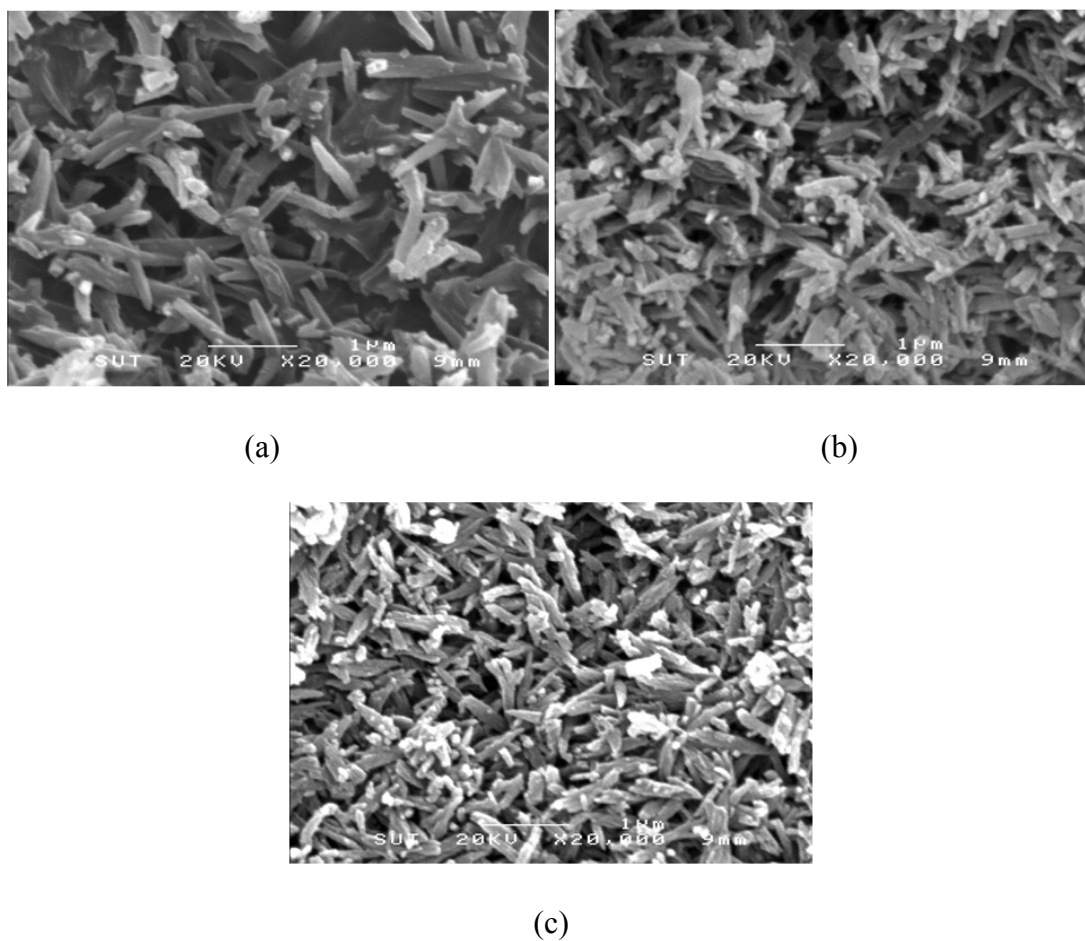
Figure 3.3 SEM images of hematin acidified by glacial acetic acid and heating at

180 °C. (a) 2 days (b) 3 days, and (c) 5 days.

(a)   (b)
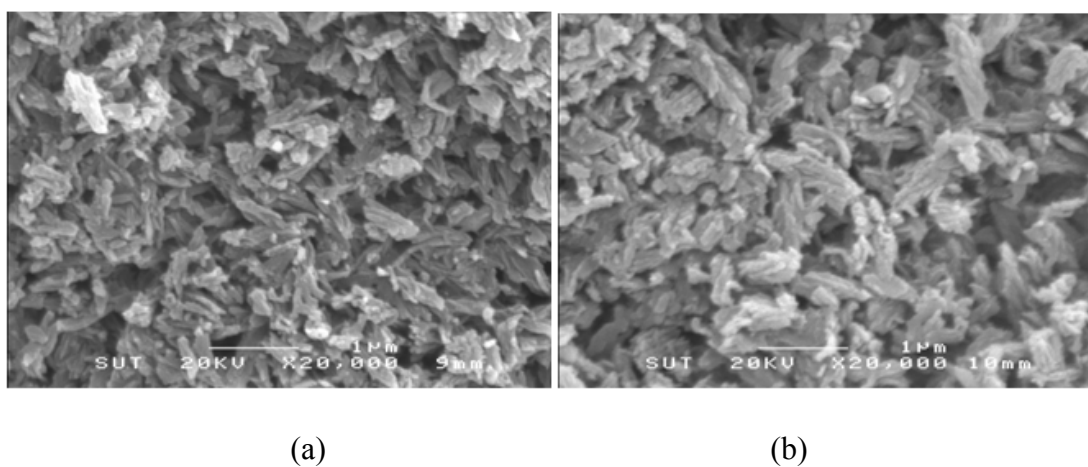
Figure 3.4 SEM images of hematin acidified by propionic acid and heating at

180 °C. (a) 2 days, and (b) 3 days.

The ATR/FTIR spectrum of β-hematin in Figure 3.5(a) and FTIR synchrotron spectrum in Figure 3.5(b) shows the intense absorbance band at 1660 and 1665 cm^{-1}, respectively for C=O stretching, and the bands at 1205 and 1212 cm^{-1} for C−O stretching typical of a ferric ion with unidentate carboxylate coordination from the carboxylate group coordinated to Fe in this pigment (Slater, Swiggard, and Orton, 1991). The intense band assigned to C=O stretching is absent and the band shape of C−O stretching is changed in hematin which shows the spectrum in Figure 3.5(c). The bands at 1709 and 1713 cm^{-1} in β-hematin and 1709 cm^{-1} in hematin are assigned to the hydrogen-bonded carboxylic acid groups that link adjacent molecules together (Wood, Langford, Cooke, Lim, Glenister, Duriska, Unthank, and McNaughton, 2004).

Figure 3.6 shows comparison of the FTIR spectra of synthetic β-hematin prepared based on the literature method (Slater, Swiggard, and Orton, 1991) and hematin products prepared by the hydrothermal method with glacial acetic or propionic acid acidification. The FTIR spectra of glacial acetic acid acidification products heated for 2 and 3 days are similar with β-hematin prepared by the literature method. However, the spectra of products of glacial acetic or propionic acid acidification heated more than 3 days are dissimilar to that of β-hematin prepared by the literature method. Propionic acid might not be the appropriate acid to prepare β-hematin by hydrothermal methods. Moreover, heating hematin acidified by glacial acetic acid in a reactor bomb longer than 3 days, results in alteration of the band at 1660 and loss of the band at 1211 cm^{-1} assigned to C=O and C−O stretching, respectively. The disappearance of these typical bands, normally observed in β-

hematin, indicates that heating under these conditions might damage the carboxylate linkage.
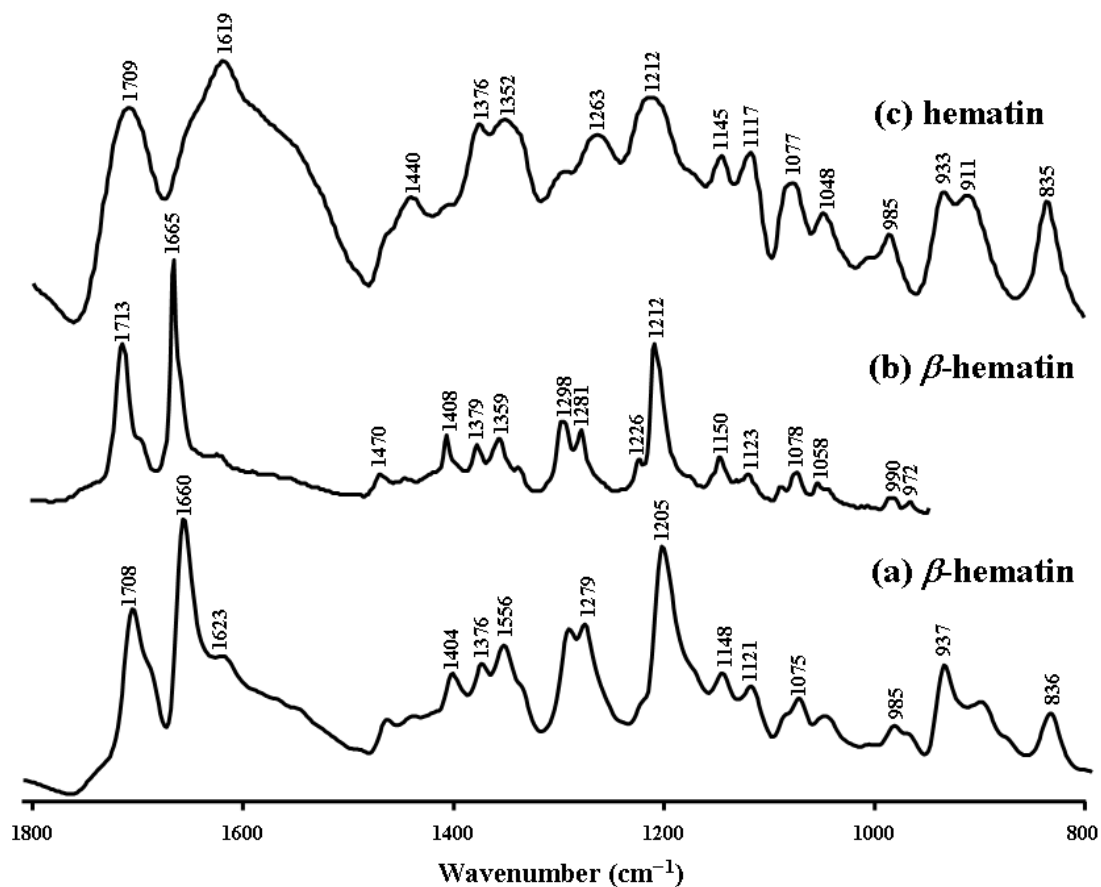
Figure 3.5 FTIR spectra of hematin and β-hematin. (a) ATR/FTIR spectrum of β-hematin, (b) FTIR synchrotron spectrum of β-hematin, and (c) ATR/FTIR spectrum of hematin.
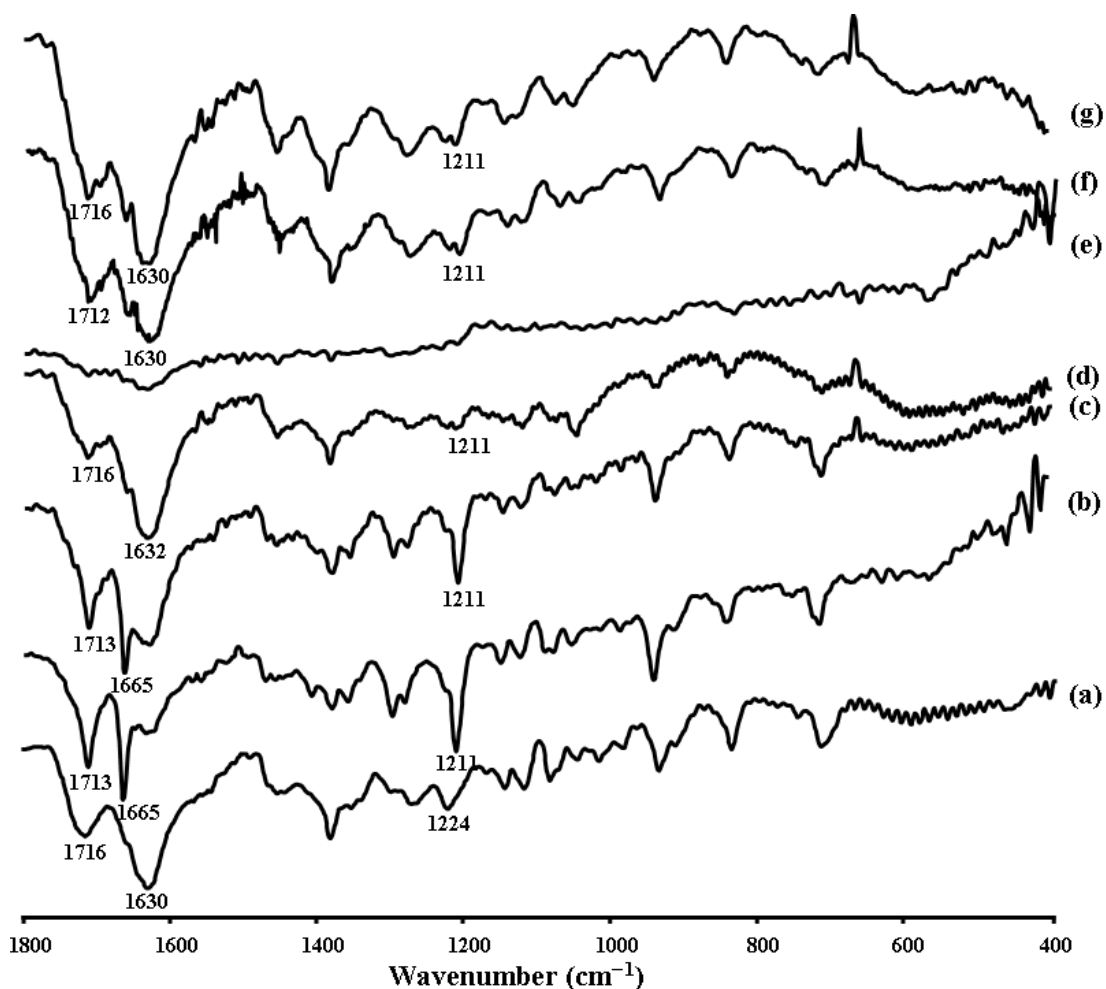
Figure 3.6 FTIR spectra of hematin and β-hematin products from various reaction conditions. (a) hematin, (b) synthetic β-hematin prepared by literature method, hematin acidified by glacial acetic acid heating at 180 °C for (c) 2 days (d) 3 days (e) 5 days, hematin acidified by propionic acid heating at 180 °C for (f) 2 days, and (g) 3 days by the hydrothermal method.
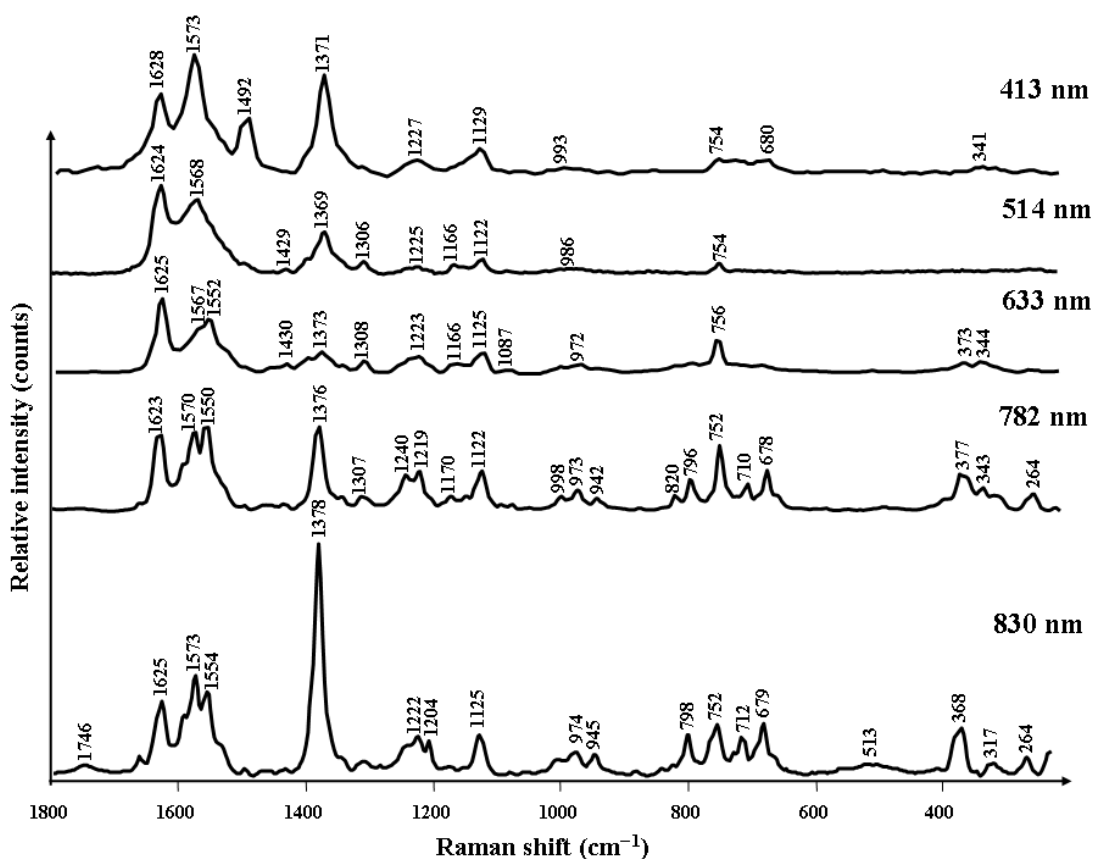
Figure 3.7 RR spectra of β-hematin in solid phase recorded using a variety of excitation wavelengths. The spectra are normalized with the totally symmetric mode v_{10}.

Figures 3.7 and 3.8 display the Raman spectra collected for β-hematin and hematin, respectively using 413, 514, 633, 782, and 830 nm excitation wavelengths. To facilitate comparison, all the spectra are normalized to the in-plane asymmetric stretching of the porphyrin ring $v_{10}(v(C_\alpha C_m)_{asym})$ at 1620–1633 cm^{-1} because of its high intensity at every excitation wavelength, both for β-hematin and hematin. Excitation into the Soret band using 413 nm laser line produces strong bands in β-hematin and hematin including the A_{1g} totally symmetric mode bands at 1567–1577,

1490–1498, and 1369–1378 cm^{-1} assigned to $\nu_2(\nu(C_\beta C_\beta))$, $\nu_3(\nu(C_\beta C_\beta))$, and $\nu_4(\nu(\text{pyrrole half-ring})_{sym})$, respectively. Excitation at 514 nm, close to the Q band, results in a decrease in the relative intensities of ν_2, ν_3, and ν_4 in β-hematin and hematin while the pyrrole-breathing and deformation modes at ~755 cm^{-1} start to increase. Excitation with 633 nm results in decreasing ν_2 and ν_4 and the complete absence of ν_3. In spectra of β-hematin the ~755 cm^{-1} band continues to increase along with the out-of-plane and metal–ligand modes (400–300 cm^{-1}). The spectra of both β-hematin and hematin recorded at 782 and 830 nm excitation wavelengths, show enhanced ν_2 and ν_4 modes with ν_3 not enhanced, as well as enhanced bands at ~755 and 400–300 cm^{-1}.

The Raman spectrum of β-hematin exhibits ν_{10}, the characteristic frequency of five-coordinate iron(III) at ~1625 cm^{-1} (Kitagawa and Ozaki, 1987), and ν_4 the oxidation state marker band sensitive to high-spin iron(III) at ~1375 cm^{-1} (Burke, Kincaid, and Spiro, 1978). Thus β-hematin is interpreted to be five-coordinate high-spin iron(III) corresponding with the previously reported crystallographic data (Pagola, Stephens, Bohle, Kosar, and Madsen, 2000) and a recent EXAFS report confirming that the oxidation state of iron is close to three (Walczak, Lawniczak-Jablonska, and Sienkiewicz, 2005).

The relative Raman intensities of β-hematin and hematin are presented in Figure 3.9. The spectra show similar enhancement when applying 413 and 514 nm excitation wavelengths. However, the enhancement is much more in β-hematin compared to hematin for excitation wavelengths 633, 782, and 830 nm even though both of them have the same stereochemistry and square-pyramidal geometry with the Fe(III)

displaced out of the porphyrin plane towards the oxygen atom coordinated axial ligand. The greater enhancement indicates more hydrogen bond interactions in β-hematin than in hematin.
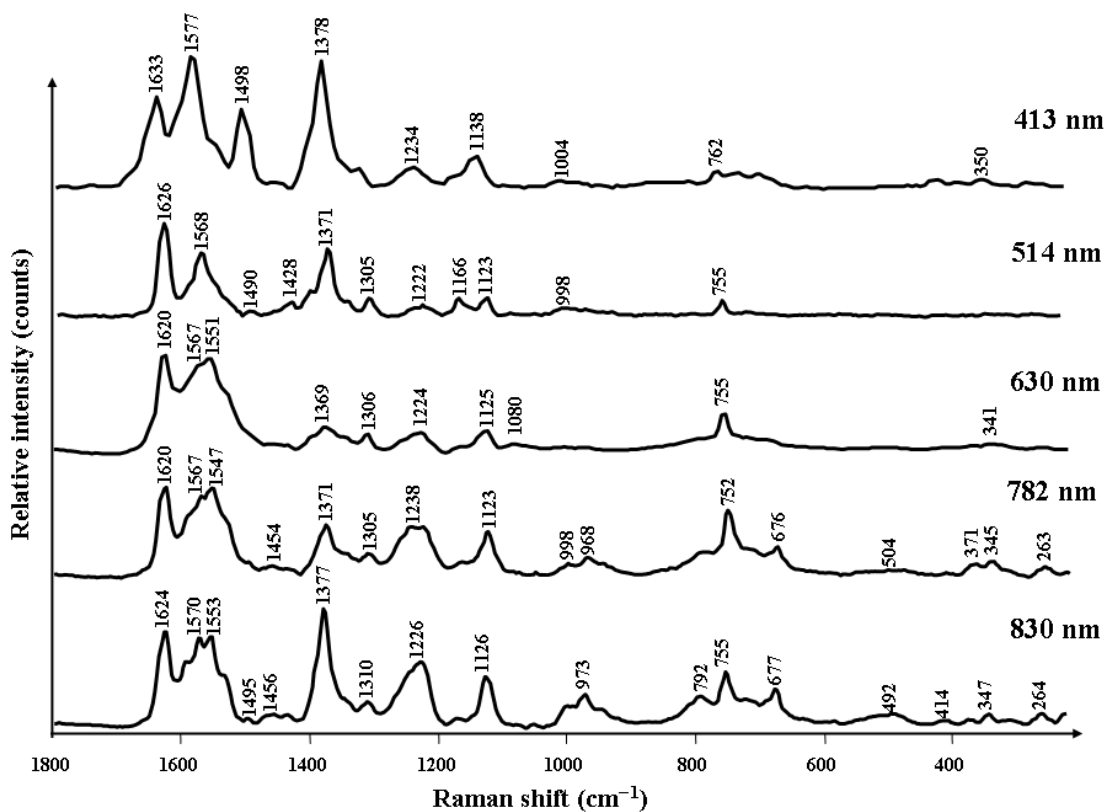
Figure 3.8 RR spectra of hematin in solid phase recorded using a variety of excitation wavelengths. The spectra are normalized with the totally symmetric mode ν_{10}.
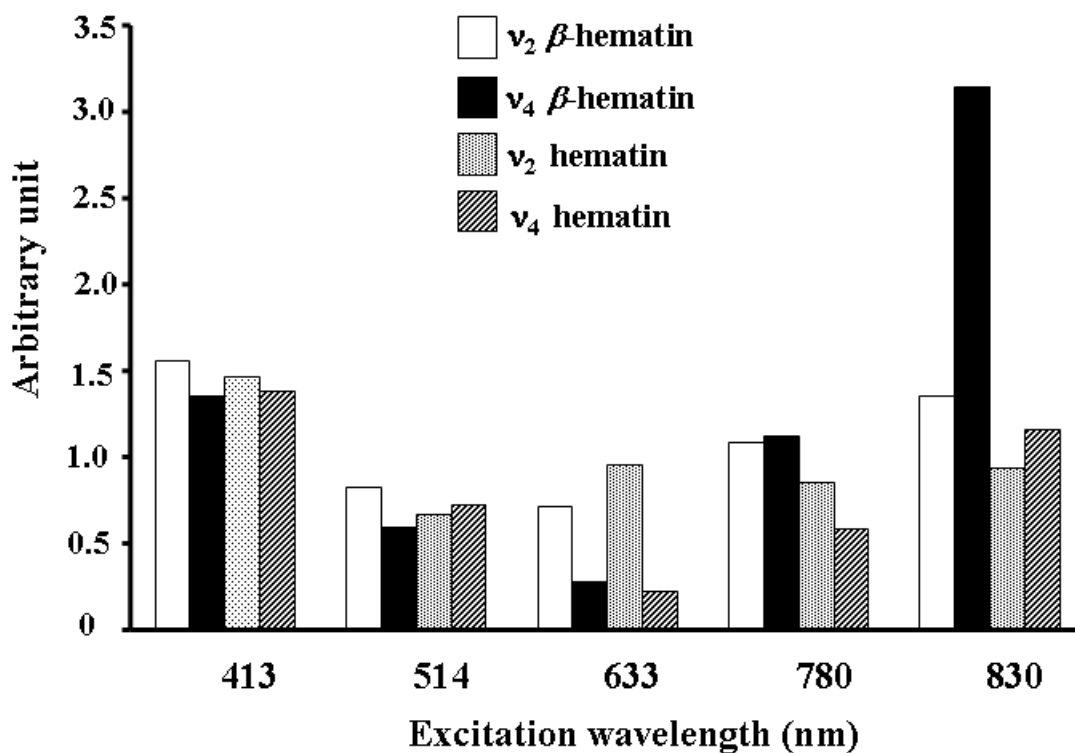
Figure 3.9 The relative Raman intensity of the totally symmetric modes ν_2 and ν_4 as a function of wavelength for β-hematin and hematin. The spectra are normalized with the totally symmetric mode ν_{10}.
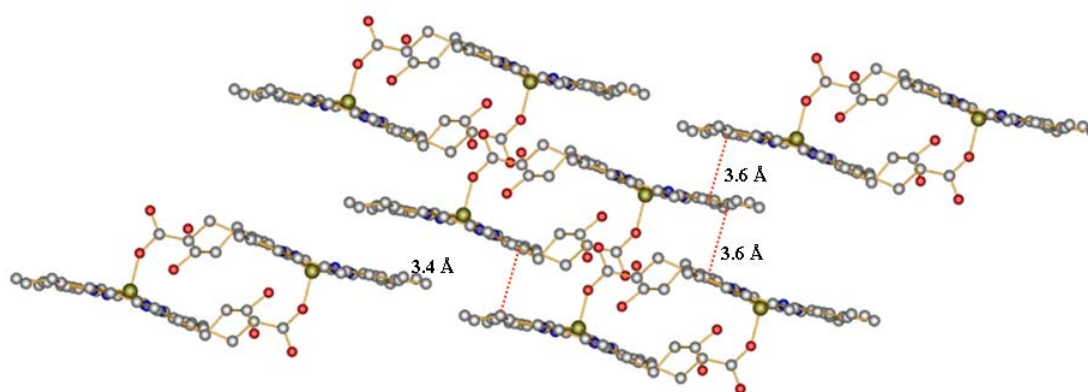
Figure 3.10 Closest porphyrin plane to porphyrin plane contact distance for β-hematin molecules in the crystal structure. Projection diagram drawn by *DIAMOND* program using XETXUP from the CSD.

The mean plane separation for β-hematin was not given in the original publication. β-hematin does not show $\pi-\pi$ interaction between reciprocal porphyrin cores due to the intercore distance being more than 4 Å. However, the closest intermolecular distance between porphyrin planes of adjacent molecules is 3.4 Å (calculated by *DIAMOND*, Crystal Impact, 2006) as shown in Figure 3.10. Therefore, there is a strong $\pi-\pi$ interaction in β-hematin which could be another contributing factor to explain the strong enhancement of the vibrational mode band ν_4 when using near-IR excitation lasers.

3.4 Conclusions

One additional parameter to be considered in β-hematin are the hydrogen bonds, which link together each dimer which facilitates the strong enhancement of vibrational mode ν_4. The results confirm that β-hematin is linked together by hydrogen bonds to form a chain (Pagola, Stephens, Bohle, Kosar, and Madsen, 2000), and also supports the hypothesis that there are intermolecular excitonic interactions occurring between porphyrin units (Wood, Langford, Cooke, Lim, Glenister, Duriska, Unthank, and McNaughton, 2004). The relative intensity of the vibrational mode ν_4 may be an indicator of the strength of $\pi-\pi$ interactions (Webster, Tilley, Deed, McNaughton, and Wood, 2008) and may be an indicator of the strength of hydrogen bond interactions. The extraordinary ν_4 band enhancement of β-hematin when exciting with near-infrared excitation wavelengths can be explained in terms of the supramolecular interactions between porphyrin plane to porphyrin plane and hydrogen bond linkage.

3.5 References

Bohle, D. S., Kosar, A. D., Stephens, P. W. (2002). Phase homogeneity and crystal morphology of the malaria pigment β-hematin. **Acta Cryst. D** 58(10−1): 1752−1756.

Burke, J. M., Kincaid, J. R., Spiro, T. G. (1978). Resonance Raman spectra and vibrational modes of iron(III) tetraphenylporphine μ-oxo dimer. Evidence for phenyl interaction and lack of dimer spitting. **J. Am. Chem. Soc.** 100(19): 6077−6083.

Byrappa, K, Yoshimaru, M. (2001). **Handbook of hydrothermal technology**: A technology for crystal growth and materials processing. William Andrew Publishing, LLC, U.S.A. 198.

Crystal Impact. (2006). *DIAMOND*. version 3.1. Crystal Impact GbR. Bonn, Germany.

Egan, T. J., Ross, D. C., Adams, P. A. (1994). Quinoline anti-malarial drugs inhibit spontaneous formation of β-hematin (malaria pigment). **FEBS Letters** 352(1): 54−57.

Egan, T. J., Hempelmann, E., Mavuso, W. W. (1999). Characterisation of synthetic β-haematin and effects of the antimalarial drugs quinidine, halofantrine, desbutylhalofantrine and mefloquine on its formation. **J. Inorg. Chem.** 73(1−2): 101−107.

Egan, T. J. (2008). Recent advances in understanding the mechanism of hemozoin (malaria pigment) formation. **J. Inor. Bio.** 102(5−6): 1288−1299.

Fitch, C. D., Kanjananggulpan, P. (1987). The state of ferriprotoporphyrin IX in malaria pigment. **J. Bio. Chem.** 262(32): 15552–15555.

Frosch, T., Koncarevic, S., Zedler, L., Schmitt, M., Schenzel, K., Becker, K., Popp, J. (2007). In *Situ* location and structural analysis of the malaria pigment hemozoin. **J. Phys. Chem. B** 111(39): 11047–11056.

Kitagawa, T., Ozaki, Y. (1987). **Struct. Bonding** 64: 73–114.

Pagola, S., Stephens, P. W., Bohle, D. S., Kosar, A. D., Madsen, S. K. (2000). The structure of malaria pigment β-hematin. **Nature** 404(6775): 307–310.

Puntharod, R., Haller, K. J., McNaughton, D., Wood, B. R. (2008). β-haematin and haematin by Raman and FTIR spectroscopy, Proceeding, 34th Congress on Science and Technology of Thailand, Bangkok, Thailand.

Slater, A. F. G., Swiggard, W. J., Orton, B. R. (1991). An iron-carboxylate bond links the heme units of malaria pigment. **Proc. Natl. Acad. Sci. USA** 88(2): 325–329.

Solomonov, I., Osipova, M., Feldman, Y., Baehtz, C., Kristian, K., Robinson, I. K., Webster, G. T., McNaughton, D., Wood, B. R., Weissbuch, I., Leiserowitz, L. (2007). Crystal nucleation, growth, and morphology of the synthetic malaria pigment β-hematin and the effect thereon by quinoline additives: the malaria pigments as a target of various antimalarial drugs. **J. Am. Chem. Soc.** 129(9): 2615–2627.

Spaulding, L. D., Chang, C. C., Yu, N., Felton, R. H. (1975). Resonance Raman spectra of metalloporphyrins. A structure probe of metal displacement. **J. Am. Chem. Soc.** 97(9): 2517–2525.

Spiro, T. G., Strekas, T. C. (1974). Resonance Raman spectra of heme proteins. Effects of oxidation and spin state. **J. Am. Chem. Soc.** 96(2): 338−345.

Spiro, T. G., Li, X-Y. (1988). **In Biological Applications of Raman Spectroscopy**; Spiro, T. G., Ed., Vol. 3, John Wiley & Sons, pp. 1−38.

Trivedi, V., Chand, P., Maulik, P. R., Bandyopadhyay, U. (2005). Mechanism of horseradish peroxidase-catalyzed heme oxidation and polymerization (β-hematin formation). **Biochem. et Biophy. Acta** 1723(1−3): 221−228.

Walczak, M., Lawniczak-Jablonska, K., Sienkiewicz, A., Demchenko, I. N., Piskorska, E., Chatain, G., Bohle, D. S. (2005). Local environment of iron in malaria pigment and its substitute β-hematin. **Nucl. Instr. and Meth. in Phys. Res. B** 238: 32−38.

Webster, G. T., Tilley, L., Deed, S., McNaughton, D., Wood, B. R. (2008). Resonance Raman spectroscopy can detect structural changes in haemozoin (malaria pigment) following incubation with chloroquine in infected erythrocytes. **FEBS Letters** 582(7): 1087−1092.

Wood, B. R., Langford, S. J., Cooke, B. M., Glenister, F. K., Lim J., McNaughton, D. (2003). Raman imaging of hemozoin within the food vacuole of *Plasmodium falciparum* trophozoites. **FEBS Letters** 554(3): 247−252.

Wood, B. R., Langford, S. J., Cooke, B. M., Lim, J., Glenister, F. K., Duriska, M., Unthank, J. K., McNaughton, D. (2004). Resonance Raman spectroscopy reveals new insight into the electronic structure of β-hematin and malaria pigment. **J. Am. Chem. Soc.** 126(30): 9233−9239.

CHAPTER IV

SUPRAMOLECULAR INERACTIONS PLAY AN INTEGRAL ROLE IN THE NEAR-INFRARED RAMAN EXCITONIC ENHANCEMENT OBSERVED IN MALARIA PIGMENT AND OTHER RELATED HEME AGGREGATES

4.1 Introduction

Hemozoin (malaria pigment) is a virtually insoluble byproduct produced from the catabolism of hemoglobin by the malaria parasite *Plasmodium falciparum* and other species (Ridley, 2002; Brown, 1911; Oliveira, Silva, Dansa-Petretski, de Souza, Lins, Braga, Masuda, and Oliveira, 1999). The compound is spectroscopically identical to *β*-hematin, which was found to be a heme dimer linked via reciprocal carboxylate groups with the dimers in turn linked together into a supramolecular hydrogen bonded array (Pagola, Stephens, Bohle, Kosar, and Madsen, 2000). The interest in hemozoin stems from the fact that quinoline based antimalarials are thought to bind to hemozoin, therefore preventing its formation or capping crystal growth, which results in the build up of toxic free heme, which can kill the parasite (Solomonov, Osipova, Feldman, Baehtz, Kristian, Robinson, Webster, McNaughton, Wood, Weissbuch, and Leiserowitz, 2007; Francis, Sullivan, and Goldberg, 1997;

Bohle, Conklin, Cox, Madsen, Paulson, Stephens, and Yee, 1994). Consequently, knowledge on the electronic, vibronic, and molecular structure of hemozoin could lead to the development of new antimalarials that target and block hemozoin formation. In pursuit of new approaches to examine hemozoin drug interactions and gain more insight into the structure of this important compound we have been utilizing near-infrared (IR) resonance Raman (RR) spectroscopy (Webster, Tilley, Deed, McNaughton, and Wood, 2008; Solomonov, Osipova, Feldman, Baehtz, Kristian, Robinson, Webster, McNaughton, Wood, Weissbuch, and Leiserowitz, 2007; Wood, Langford, Cooke, Lim, Glenister, Duriska, Unthank, and McNaughton, 2004).

RR spectroscopy has long been used to provide structural information on porphyrin moieties including metalloporphyrins and in particular iron porphyrins that serve as prosthetic groups for heme proteins (Spiro, 1988). Isotopic substitution studies and theoretical calculations have led to the assignment of many bands in the RR spectra of metalloporphyrins and in particular hemes (Abe, Kitagawa, and Kyogoku, 1978; Hu, Smith, and Spiro, 1996). Early RR studies reported that specific vibrational modes are sensitive to both the oxidation state and coordination number of the central metal ion (Spiro and Strekas, 1974; Yamamoto and Palmer, 1973). One band designated ν_4, assigned to the totally symmetric C_α–N pyrrole breathing mode (Abe, Kitagawa, and Kyogoku, 1978), appeared particularly sensitive to oxidation state, shifting in position from ~1370–1375 cm^{-1} in ferric hemes to ~1355 cm^{-1} in ferrous hemes as a result of increased back-donation of electron density from Fe d_π (d_{xz}, d_{yz}) to porphyrin $\pi*$ molecular orbitals (Spiro, 1974; Yamamoto and Palmer, 1973). This band was found generally enhanced in RR spectra of hemoglobin

solutions when using excitation wavelengths in resonance with the Soret band at ~400 nm and diminished when exciting in the vicinity of the Q (0,0) and Q (0,1) bands at ~540 and 575 nm, respectively (Strekas, Packer, and Spiro, 1973; Strekas and Spiro, 1973). The enhancement can be explained through the classical *A*- and *B*-type scattering mechanisms based on the sum-over-states approach to light dispersion derived by Kramers and Heisenberg (1925) and Dirac (1927) from second-order time dependent perturbation theory.

In type *A* scattering or Franck–Condon scattering only totally symmetric modes are enhanced because these are ineffective in mixing the electronic states. The intensity of a particular band is mainly dependent on the square of the transition dipole moment and more importantly on the overlap wavefunction integrals between the initial, intermediate, and final vibrational states summed over all the vibrational states (Equation 1). The enhancement of totally symmetric modes in heme solutions are commonly seen when exciting into the 400–500 nm Soret band region where there is little electronic configuration interaction occurring. Type *B* scattering involves a vibronic coupling mechanism whereby due to strong electronic configuration interaction between neighboring electronic states non-totally symmetric modes can become enhanced. The intensity of a band is dependent on the derivative of the normal coordinate with respect to the transition dipole but more importantly on how the normal coordinate, usually a low frequency non-totally symmetric mode, can couple the exited electronic states to give rise to the greatest wavefunction overlap between the initial, intermediate, and final states summed over all the vibrational states (Equation 2). Type *B* scattering explains the enhancement of non-totally

symmetric modes observed when exciting hemes with excitation wavelengths between 500–600 nm.

$$A = (\mu_e)^2 \frac{1}{\hbar} \sum_v \frac{\langle j|v\rangle\langle v|i\rangle}{\Delta\nu_v + i\Gamma_v}, \tag{1}$$

$$B = \mu_e \left(\frac{\partial\mu_e}{\partial Q}\right) \frac{1}{\hbar} \sum_v \frac{\langle j|Q|v\rangle\langle v|i\rangle + \langle j|v\rangle\langle v|Q|i\rangle}{\Delta\nu_v + i\Gamma_v} \tag{2}$$

where $|i\rangle$ and $|j\rangle$ are the initial and final vibrational wave functions of the ground electronic state, Q represents the normal coordinate operator, $|v\rangle$ represents the intermediate vibrational wave function in the resonant excited state, $\Delta\nu_v$ is the difference between the frequency of laser excitation wavelength and the frequency of the vibration in the excited state v, Γ_v is the half-width of the vibrational wave function for the excited state and represents the lifetime of the excited state, and $\hbar$ is $h/2\pi$ (h, Plank constant) (Spiro, 1988).

Recent RR studies of hemozoin demonstrated that the compound produced dramatic enhancement of the totally symmetric mode (ν_4) when irradiated with near-IR excitation wavelengths (782 and 830 nm) well away form the Soret and Q bands (Wood, Langford, Cooke, Glenister, Lim, and McNaughton, 2003; Wood, Langford, Cooke, Lim, Glenister, Duriska, Unthank, and McNaughton, 2004). It was postulated that the enhancement was attributable to excitonic interactions occurring throughout the supramolecular array (Wood, Langford, Cooke, Lim, Glenister, Duriska, Unthank, and McNaughton, 2004). To understand the mechanism of this excitonic

enhancement we investigated a number of structurally related high-spin ferric hemes with RR spectroscopy and correlated these results with X-ray crystallographic structural results.

RR spectra of model heme complexes including iron tetraphenylporphyrin Fe(TPP) and iron octaethylporphyrin Fe(OEP) derivatives in both monomeric and dimeric forms have been extensively studied (See Table 1.1). Furthermore, the crystal structures of Fe(TPP)Cl (Hoard, Cohen, and Glick, 1967; Scheidt and Finnegan, 1989), [Fe(TPP)]$_2$O (Hoffman, Collins, Day, Fleischer, Srivastava, and Hoard, 1972; Swepton and Ibers, 1985), Fe(OEP)Cl (Senge, 2005), and [Fe(OEP)]$_2$O (Cheng, Hobbs, Debrunner, Erlebacher, Shelnutt, and Scheidt, 1995) have been analyzed for supramolecular interactions. The stereochemistry of the dimers [Fe(TPP)]$_2$O, [Fe(OEP)]$_2$O, and [Fe(PPIX)]$_2$ (β-hematin) are similar, each consisting of a high-spin five-coordinate Fe(III) displaced above the mean plane of the porphyrin towards the axially coordinated O atom. Consequently, these structures serve as excellent model complexes to study the stereochemistry of hemozoin and provide excellent models to investigate the Raman "excitonic" enhancement mechanism previously reported for malaria pigment and its synthetic analogue β-hematin at near-IR excitation wavelengths (Wood, Langford, Cooke, Glenister, Lim, and McNaughton, 2003; Wood, Langford, Cooke, Lim, Glenister, Duriska, Unthank, and McNaughton, 2004).

In this study we compare excitation profiles for Raman bands of crystalline monomeric Fe(TPP)Cl and Fe(OEP)Cl and of the corresponding dimeric [Fe(TPP)]$_2$O and [Fe(OEP)]$_2$O. Only one of the four compounds investigated namely [Fe(OEP)]$_2$O does not show the enhancement of the totally symmetric modes at near-IR excitation. Based on X-ray crystallographic results it is hypothesized that the enhancement could

be in part attributed to noncovalent supramolecular interactions. Since the axial ligands and the peripheral substitution groups are different for monomers and dimers of Fe(TPP) and Fe(OEP), their intermolecular interactions are also different which in turn affects the excitonic interactions throughout the aggregates. To date, there has been no report on the enhancement of Raman bands of these compounds at near-IR excitation.

Table 4.1 List of Literature for Raman Results of Fe(TPP) and Fe(OEP).

Iron(III) porphyrin	Excitation laser wavelength (nm)	Solvent/Conditions	References
Fe(OEP)Cl	458–514	CH_2Cl_2	Spaulding, Chang, Yu, and Felton, 1975
Fe(TPP)Cl, [Fe(TPP)]$_2$O	568	Benzene, piperidine	Adar and Srivastava, 1976
Fe(OEP)Cl	488	THF	Kitagawa, Abe and Kyogoku, 1976
Fe(TPP)Cl, [Fe(TPP)]$_2$O	458–616	CH_2Cl_2, THF, CS_2, benzene	Burke, Kincaid and Spiro, 1978 Burke, Kincaid, Peters, Gange, Collman, and Spiro, 1978
[Fe(OEP)]$_2$O	407, 568	CS_2	Hofmann and Bocian, 1984
Fe(TPP)Cl, [Fe(TPP)]$_2$O	458, 567	Solid state	Kowalewski, Merlin, Brémard, and Moreau, 1988
Fe(OEP)Cl	442	MeOH/CH_2Cl_2 (1:1)	Filder, Ogura, Sato, Aoyagi, and Kitagawa, 1991
[Fe(TPP)]$_2$O	458	CS_2, $CHCl_3$	Brémard, Kowalewski, Merlin, and Moreau, 1992
Fe(TPP)Cl	407, 442	CH_2Cl_2	Shantha, Thanga and Verma, 1998

This study provides new insight into the mechanism of Raman excitonic enhancement observed at near-IR excitation wavelengths in heme compounds thus providing additional insight into the supramolecular structure of malaria pigment. The

combination of RR spectroscopy and X-ray crystallography indicates a correlation between the presence of inter-heme interactions including C$-$H$\cdots$X hydrogen bonding (where X (π, chloro) is an electron donating entity) and the enhancement of ν_4 in heme complexes at near-IR excitation. Consequently, the enhancement of ν_4 at near-IR excitation can be used as an indicator of intermolecular interactions in heme complexes especially in β-hematin. Such information could be used to monitor the effects of anti-malarial drugs designed to inhibit hemozoin formation in *Plasmodium falciparum* infected erythrocytes. Moreover, the results underpin the importance of noncovalent interactions in excitonic energy transfer processes in heme aggregates, which could have enormous implications in the development of heme based near-IR photon transfer devices.

4.2 Experiment

Compounds. Fe(TPP)Cl and Fe(OEP)Cl were purchased from Sigma Aldrich. [Fe(TPP)]$_2$O and [Fe(OEP)]$_2$O were prepared based on the method of Cheng, Hobbs, Debrunner, Erlebacher, Shelnutt, and Scheidt (1995).

Electronic Absorbance Spectra. Electronic absorption spectra of samples were recorded using a J&M MSP800 UV$-$visible spectrometer equipped with a Leica DM4000M microscope and an ×40 quartz UV$-$visible objective with a 7×7 µm aperture size in the spectral range 940$-$500 nm as 20 accumulations using a 1.2 sec integration time per accumulation.

Attenuated Total Reflection Fourier Transforms Infrared Spectroscopy (ATR/FTIR). ATR/FTIR spectra of samples were recorded with a Varian 600-UMA

FTIR microscope equipped with an HgCdTe detector and coupled to a Varian 7000 FTIR spectrometer. Spectra were recorded in reflection mode on Kevley™ "low e" IR reflective slide substrates (6 cm^{-1} resolution, 128 co-added scans, apodized using a Blackman Harris 4 term function and zero filled by a factor of 2).

Resonance Raman (RR) Spectroscopy. RR spectra of products were recorded on a Renishaw system 2000 spectrometer using a 413 nm (or 514 nm) excitation line (Spectra Physics Ar$^+$ Stabilite 2017 laser system), a 633 nm excitation line generated by Coherent 45 mW helium−neon laser, or a 782 nm (or 830 nm) excitation line generated by diode lasers (Renishaw RM2000) in a back scattering geometry. The laser power on the sample was approximately 39, 130, 160, 500, and 600 μW for the excitation wavelengths 413, 514, 633, 782, and 830 nm, respectively. The system was equipped with an Olympus optical microscope and a Zeiss ×60 water immersion objective to enable spectral acquisition in water to prevent the thermal degradation of the solid samples. All spectra presented have been smoothed and normalized after interactive baseline-correction using the concave rubber band algorithm in the OPUS software.

Crystallographic Calculations. Supramolecular interaction contact distances and angles were calculated with *ORTEP-III* (Burnett and Johnson, 1996) reported with the conventional D−H···A notation or with D−H···(A−A') notation where the acceptor position is the midpoint of the A−A' bond of the relevant aromatic system. Coordinates for Fe(TPP)Cl (Scheidt and Finnegan, 1989), [Fe(TPP)]$_2$O (Swepston and Ibers, 1985), Fe(OEP)Cl (Senge, 2005), triclinic [Fe(OEP)]$_2$O (Cheng, Hobbs, Debrunner, Erlebacher, Shelnutt, and Scheidt, 1995), and monoclinic (Cheng, Hobbs, Debrunner, Erlebacher, Shelnutt, and Scheidt, 1995) were obtained from the

Cambridge Structural Database (Cambridge Structural Database). Refcodes: KANYUT, PPORFE01, TOYRUU, YIKJOR, and YIKJOR01, respectively.

4.3 Results
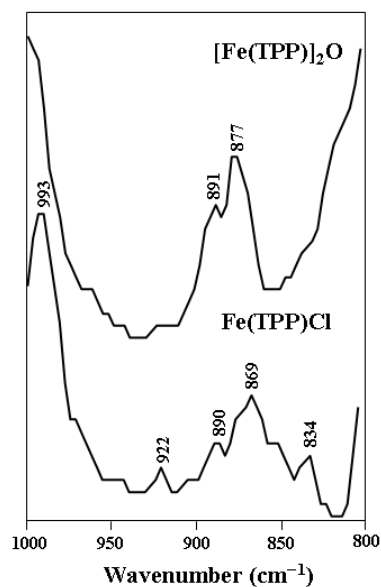
Figure 4.1 FTIR spectra of Fe(TPP)Cl and [Fe(TPP)]$_2$O.
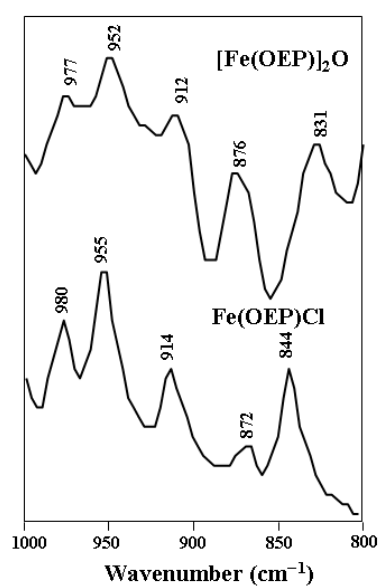
Figure 4.2 FTIR spectra of Fe(OEP)Cl and [Fe(OEP)]$_2$O.

FTIR Spectroscopy. Oxo-bridged dimers of transition metals including Fe(III) porphyrins have been characterized by ATR/FTIR spectroscopy of microcrystalline samples. The IR absorption band in the region 800–900 cm^{-1} has been used as evidence of the μ-oxo-bridged dimer for several transition metal complexes (Sadasivan, Eberspaecher, Fuchsman, and Caugey, 1969). The FTIR spectra of dimers presented in Figures 4.1 and 4.2 exhibit the asymmetric stretching vibration of Fe–O–Fe at 877 and 876 cm^{-1} for [Fe(TPP)]$_2$O (Fleisher and Srivastava, 1969) and [Fe(OEP)]$_2$O (Hofmann and Bocian, 1984), respectively which confirm the formation of the μ-oxo-dimer complexes.

Solid State Resonance Raman Spectroscopy. Figures 4.3 and 4.4 compare the solid state RR spectra of monomers and dimers of Fe(TPP) and Fe(OEP) at different excitation wavelengths while Table A1 and A2 (Appendix A) give a complete listing of the observed bands along with relative enhancement at each excitation wavelength. It should be noted that all spectra were min(0)–max(10) normalized to facilitate the comparison. The vibrational mode notation is based on that proposed by Abe Kitagawa, and Kyogoku (1978) for Ni(OEP) with some amendments to the assignments made by Rush, Kozlowski, Piffat, Kumble, and Zgierski (2000) from their studies on Ni(TPP). Although the axial ligands lower the actual symmetry, the idealized D_{4h} symmetry selection rules are followed closely enough to maintain the assignment scheme and are adopted by convention.

When exciting into the Soret band using a 413 nm laser, all heme derivatives investigated exhibit dramatic enhancement of the totally symmetric modes including ν_2, ν_3, and ν_4 as expected when the A-term RR scattering mechanism is the dominant

term. Relative enhancement of other A_{1g} modes including ν_1 and ν_8 (in TPPs), and ν_6 (in [Fe(OEP)]$_2$O) are also observed.

When exciting at 514 nm, in TPPs, totally symmetric modes ν_2, ν_4, ν_6 (in dimer), and ν_8 (in monomer) again dominate the spectra although the B_{1g} mode ν_{11} is also enhanced. However, in OEPs non-totally symmetric modes ν_{10}, ν_{11}, ν_{19}, ν_{21}, and ν_{29} dominate the spectra and the A_{1g} mode ν_4 is also enhanced.

When exciting with a 633 nm laser line all types of modes are observed in TPPs including polarized (ν_2, ν_4, ν_1, ν_8), depolarized (ν_{11}, ν_{30}), and inverse polarized modes (ν_{19}, ν_{20}). However, in OEPs, the spectra are dominated by B_{1g} (ν_{10}, ν_{11}, ν_{13}, ν_{15}) and A_{2g} (ν_{19}, ν_{21}) modes.

Finally, when using near-IR excitation wavelengths (782 and 830 nm), the spectra of TPPs are still dominated by totally symmetric modes ν_2, ν_4, ν_1, ν_6, and ν_8. However, in the spectra of Fe(OEP)Cl both B_{1g} (ν_{11}, ν_{13}) and A_{1g} (ν_2, ν_4) modes are dramatically enhanced while the spectra of [Fe(OEP)]$_2$O are dominated by B_{1g} modes ν_{10}, ν_{11}, and ν_{13} and the A_{1g} mode ν_4 has virtually disappeared. Notably, the pattern of the bands in the spectrum of [Fe(OEP)]$_2$O resembles the FT-Raman spectra (at 1064 nm excitation) of heme derivatives indicating a lack of any type of RR enhancement (Ozaki, Mizuno, Sato, Kawaguchi, and Muraishi, 1992).

The band at ~366 cm^{-1} observed in the spectra of [(FeTPP)]$_2$O is assigned to the Fe−O−Fe symmetric stretch, whilst the band at ~390 cm^{-1} is assigned to an in-plane deformation mode that incorporates contributions from the Fe−N stretching vibration.[21(d)] The relative intensity of these bands radically changes depending on the excitation wavelength applied. At 413, 782, and 830 nm the intensity of the band at

~390 cm^{-1} is much greater than the 366 cm^{-1} band. The opposite is observed when exciting with 514 and 633 nm where the 366 cm^{-1} band is much more intense than the 390 cm^{-1} band. Moreover, the axial ligand vibrations ν(Fe–Cl) and ν_{sym}(Fe–O–Fe) are enhanced at 633 nm and near-IR excitation except for [Fe(OEP)]$_2$O in which the ν_{sym}(Fe–O–Fe) band is virtually absent at all excitation wavelengths studied.
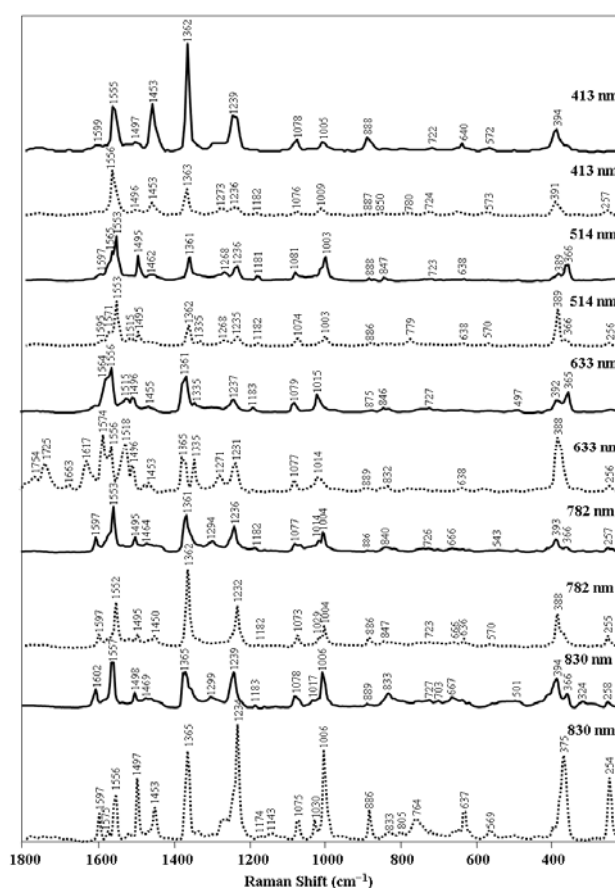
Figure 4.3 RR spectra of Fe(TPP)Cl and [Fe(TPP)]$_2$O. The solid lines correspond to the μ-oxo dimer complex and the dashed lines correspond to the chloro monomer.
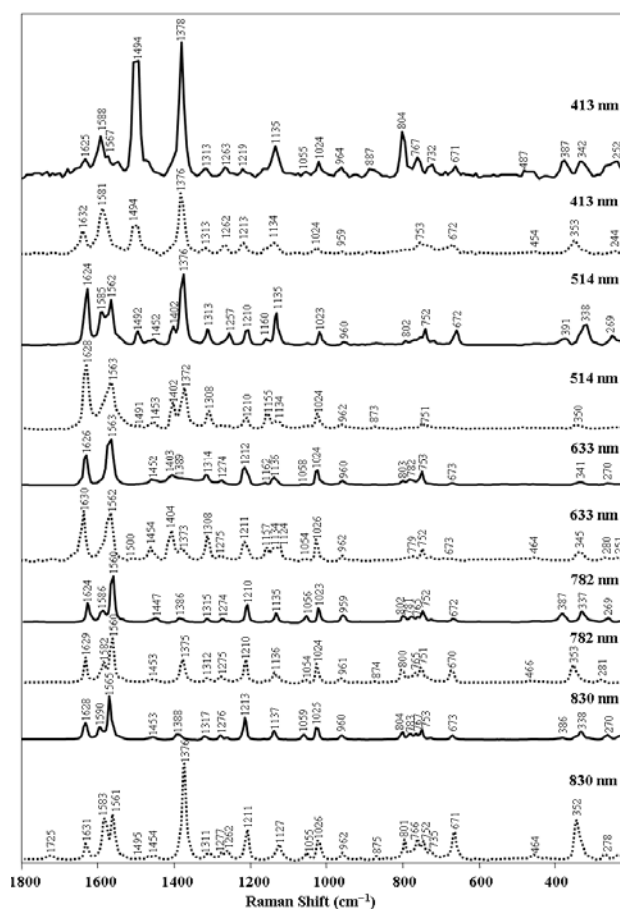
Figure 4.4 RR spectra of Fe(OEP)Cl and [Fe(OEP)]$_2$O. The solid lines correspond to the μ-oxo dimer complex and the dashed lines correspond to the monomer.

Phenyl internal modes of the TPP derivatives are observed enhanced for all wavelengths investigated. The enhancement of these modes is explained through kinematic mixing of the phenyl internal modes with porphyrin skeletal modes (Kincaid, 2000). Based on isotopic substitution and polarization studies Burke and co-workers (Burke, Kincaid, and Spiro, 1978; Burke, Kincaid, Peters, Gagne, Collman, and Spiro, 1978) assigned bands appearing at 1599, 1030, and 886 cm^{-1} in [Fe(TPP)]$_2$O solutions to the phenyl modes. These bands are also observed in the

solid phase spectra, albeit small and slightly shifted when using visible excitation wavelengths. Interestingly, these bands become more pronounced in the solid phase when using near-IR excitation wavelengths. The fact that these modes are polarized like the totally symmetric A_{1g} porphyrin modes, which are also enhanced when using near-IR excitation wavelengths, indicates there is another mechanism at work contributing to their enhancement.

Solid State UV-visible Spectroscopy. The UV−visible absorption spectra of TPP and OEP derivatives are depicted in Figure 4.5. The "normal" absorption spectrum of metalloporphyrin contains a sharp intense Soret band at approximately 400 nm along with two smaller bands in the visible region (500−600 nm). However, different types of absorption spectra are usually observed depending on the characteristics of the central metal ion and the substituent groups. The perturbation of the "normal" spectrum is partly caused by intramolecular charge transfer from the porphyrin orbitals to the metal d_π orbitals (Zerner, Gouterman, and Kobayashi, 1966), which is usually connected with an unsymmetrical axial coordination of the ligand(s) and/or a nonplanar coordination of the metal ion to the porphyrin. The high-spin five coordinate ferric porphyrins generally display several overlapping bands in the visible region. Assignment of these complex spectra has been controversial (Strekas and Spiro, 1973; Burke, Kincaid, and Spiro, 1978; Burke, Kincaid, Peters, Gagne, Collman, and Spiro, 1978; Paulat and Lehnert, 2008). However, the major electronic bands observed in these compounds are still from $\pi \rightarrow \pi^*$ transitions occurring at approximately 400 nm (Soret) and between 500 and 600 nm (Q bands). Other transitions include various charge-transfer transitions from porphyrin to iron or between iron and axial ligand.

As shown in Figure 4.5, the spectral profiles have remarkable differences between monomers and dimers although RR enhancement patterns are very similar (except at near-IR excitation of OEPs). Another factor that influences the absorption spectrum of metalloporphyrins is the intermolecular interactions and excitonic effects in aggregates. Most of the previous studies regarding the effects of aggregation on absorption spectra of porphyrins are focused on Soret and Q band regions. Since the exciton interaction depends on the square of the transition moment, generally the excitonic effects (including splitting of bands) in the visible region are substantially less than those in the near-UV (Selensky, Holten, Windor, Paine, and Dolphin, 1981). However, the discovery of "excitonic" enhancement of A_{1g} modes at near-IR excitation in our lab (Wood, Langford, Cooke, Lim, Glenister, Duriska, Unthank, and McNaughton, 2004) indicates that excitonic transition bands (albeit weak) in near-IR region can have substantial effects on the pattern of RR spectra. Since there is no vibronic coupling (and enhanced non-totally symmetric modes) in this region, the relative enhancement of A_{1g} modes via resonance with a small excitonic transition can make totally symmetric modes dominate the spectrum. An inspection of the near-IR region of the UV−visible spectra presented in Figure 4.5 shows there is possibly a very broad weak absorption band between 800−900 nm and another between 700−750 nm.

Recently Paulat (2008) assigned in detail the magnetic circular dichroism (MCD) and UV−visible bands of Fe(TPP)Cl using TD-DFT. However, the nature of two weak bands, 863 nm (MCD, broad) and 738 nm (UV−visible) remained unclear. Using a higher basis set (TZVP) we repeated the calculations and could assign the broad band at 875 nm (in our spectrum of Fe(TPP)Cl) to $a_{2u}(\pi) \rightarrow d_\pi$ transition (Table

A3, Appendix A). Similar calculations on OEPs and [Fe(TPP)]$_2$O are under way. We believe there should be similar electronic transitions in the near-IR region absorption spectra of [Fe(TPP)]$_2$O and Fe(OEP)Cl, which show the RR enhancement of A$_{1g}$ modes at near-IR excitation. There is a similar broad band (at 867 nm) in the absorption spectrum of hemin which is pronounced in β-hematin and has already been evoked to explain RR enhancement of A$_{1g}$ modes at near-IR excited spectra of these compounds (Wood, Langford, Cooke, Lim, Glenister, Duriska, Unthank, and McNaughton, 2004).
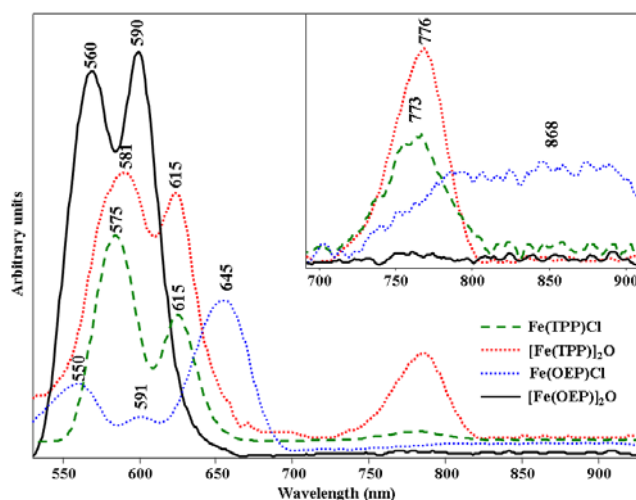
Figure 4.5 UV-visible absorbance spectra of crystalline heme derivatives.

Solution Resonance Raman Spectroscopy. It is important to note that we were unable to obtain solution phase RR spectra of Fe(OEP)Cl and Fe(TPP)Cl along with their related μ-oxo dimers when using near-IR excitation wavelengths even at high concentrations (>10 mM) and relatively high laser power (20 mW). The solution phase spectra at these excitation wavelengths show a broad featureless baseline with no evidence of any bands. However, a number of studies have reported solution phase

RR spectra of Fe(TPP) and Fe(OEP) monomers and μ-oxo dimers using visible excitation wavelengths (See Table 4.1). In a very recent study we investigated the RR spectra of hematin and hemin at different concentrations using 413 and 514 nm excitation. As the concentration of hematin/hemin increases there is an increased probability of supramolecular interactions between iron(III) Fe(PPIX) units occurring. The iron(III) Fe(PPIX) concentration reaches a saturation point in solution and excitonic coupling reaches a maximum causing the enhancement profile to plateau when applying 514 nm excitation. In contrast, when using 413 nm excitation there were no changes in band intensity with increased concentration showing that excitonic coupling through supramolecular interactions for aggregated solutions is wavelength dependent (Webster, McNaughton, and Wood, 2009).

X-ray Crystallography.

(a) General Comments. *ORTEP-III* (Burnett and Johnson, 1996) illustrations of monomeric and dimeric [Fe(TPP)] and [Fe(OEP)] molecules, as they exist in crystal structures, are shown in Figures A1−A5 (Appendix A). In the previous studies, the structural parameters of interest were primarily the conformational characteristics of the iron atom and porphyrin core, including the bond lengths of Fe−N and Fe−axial ligand as well as the displacement of iron atom out of the porphyrin plane. From the X-ray crystallographic results, these features are similar, all showing five-coordinate square-pyramidal geometry in the high-spin ferric state. Table 4.2 summarizes the average Fe−N bond distances, Fe(III) displacements from the porphyrin plane, and shortest porphyrin-porphyrin contact distances.

Table 4.2 Molecular Parameters Including Intermolecular Distance and Interactions for Heme Compounds in this Study.

Heme derivatives	O.S of Fe	Spin state of Fe	C.N of Fe	Axial ligand	d[Fe–N] (Å)	Displacement of Fe (Å)	Intermolecular distance between porphyrin ring	Type of interaction (*)	Enhancement of ν_4 band (C_α–N, ~1375 cm^{-1}) at near-IR excitation laser
Fe(TPP)Cl monomer $P2_1/n$, Z = 4 Scheidt *et al.* (1989)	3+	high spin	5	Cl	2.070(9)	0.57	4.5 (by *Diamond*)	C–H···Cl (3) C–H···$\pi_{pyrrole}$ (10) C–H···π_{phenyl} (1)	✓
[Fe(TPP)]$_2$O dimer $C2ca$, Z = 4 Hoffman *et al.* (1972)	3+	high spin	5	O μ-oxo	2.087(3)	0.54	~ 5.20	C–H···$\pi_{pyrrole}$ (18) C–H···π_{phenyl} (6)	✓
Fe(OEP)Cl monomer $P2_1/c$, Z = 4 Senge (2005)	3+	high spin	5	Cl	2.071(2)	0.49	4.02	C–H···Cl (4) C–H···$\pi_{pyrrole}$ (11)	✓
[Fe(OEP)]$_2$O dimer $P–1$, Z = 4 $P2_1/c$, Z = 4 Cheng *et al.* (1995)	3+	high spin	5	O μ-oxo	2.077(3) for triclinic 2.080(5) for monoclinic	0.50 for triclinic 0.54 for monoclinic	4.5 for triclinic 4.6 for monoclinic	C–H···$\pi_{pyrrole}$ (6)	✗
β-hematin dimer $P–1$, Z = 2 Pagola *et al.* (2000)	3+	high spin	5	O	2.061	0.47	3.4 (by *Diamond*)	C–H···O (17) (**) O–H···O (2) C–H···$\pi_{pyrrole}$ (24)	✓

(*) The numbers in parentheses refer to the number of calculated interactions based on d[H···A] ≤ 3.0 Å and d[D···A] ≤ 4.0 Å (except A = N; d[H···A] ≤ 3.2 Å). (**) The calculated interactions of β-hematin are only calculated d[D···A] ≤ 4.0 Å due to hydrogen atoms were not included in the original paper. See Tables A4–A9 (Appendix A) for full listings of the calculated H-bond parameters.

However, the fact that [Fe(OEP)]$_2$O does not exhibit the enhancement of electron density marker band ν_4 at near-IR excitation wavelengths reveals that there should be additional parameter(s) which influence the RR enhancement mechanisms. To further investigate the mechanism of enhancement of totally symmetric modes a detailed analysis of the crystal structures is required. We have considered the

supramolecular chemistry of TPP and OEP derivatives as a possible factor to explain the enhancement of totally symmetric modes (particularly at near-IR excitation wavelengths). Since the axial ligands and the peripheral substituent groups are different in monomers and dimers of Fe(TPP) and Fe(OEP), their intermolecular interactions may also be different which in turn could affect the excitonic interactions throughout the aggregates. In the following, the various intra- and inter-molecular interactions are considered and support the hypothesis that supramolecular interactions are one factor in explaining the enhancement of A_{1g} modes in TPPs and OEP monomer and the dramatic reduction of the same modes in the OEP dimer. The number of noncovalent intermolecular interactions for the heme compounds in this study are also included in Table 4.2.

(b) Distance between Porphyrin Planes. In the case of dimeric β-hematin, the closest intermolecular distance between porphyrin planes is 3.4 Å (*DIAMOND*, Crystal Impact, 2006 calculation; Figure A6, Appendix A). The average mean plane separations between two porphyrin rings for the Fe(TPP) and Fe(OEP) monomers and dimers are all greater than 4 Å (Table 4.2), indicating minimal π–π interactions between the two chromophores in these species. However, in the case of the triclinic Fe(OEP) dimer the geometric constraints of the nearly eclipsed porphyrin cores along with an Fe–O–Fe angle of 172° leads to porphyrin-porphyrin contact distances between the nonparallel cores as short as 3.8 Å.

(c) Delocalizes π System and Steric Interaction. The appearance of enhancement of Raman bands assignable to internal modes of the phenyl rings, in resonance with the porphyrin π–π* transition, demonstrates an interaction between the phenyl and porphyrin π systems previously attributed to intramolecular

delocalization between the porphyrin and phenyl π systems (Fuchsman, Smith, and Stein, 1977). However, since the phenyl rings are tilted with respect to the porphyrin ring (by angles from 53 to 83°), and there is a substantial barrier to rotation, reflecting the steric hindrance between the *ortho* hydrogen atoms of the phenyl groups and the adjacent pyrrole rings (Hoffman, Collins, Day, Fleischer, Srivastava, and Hoard, 1972), overlap between the phenyl and porphyrin π systems in the ground state has been questioned (Fuchsman, Smith, and Stein, 1977; Tsubuki, Srivastava, and Nai-Teng, 1982). It is also significant that the enhancement observed here is a *solid state* effect. NMR evidence for phenyl ring rotation in solution from five-coordinate *para*-substituted phenyl analogues finds an activation barrier of about 16 kcal mol^{-1} for chloro iron(III) analogues, and also facilitation of the averaging of nonequivalent phenyl ring *ortho* protons by addition of chloride ion (Eaton and Eaton, 1975), suggesting a dissociation mechanism is also operating to average the nonequivalent *ortho* hydrogen atoms. Furthermore, rotation of the phenyl rings in the solid state would be expected to destroy the crystal lattice, as occurs with as little as 35° rotation of axial pyridines in the perchlorate salt of $[Fe(OEP)(3\text{-}Clpy)_2]^+$ to achieve an $S = {}^3/_2$ (quantum-admixed intermediate-spin state) (Scheidt, Geiger, Hayes, and Laing, 1983) to $S = {}^1/_2$ (low spin state) (Scheidt, Geiger, and Haller, 1982) transition, where the transition is accompanied by fragmentation of the crystal.

In any case, the fact that the aliphatic substituents on Fe(OEP)Cl do not allow the possibility of extended delocalization and yet Fe(OEP)Cl exhibits enhancement of A_{1g} modes at near-IR excitation indicates there should be other factors that account for the RR enhancement of the ν_4 band. Further, the lack of enhancement in the solution phase RR spectra even at high concentrations for all heme derivatives

investigated here when using near-IR excitation wavelengths suggests that the enhancement is not due to an intramolecular mechanism. This provides supporting evidence that the band enhancement observed when applying near-IR excitation is a solid state phenomenon involving intermolecular interactions.

(d) Hydrogen Bonding. β-hematin shows the enhancement of A_{1g} modes at near-IR excitation wavelengths (Wood, Langford, Cooke, Lim, Glenister, Duriska, Unthank, and McNaughton, 2004). The interpretation of the high-resolution powder diffraction data indicates that β-hematin contains centrosymmetric dimers with reciprocal propionate linkages, and that the dimers are linked together by strong hydrogen bonds (Pagola, Stephens; Bohle, Kosar, and Madsen, 2000). TPPs exhibit hydrogen bond interactions including C–H···π (π system of phenyl and/or porphyrin rings) and C–H···Cl (in monomer) as shown in Figures 4.6 and 4.7. Both OEP derivatives also show hydrogen bond interactions between the porphyrin π systems and C–H of the methylene and methyl groups (Figure 4.8) and numerous C–H···Cl bonding interactions in the monomer (Figure 4.9). The total number of C–H···X intermolecular interactions (included in Table 4.2) for the Fe(OEP) monomer and both the Fe(TPP) monomer and dimer is much larger than for the Fe(OEP) dimer.
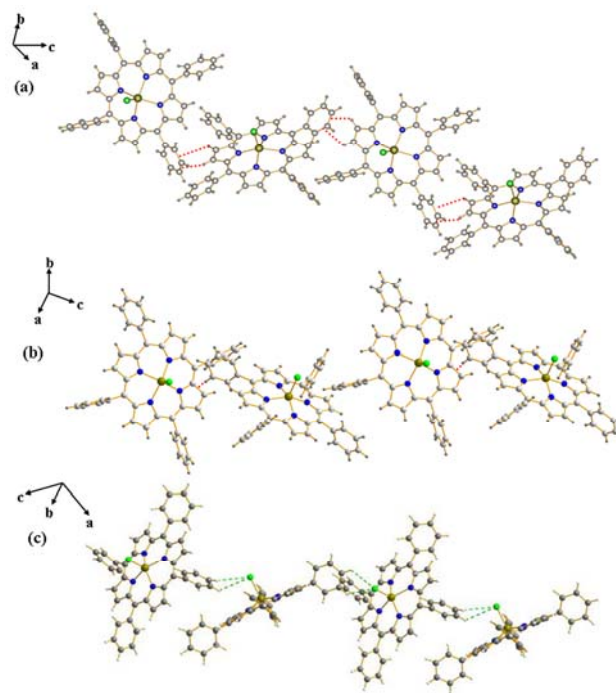
Figure 4.6 Nonbonded interaction of Fe(TPP)Cl showing (a) the C–H⋯π_{phenyl}, (b) C–H⋯$\pi_{pyrrole}$, and (c) C–H⋯Cl hydrogen bond interactions.
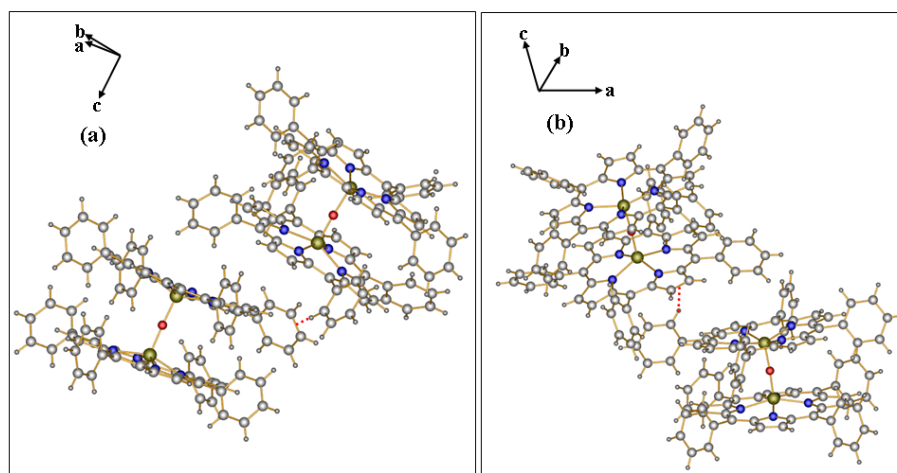
Figure 4.7 Nonbonded interaction of [Fe(TPP)]$_2$O showing (a) the C–H⋯π_{phenyl} and (b) C–H⋯$\pi_{pyrrole}$ hydrogen bond interactions.
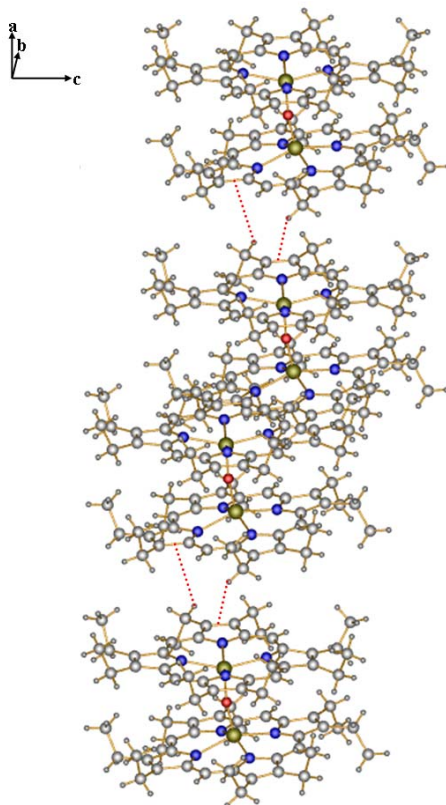
Figure 4.8 Nonbonded interaction of [Fe(OEP)]$_2$O showing C–H···$\pi_{pyrrole}$ hydrogen
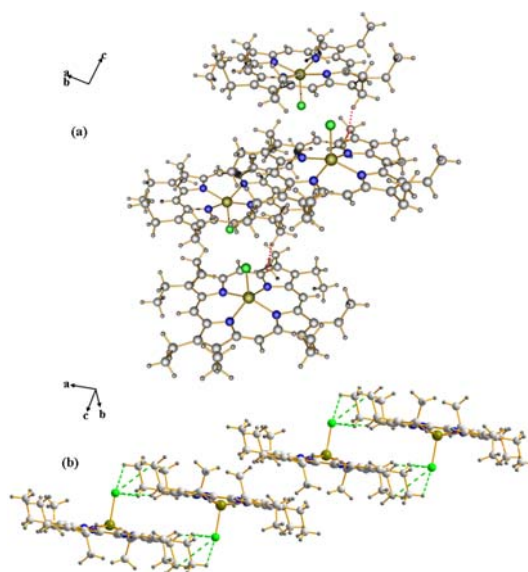
bond interactions.

Figure 4.9 Nonbonded interaction of Fe(OEP)Cl showing (a) C–H···$\pi_{pyrrole}$ and (b)

C–H···Cl hydrogen bond interactions.

4.4 Discussion

Detail investigation of the above results reveals that there are a few deviations from the excitation profiles expected for the intermolecular heme compounds based on conventional Type *A* and Type *B* resonance Raman enhancement mechanisms.

1. Exciting solid phase TPP derivatives with 514 nm in the Q band region is similar to solution phase spectra reported by Burke and co-workers for $[Fe(TPP)]O_2$ (Burke, Kincaid and Spiro, 1978; Burke, Kincaid, Peters, Gagne, Collman, and Spiro, 1978) which in turn shows a similar excitation profile to those reported by Shelnutt, Cheung, Change, Yu, and Felton (1977) for Cr(TPP)Cl. The spectra show enhancement of non-totally symmetric modes including A_{2g}, B_{1g} and to a lesser extent B_{2g} modes. This was interpreted in terms of strong vibronic coupling between the Q and B (Soret) states, superimposed on a small amount of Jahn-Teller activity (Shelnutt, Cheung, Change, Yu, and Felton, 1977). Exciting with laser wavelengths in the Q band region also resulted in the enhancement of totally symmetric A_{1g} modes including bands at 1362 and 390 cm^{-1}. Shelnutt and co-workers (Shelnutt, Cheung, Change, Yu, and Felton, 1977) observed similar enhancement profiles for Cr(TPP)Cl and interpreted them as "helping mode" behavior. In case of $[Fe(TPP)]O_2$ the band at ~1362 cm^{-1} helps the 390 and 363 cm^{-1} modes by virtue of its large origin shift in the Q state producing large Franck–Condon products involving scattering into the 390 and 363 cm^{-1} states via an intermediate state with one quantum of excitation in the 1359 cm^{-1} mode (Shelnutt, Cheung, Change, Yu, and Felton, 1977; Burke, Kincaid, and Spiro, 1978; Burke, Kincaid, Peters, Gagne, Collman, and Spiro, 1978). Through this mechanism both Type *A* and *B* term scattering can result as theorized by Warshel and Dauber (1977).

2. In general the Fe−O−Fe, Fe−N and Fe−Cl stretching modes are enhanced at 633 nm and near-IR excitation for TPPs and OEP monomer but not at 413 nm. The intensity of these modes might be expected to arise from resonance with a charge transfer transition ($Cl^- \rightarrow Fe^{3+}$ or $O^{2-} \rightarrow Fe^{3+}$). However, this seems too low an energy for a charge-transfer from oxide or halide to high-spin iron(III). Time-dependent density functional theory (TD-DFT) calculations do not show any charge-transfer from chloride to Fe ion in Fe(TPP)Cl at near-IR region (Table A3, Appendix A). Another argument is the effect of angle on the intensity of these modes. Theoretical models for μ-oxo complexes predict a potential minimum at an angle smaller than 150° but steric interaction which occurs between two porphyrin rings can increase the angle (Tsubakin, Srivastava and Nai-Teng, 1982). In $[Fe(TPP)]_2O$ the observed Fe–O–Fe angle is 174.5° (Hoffman, Collins, Day, Fleischer, Srivastava, and Hoard, 1972). An increase of angle could promote the overlap of iron d orbitals and oxygen 2p orbitals and thus decreases the energy of the μ-oxo $\rightarrow$ Fe(III) charge transfer transition (Kowalewski, Merlin, Bremard, and Moreau, 1988). However, the lack of RR enhancement of ν_{sym}(Fe–O–Fe) in $[Fe(OEP)]_2O$ (with Fe–O–Fe angle similar to that of TPP dimer) rules out the generality of this argument. Moreover, a correlation between motion of the nitrogen and iron atoms has been evoked as the mechanism to explain the coupling between the Fe–O–Fe stretching and the ν_4 breathing modes (Burke, Kincaid, and Spiro, 1978). Motion of the iron atom into the plane of the pyrrole nitrogen atoms is made easier if the nitrogen atoms simultaneously move outward. This provides a mechanism for coupling the Fe–O–Fe stretch with the ν_4 pyrrole-breathing mode. Our results corroborate this argument. Following the lack of enhancement of ν_4 at 633 and near-IR excited RR spectra of

[Fe(OEP)]$_2$O, the intensity of ν_{sym}(Fe–O–Fe) is near zero while the dramatically enhanced ν_4 breathing mode in TPPs and OEP monomer help the axial ligand stretching modes to be enhanced as well.

3. A striking observation, first observed in our lab for hemozoin and β-hematin (Wood, Langford, Cooke, Lim, Glenister, Duriska, Unthank, and McNaughton, 2004), is the dramatic enhancement of the totally symmetric RR modes at near-IR excitation of all heme species studied to date except for [Fe(OEP)]$_2$O. It was noted that when exciting with 782 and 830 nm lines a number of totally symmetric modes including ν_4 (1374 cm^{-1}), ν_2 (1572 cm^{-1}), and ν_7 (678 cm^{-1}) dramatically enhance relative to ν_{10} (1625 cm^{-1}). Such enhancement can only occur under an A-term mechanism. It was suggested that the dramatic A-type enhancement observed at near-IR excitation wavelengths well away from any of the major optical electronic transitions was the result of excitonic interactions occurring throughout the heme aggregate. A small broad electronic transition observed at ~867 nm during the acidification of Fe(PPIX)Cl (hemin) to β-hematin, was implicated in the mechanism of enhancement.

Similar enhancement of these modes was also observed for the monomeric precursors, hemin and Fe(PPIX)OH (hematin) but not as much as that observed in the dimer complex indicating less interaction between porphyrins in monomeric forms. Based on symmetry arguments and UV–visible spectroscopic monitoring of the acidification of hemin to β-hematin which shows a red shifting of the Soret, Q, and a band at ~867 nm, it was hypothesized that an excitonic mechanism is contributing to the observed enhancement (Wood, Langford, Cooke, Lim, Glenister, Duriska,

Unthank, and McNaughton, 2004). In this scenario, the symmetric electronic component of the near-IR photon couples the excited states of charge transfer transitions resulting in a superposition of states increasing the contributions to the Franck–Condon integrals.

To the best of our knowledge, there has been no other report in the literature about the enhancement of A_{1g} modes at near-IR excited RR spectra of Fe(OEP) and Fe(TPP) porphyrins. However, unusual resonance Raman enhancement has been observed for porphyrin linked arrays when exciting in the visible region. RR spectra of the *meso,meso*-linked arrays recorded in the *B*-state excitation range exhibit a complex and unusual scattering pattern. Bhuiyan, Seth, Yoshida, Osaku, and Bocian (2000) noted several striking features about the spectra (1) the observation of only polarized (A_{1g} for D_{4h}) and anomalously polarized modes (A_{2g} for D_{4h}) in the RR spectrum, (2) the enhancement of anomalously polarized vibrations with *B*-state excitation, and (3) the large differential enhancement of symmetric versus non-totally symmetric vibrations with excitation across the *B*-state absorptions. Bhuiyan, Seth, Yoshida, Osaku, and Bocian (2000) surmised that these scattering characteristics were due to the effects of symmetry lowering. The asymmetric *meso* substitution pattern inherent to the *meso,meso*-linked arrays contributes to symmetry lowering in both the ground and excited electronic states. The strong uniaxial excitonic interactions make an additional contribution to symmetry lowering in the excited state(s) promoting novel Franck–Condon and vibronic scattering mechanisms in the *B* state(s) of the arrays. Collectively, the studies of the *meso,meso*-linked arrays provide insight into the type of RR scattering that might be anticipated for other types of systems that exhibit strong excitonic interactions among the constituent

chromophores. However, the unusual scattering patterns observed by Bhuiyan, Seth, Yoshida, Osaku, and Bocian (2000) could not explain the enhancement observed when exciting Fe(OEP)Cl, Fe(TPP)Cl and [Fe(TPP)$_2$]O with near-IR excitation wavelengths, because the A$_{1g}$ modes are much more enhanced in the near-IR compared to the *B*-state region. The extremely strong scattering by the A$_{1g}$ modes implicates a true Frank–Condon mechanism at work with little or no vibronic coupling.

Akins *et al*. (Akins, 1986; Akins, Zhu, and Guo, 1996) reported that in highly conjugated systems such as cyanine dyes and porphyrin arrays other enhancement effects can also be significant. One such important mechanism is Aggregated Enhanced Raman Scattering (AERS) where bands can become enhanced through excitonic interactions between neighboring chromophores (Akins, 1986; Akins, 1986; Akins, Zhu, and Guo, 1996). In this case energy in the form of an exciton is either transferred via covalent linkages between chromophores or directly though space via overlapping π-orbitals, resulting in the enhancement of particular vibrational modes. The enhancement of vibrational modes can be explained in terms of an increase-size effect and near-resonance terms in the polarizability (Akins, Zelik, Zhu, and Guo, 1997). Excitonic coupling will essentially split the electronic states into a broad band of states with different geometries, energies, and oscillator strengths. The Raman intensities for a particular wavelength will then reflect the extent of the excitonic coupling. The net effect is that both Type *A* and Type *B* modes can become enhanced in these highly conjugate systems.

To provide more insight into the enhancement mechanism, we utilized additional spectrophotometric and crystallographic tools to find possible factors involved in the

enhancement mechanism considering the similar model compounds with different enhancement behavior. In order for excitonic interactions to occur there must be an electronic transition. UV-visible measurements show possibly a very broad weak absorption band between 800–900 nm for Fe(OEP)Cl and another between 700–750 nm for the Fe(TPP)Cl and [Fe(TPP)]$_2$O but no such band is observed for [Fe(OEP)]$_2$O. Theoretical calculations have assigned a transition at 875 nm to a $a_{2u}(\pi)$ $\rightarrow d_\pi$ transition in Fe(TPP)Cl which is not obvious in the UV-visible spectrum indicating other transitions may be in this region but low temperature magnetic circular dichroism measurements are required to validate these findings.

By far the most compelling difference between the heme compounds that show strong enhancement of A_{1g} modes when irradiating with near-IR excitation wavelengths and the [Fe(OEP)]$_2$O derivative is the number of intermolecular interactions as deduced by the *ORTEP-III* (Burnett and Johnson, 1996) calculations. It is hypothesized that the enhancement of some of the A_{1g} modes in *β*-hematin results from excitonic coupling in the extended heme aggregate through strong intermolecular interactions. Similarly, the summation of concerted weaker intermolecular interactions between the respective porphyrins appears to be the pivotal factor in explaining the enhancement of totally symmetric A_{1g} modes when exciting with near-IR excitation wavelengths. Fewer intermolecular hydrogen bond interactions between porphyrins in Fe(OEP) dimer may decrease the probability of excitonic interactions in the Fe(OEP) dimer aggregate. Supporting this argument is the indication that simple $\pi-\pi$ intramolecular contact, as between the porphyrin cores of the [Fe(OEP)]$_2$O dimer, may not be a sufficient condition to enable enhancement.

4.5 Conclusion

RR spectra of heme derivatives Fe(TPP)Cl, [Fe(TPP)]$_2$O, and Fe(OEP)Cl reveal a dramatic enhancement of totally symmetric modes (particularly ν_4) at near-IR excitation wavelengths; however, [Fe(OEP)]$_2$O does not exhibit this feature. The enhancement of the A$_{1g}$ modes in heme porphyrins at near-IR excitation could be interpreted in terms of the presence of intermolecular C–H···X hydrogen bonding where X is a π system or an electron donor atom. Consequently, the enhancement of ν_4 at near-IR excitation can be used as an indicator of the supramolecular interactions in heme aggregates. Moreover the relative intensity of ν_4 may be an indicator of the strength of concerted supramolecular interactions in heme systems. This is the first time that hydrogen bonds have been implicated in causing RR enhancement via the excitonic coupling mechanism. This study has potential implications in the development of antimalarial drugs that are designed to disrupt hydrogen bond interactions. Moreover, the discovery of the importance of hydrogen bonding interactions to transfer energy excitonically in the near-IR may have important implications in the development of heme-based nano-wires and sensors.

4.6 References

Abe, M., Kitagawa, T., Kyogoku, K. (1978). Resonance Raman spectra octaethylporphyrinato-Ni(II) and meso-deuterated and 15N substituted derivatives. II A normal coordinate analysis. **J. Chem. Phys.** 69: 4526–4534.

Adar, F., Srivastava, T. S. (1975). Resonance Raman effect in μ-oxo-bis[iron(III) tetra phenylporphyrin]. **Proc. Nat. Acad. Sci. USA** 72: 4419–4424.

Akins, D. L. (1986). Theory of Raman scattering by aggregated molecules. **J. Phys.Chem.** 90: 1530−1534.

Akins, D. L., Zhu, H. R., Guo, C. J. (1996). Aggregation of tetraaryl-substituted porphyrins in homogeneous solution. **J. Phys.Chem.** 100(13): 5420−5425.

Akins, D. L., Zelik, S., Zhu, H.-R. Guo, C. (1997). Aggregation-enhanced Raman scattering of a cyanine dye in homogeneous solution. **J. Phys.Chem. A** 101(18): 3251−3259.

Bhuiyan, A. A., Seth, J., Yoshida, N., Osaku, A., Bocian, D. F. (2000). Resonance Raman characterization of excitonically couples *meso,meso*-linked porphryin arrays. **J. Phys. Chem. B** 104(46): 10757−10764.

Bohle, D. S., Conklin, B. J., Cox, D., Madsen, S. K., Paulson, S., Stephens, P. W., Yee, G. T. (1994). Structural and spectroscopic studies of beta-hematin (the heme coordination polymer in malaria pigment. **Am. Chem. Soc. Symp. Ser.** 572: 497−515.

Brémard, C., Kowalewski, P., Merlin, J. C. (1992). Resonance Raman enhancemen of the oxo-bridged dinuclear iron center: Vibrational modes in iron(III) physiological-type porphyrin complexes. **J. Raman Spectrs.** 23: 325−333.

Brown, W. H. (1911). Malarial pigment (so-called melanin): its nature and mode of production. **J. Exp. Med.** 13: 290−299.

Burke, J. M., Kincaid, J. R., Spiro, T. G. (1978). Resonance Raman spectra and vibrational modes of iron(III) tetraphenylporphine μ-oxo dimer. Evidence for phenyl interaction and lack of dimer spitting. **J. Am. Chem. Soc.** 100(19): 6077−6083.

Burke, J. M., Kincaid, J. R., Peters, S., Gagne, R. R., Collman, J.P., Spiro, T. G. (1978). Structural-sensitive resonance Raman bands of tetraphenyl and "picket fence" porphyrin-iron complexes, including an oxyhemoglobin analogue. **J. Am. Chem. Soc.** 100(19): 6083−6088.

Burnett, M. N., Johnson, C. K. (1996). *ORTEP-III*: *Oak Ridge Thermal Ellipsoid Plot Program for Crystal Structure Illustrations*, Report ORNL-6895, Oak Ridge National Laboratory, Oak Ridge TN.

Cheng, B., Hobbs, J. D., Debrunner, P. G., Erlebacher, J., Shelnutt, J. A., Scheidt, W. R. (1995). An unusual near-eclipsed porphyrin ring orientation in two crystalline forms of (μ-oxo)bis[(octaethylporphinato)iron(III)]. Structural and molecular mechanics studies. **Inorg. Chem.** 34(1): 102−110.

Crystal Impact. (2006). *DIAMOND*. version 3.1. Crystal Impact GbR. Bonn, Germany.

Dirac, P. A. M. (1927). **Proc. Roy. Soc. (London)** 114: 710−728.

Eaton, S. S., Eaton, G. R. (1975). Rotation of phenyl rings in metal complexes of substituted tetraphenylporphyrins. **J. Am. Chem. Soc.** 97(13): 3660−3666.

Fidler, V., Ogura, T., Sato, S., Aoyagi, K., Kitagawa, T. (1991). Resonance Raman study on photoreduction of iron-porphyrins. A novel insight into the ligand-aided process. **Bull. Chem. Soc. Jpn.** 64: 2315−2322.

Fleischer, E. B., Srivastava, T. S. (1969). The structure and properties of μ-oxo-bis(tetraphenylporphineiron(III)). **J. Am. Chem. Soc.** 91(9): 2403−2405.

Francis, S., Sullivan, D. J., Goldberg, D. (1997). Hemoglobin metabolism in the malaria parasite Plasmodium Falciparum. **Annu. Rev. Micobiol.** 51: 97−123.

Fuchsman, W. H., Smith, Q. R., Stein, M. M. (1977). Direct Raman evidence for resonance interactions between the porphyrin ring system and ring-conjugated substituents in porphyrins, porphyrin dications, and metalloporphyrins. **J. Am. Chem. Soc.** 99(12): 4190–4192.

Hoard, J. L., Cohen, G. H., Glick, M. D. (1967). The stereochemistry of the coordination group in an iron(III) derivative of tetraphenylporphine[1,2]. **J. Am. Chem. Soc.** 89(9): 1992–1996.

Hoffman, A. B., Collins, D. M., Day, V. W., Fleischer, E. B., Srivastava, T. S., Hoard, J. L. (1972). The crystal structure and molecular stereochemistry of μ-oxo-bis[$\alpha,\beta,\gamma,\delta$-tetraphenylporphinatoiron(III)]. **J. Am. Chem. Soc.** 94(10): 3620–3626.

Hofmann, J. A., Bocian, D. F. (1984). Resonance Raman spectra of oxygen- and nitrogen-bridged iron octaethylporphyrin dimers. **J. Phys. Chem.** 88: 1472–1479.

Hu, S., Smith, K. M., Spiro, T. G. (1996). Assignment of protoheme resosnance Raman spectrum by heme labeling in myoglobin. **J. Am. Chem. Soc.** 118(50): 12638–12646.

Kincaid, J. R. (1999). **The Porphyrin Handbook** Vol. 7; Kadish, K. M., Smith, K. M., Guillard, R. (Eds). Academic Press, pp. 225–291.

Kitagawa, T., Abe, M., Kyogoku, Y. (1976). Resonance Raman spectra of metallopoprhyrins. Low frequency vibrations of porphyrin and iron-axial ligand stretching modes. **J. Phys. Chem.** 80: 1181–1186.

Kowalewski, P., Merlin, J. C., Bremard, C., Moreau, S. (1988). Resonance Raman evidence for μ-oxo linkage in ferriporphyrins. **J. Mol. Struct.** 175: 55−60.

Kramers, H. A., Heisenberg, W. Z. (1925). **Phys.** 31: 681−707.

Oliveira, M. F., Silva, J. R., Dansa-Petretski, M., de Souza, W., Lins, U., Braga, C. M., Masuda, H., Oliveira, P. L. (1999). Haem detoxification by an insect. **Nature** 400: 517−518.

Ozaki, Y., Mizuno, A., Sato, H., Kawaguchi, K., Muraishi, S. (1992). Biomedical application of near-infrared fouier transform Raman spectroscopy. Part I: The 1064-nm excited Raman spectra of blood and met hemoglobin. **Appl. Spectrosc.** 46: 533−535.

Pagola, S., Stephens, P. W., Bohle, D. S., Kosar, A. D., Madsen, S. K. (2000). The structure of malaria pigment β-hematin. **Nature** 404(6775): 307−310.

Paulat, F. Lehnert, N. (2008). Detailed assignment of the magnetic circular dichroism and UV-vis spectra of five-coordinate high-spin ferric [Fe(TPP)Cl]. **Inorg. Chem.** 47(11): 4963−4976.

Ridley, R. G. (2002). Malaria: To kill a parasite. **Nature** 415: 686−693.

Rush, T. S. I., Kozlowski, P. M., Piffat, C. A., Kumble, R., Zgierski, M. Z. (2000). Computational modeling of metalloporphyrin structure and vibrational spectra: Porphyrin ruffling in NiTPP. **J. Phys. Chem. B** 104(20): 5020−5034.

Sadasivan, N., Eberspaecher H. I., Fuchsman, W. H., Caugey, W. S. (1969). Substituted deuteroporphyrins. VI. Ligand-exchange and dimerization ractions of deuterohemin*. **Biochem.** 8(2): 534−541.

Scheidt, W. R., Geiger, D. K., Haller, K. J. (1982). Strucral characterization of a variable-spin(porphinato)iron(III) complex. Molecular stereochemistry of bis(3-chloropyridine) (octaethylporphinato)iron(III) perchlorate at 98 K (S = 1/2) and 293 K (S = 1/2, S = 5/2). **J. Am. Chem. Soc.** 104(2): 495–499.

Scheidt, W. R., Geiger, D. K., Hayes, R. G., Laing, G. (1983). Control of spin state in (porphinato)iron(III) complexes. An axail ligand orientation effect leading to an intermediate-spin complex. Molecular structure and physical characterization of the monoclinic form of bis(3-chloropyridine) (octaethylporphinato) iron(III) perchlorate. **J. Am. Chem. Soc.** 105(9): 2625–2632.

Scheidt, W. R., Finnegan, M. G. (1989). Structure of monoclinic chloro(meso-tetraphenylporphyrinato)iron(III). **Acta Cryst. C** 45: 1214–1216.

Selensky, R., Holten, D., Windor, M. W., Paine, J. B., Dolphin, D. (1981). Excitonic interactions in covalently-linked porphyrin dimers. **Chemical Physics.** 60: 33–46.

Senge, M. O. (2005). Chloro(2,3,7,8,12,13,17,18-octaethylporphinato)iron(III). **Acta Cryst. E** 61: m399–m400.

Shantha, P. K., Thanga, H. H., Verma, A. L. (1998). Photoreduction of Fe(TPP)Cl in CH_2Cl_2 and DMSO in the presence of and in neat 1,2-dimethylimidazole without alcohol: evidence for a photoreactive state from resonance Raman and optical absorption studied. **J. Raman Spectrosc.** 29: 997–1001.

Shelnutt, J. A., Cheung, L. D., Change, R. C. C., Yu, N., Felton, R. H. (1977). Resonance Raman spectra of metalloporphyrins. Effects of Jahn-Teller instability and nuclear distortion on excitation profiles of Stokes fundamentals. **J. Phys. Chem.** 66(8): 3387–3398.

Solomonov, I., Osipova, M., Feldman, Y., Baehtz, C., Kristian, K., Robinson, I. K., Webster, G. T., McNaughton, D., Wood, B. R., Weissbuch, I., Leiserowitz, L. (2007). Crystal nucleation, growth, and morphology of the synthetic malaria pigment β-hematin and the effect thereon by quinoline additives: the malaria pigments as a target of various antimalarial drugs. **J. Am. Chem. Soc.** 129(9): 2615−2627.

Spaulding, L. D., Chang, C. C., Yu, N., Felton, R. H. (1975). Resonance Raman spectra of metalloporphyrins. A structure probe of metal displacement. **J. Am. Chem. Soc.** 97(9): 2517−2525.

Spiro, T.G., Li, X-Y. (1988). **In Biological Applications of Raman Spectroscopy**; Spiro, T. G., Ed., Vol. 3, John Wiley & Sons, pp. 1−38.

Spiro, T. G. (1974). Resonance Raman spectroscopy: A new structure probe for biological chromophores. **Acc. Chem. Res.** 7(10): 339−344.

Strekas, T. C., Packer, A. J., Spiro, T. G. (1973). Resonance Raman spectra of ferri-hemoglobin fluoride: Three scattering regimes. **J. Raman Spectrosc.** 1: 197−206.

Strekas, T. C., Spiro, T. G. (1973). Hemoglobin resonance Raman excitation profiles with a tunalbe dye laser. **J. Raman Spectrosc.** 1: 387−392.

Swepston, P. N., Ibers, J. A. (1985). Redetermination of the structure of μ-oxo-bis [(5,10,15,20-tetraphenylporphyrinato)iron(III)] at 122 K, [Fe$_2$O(C$_{44}$H$_{28}$N$_4$)$_2$]. **Acta Cryst. C** 41: 671−673.

Tsubakin, M., Srivastava, R. B., Nai-Teng, Y. (1982). Resonance Raman investigation of carbon monoxide bonding in (carbon monoxy)hemoglobin and

-myoglobin: detection of iron-carbon monoxide stretching and iron-carbon-oxygen bending vibrations and influence of the quaternary structure change. **Biochem.** 21(6): 1132−1140.

Warshel, A., Dauber, P. (1977), Calculations of resonance Raman spectra of conjugated molecules. **J. Phys. Chem.** 66(12): 5477−5488.

Webster, G. T., Tilley, L., Deed, S., McNaughton, D., Wood, B. R. (2008). Resonance Raman spectroscopy can detect structural changes in haemozoin (malaria pigment) following incubation with chloroquine in infected erythrocytes. **FEBS Letters** 582(7): 1087−1092.

Webster, G. T., McNaughton, D., Wood, B. R. (2009). Aggreagted enhanced Raman scattering in Fe(III)PPIX solutions: The effects of concentration and chloroquine on excitonic intrations, **J. Phys. Chem. B.** Accepted pending revision.

Wood, B. R., Tait, B., McNaughton, D. (2001). Micro-Raman characterisation of the R to T state transition of haemoglobin within a single living erythrocyte. **Biochim. Biophys. Acta** 1539: 58−70.

Wood, B. R., Langford, S. J., Cooke, B. M., Glenister, F. K., Lim J., McNaughton, D. (2003). Raman imaging of hemozoin within the food vacuole of *Plasmodium falciparum* trophozoites. **FEBS Letters** 554(3): 247−252.

Wood, B. R., Langford, S. J., Cooke, B. M., Lim, J., Glenister, F. K., Duriska, M., Unthank, J. K., McNaughton, D. (2004). Resonance Raman spectroscopy reveals new insight into the electronic structure of *β*-hematin and malaria pigment. **J. Am. Chem. Soc.** 126(30): 9233−9239.

Yamamoto, T., Palmer, G. (1973). The valence and spin state of iron in oxyhemoglobin as infrared from resonance Raman spectroscopy. **J. Biol. Chem.** 248: 5211−5213.

Zerner, M., Gouterman, M., Kobayashi, H. *Theoret.* (1966). Porphyrins VIII. Extended Hückel calculations on iron complexes. **Chim. Acta** 6(5): 363−399.

CHAPTER V

A NEW MODEL FOR HEMOZOIN: Fe(OEP)PICRATE

5.1 Introduction

Metalloporphyrins as mimics for biologically functional molecules have been extensively studied. In this context both tetraphenylporphyrin, TPP, and octaethylporphyrin, OEP, iron complexes make excellent models for heme systems. Several techniques have been applied to investigate the molecular and electronic structure of iron porphyrin compounds. Among these techniques, resonance Raman (RR) spectroscopy is uniquely sensitive to stereochemical and bonding arrangements of atoms in metalloporphyrin molecules (Spiro and Strekas, 1974). It has been used to study the high-wavenumber value structurally-sensitive Raman marker bands of D_{4h} and D_{2d} molecular forms of Ni(OEP) (Spaulding, Chang, Yu, and Felton, 1975). The correlation between heme structure and Raman wavenumber value was confirmed and extended by Scholler and Hoffman (1979), Spiro, Stong, and Stein (1979), and Callahan and Badcock (1981).

RR spectroscopy is also a powerful technique to investigate evidence for electronic interaction between the porphyrin ring π system and the π systems of peripheral substituents in porphyrins and metalloporphyrins (Fuchsman, Smith, and Stein, 1977; Burke, Kincaid, and Spiro, 1978) or electronic interactions between the π systems of porphyrin rings that are not connected by covalent bonds (Chapter IV) and for analyzing the effects of π–π stacking in the different square-planar crystalline

forms of Ni(OEP) (Brennan, Scheidt, and Shelnutt, 1988) and Cu(OEP) (Sparks, Scheidt, and Shelnutt, 1992).

Specific resonance Raman bands can be used to identify *alpha* and *beta*-carbon substituents. The $\nu_2(A_{1g})$ and $\nu_{11}(B_{1g})$ modes are sensitive to the nature of *beta*-carbon substituents, while the $\nu_3(A_{1g})$, $\nu_{19}(A_{1g})$, and $\nu_{10}(B_{1g})$ are characteristic of *alpha*-carbon-methine-carbon stretching vibrations (Abe, Kitagawa, and Kyogoku, 1978). Consequently, RR spectroscopy is a powerful method to gain structural information of the various metalloporphyrins.

In terms of coordination sphere stereochemistry, μ-oxo iron(III) porphyrins such as [Fe(TPP)]$_2$O and [Fe(OEP)]$_2$O are good model systems to study the molecular and electronic structure of β-hematin. They both contain a five-coordinate high-spin iron(III) ion coordinated to an oxygen atom from the axial ligand. The RR spectrum of β-hematin shows characteristic bands of *beta* substituted hemes in the ranges of 1621–1639 and 750–756 cm^{-1} assigned to the $\nu(C_\alpha C_m)_{asym}$ and ν(pyr breathing) modes, respectively (Wood, Langford, Cooke, Lim, Glenister, Duriska, Unthank, and McNaughton, 2004). Neither of these bands appear in the spectra of Fe(TPP)Cl (Burke, Kincaid, and Spiro, 1978; Burke, Kincaid, Peters, Gagne, Collman, and Spiro, 1978; Paulat, Praneeth, Näther, and Lehnert, 2006), [Fe(TPP)]$_2$O Burke, Kincaid, and Spiro, 1978; Burke, Kincaid, Peters, Gagne, Collman, and Spiro, 1978), [Fe(TPP)(Im)$_2$]Cl (Burke, Kincaid, and Spiro, 1978), Fe(T$_{piv}$PP)Br and [Fe(T$_{piv}$PP)]$_2$O (Burke, Kincaid, Peters, Gagne, Collman, and Spiro, 1978), and (n-Bu$_4$N)[Mn(TPP)(CN)$_2$] (Galich, Hückstädt, and Homborg, 1998). Fe(OEP)picrate (Figure 5.1) on the other hand is expected to have these bands and is therefore more

similar to β-hematin in this respect. It should be noted that 1627 and 751 cm^{-1} bands

characteristic of *beta* substituted hemes, are observed in OEP derivatives.
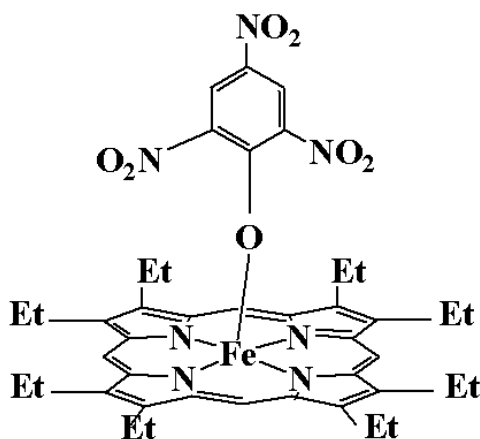
Figure 5.1 Schematic diagram of the structure of Fe(OEP)picrate.

Another reason for choosing Fe(OEP)picrate as a model compound for β-hematin is that in the solid phase, unlike [Fe(OEP)]$_2$O discussed in Chapter IV it shows the enhancement of the oxidation state marker band, ν_4 when applying near-IR excitation laser wavelengths. Thus, it would appear that the solid state electronic structure of β-hematin is different from that of [Fe(TPP)]$_2$O and [Fe(OEP)]$_2$O, but similar to that of Fe(OEP)picrate.

The application of near-IR excitation wavelengths leads to the selective resonance enhancement of oxidation state marker band ν_4, which is sensitive to the electron density of Fe(OEP)picrate and β-hematin. This chapter provides electronic and structural information using Fe(OEP)picrate as model compound for β-hematin and hemozoin. UV-visible spectroscopy revealed important generalizations about the effects of axial ligand substitution, while results from Density Functional Theory (DFT) calculations are used to support band assignments and further clarify

experimental results. The molecular structure of Fe(OEP)picrate was determined by single crystal X-ray crystallography.

Study of the stereochemistry of Fe(OEP)picrate by crystallography will help understand the importance of intermolecular bonding in β-hematin which contributes to the dramatic enhancement of totally symmetric modes at near-IR excitation wavelengths. The knowledge of stereochemistry has important implications in drug development and in understanding the heme−drug interactions occurring within the digestive vacuole of the mature parasites.

5.2 Experimental

Synthesis of Fe(OEP)picrate. 0.0153 g (0.025 mmol) Fe(OEP)Cl (Sigma Aldrich) was dissolved in 5 mL of dichloromethane followed by addition of 2 mL of 0.0185 M (0.037 mmol) picric acid solution. Subsequently, ~4 mL of ethanol and ~6−8 mL of dimethyl sulfoxide were added. The mixture was stirred vigorously until it was homogenous, then 1 mL of methanol was added and the solution allowed to stand at room temperature for 3 days. The dark blue solid product was filtered off and washed with ethanol.

Synthesis of β-hematin. Synthesis of β-hematin was based on the literature method (Slater, Swiggard, and Orton, 1991) using hematin from Sigma Aldrich.

Electronic Absorbance Spectra for Solution Phase. Electronic absorption spectra of samples were recorded on a Cary 100 Bio UV−visible spectrometer using dichloromethane as solvent for Fe(OEP)picrate and water for diluted picric acid.

Attenuated Total Reflection Fourier Transforms Infrared Spectroscopy (ATR/FTIR). ATR/FTIR spectra were recorded on a Bruker Equinox spectrometer. Solid porphyrin samples were placed on the window of an ATR cell, while picric acid solution was dried onto the window. Spectra were recorded in absorption mode at 5 cm^{-1} resolution with 60 scans.

Resonance Raman (RR) Spectroscopy. RR spectra of products were recorded on a Renishaw system 2000 spectrometer using a 413 and 514 nm excitation line generated by a Spectra Physics Ar^+ Stabilite 2017 laser system, 633 nm excitation line from a helium-neon laser, 782 nm excitation line generated by a diode laser, and 830 nm excitation line from a diode laser. The approximate laser power at the sample is 0.039, 1.3, 1.6, 0.5, and 4.04 mW for the excitation wavelength 413, 514, 633, 782, and 830 nm, respectively. The system is equipped with an Olympus optical microscope and a Zeiss ×60 water immersion objective to enable spectral acquisition in water to prevent the thermal degradation of the solid porphyrin samples. Picric acid was dried in air before recording the resonance Raman spectra without using a water immersion objective. Spectra were recorded between 1800 and 230 cm^{-1}. Each spectrum was accumulated as one scan with laser exposure of 10 sec. The percentage of power at the sample was 10% power with binning 4. The instrument was calibrated to the 520.5 cm^{-1} Si band. No change was observed in the surfaces of the samples based on microscopic examination before and at the end of data collection.

Density Functional Theory (DFT) Calculations. To assist in the analysis of IR and Raman spectra, a series of density functional theory calculations were performed at the B3LYP/6-31G(d) level using the Gaussian03 suite of programs (Frisch *et al.*,

2004). Geometry optimizations preceded vibrational frequency calculations, with wavenumber values scaled by factor 0.97.

X-ray Crystallography. A single crystal, 0.15×0.25×0.30 mm, of Fe(OEP)picrate was mounted on a hollow glass fiber with cyanoacrylate glue. All crystallographic data were obtained from a Bruker-Nonius KappaCCD diffractometer, equipped with a fine-focus molybdenum-anode (λ = 0.71073 Å) sealed-source X-ray tube operating at 50 kV and 20 mA, a horizontally mounted graphite crystal monochromator, 0.5 mm *ifg* capillary collimator, and a 95 mm CCD camera. All measurements were carried out at 295(1) K.

The complex crystallizes in the monoclinic space group *C*2/c (No. 15). The unit cell parameters, *a* = 26.3997(20), *b* = 13.7806(18), *c* = 25.4126(20) Å, *β* = 119.955(9)°, *V* = 8010.2(14) Å^3, were determined by DIRAX (Duisenberg, 1992) from fitting 104 phi/chi reflection pairs obtained from four detector settings. The calculated density for *Z* = 8 is 1.354 Mg m^{-3} and the linear absorption coefficient, μ, is 0.436 mm^{-1}. Data were collected as a series of frame images using *Collect* (Nonius BV, 1998), first by rotation about the φ axis of the goniostat, followed by rotations about the ω axis of goniostat with various φ/χ offsets to cover reciprocal space. The total scan length was 597° and the detector to crystal distance was 36 cm. Frame images were reduced to intensity data with the *EvalCCD* software (Duisenberg, Kroon-Batenburg, and Schreurs, 2003), and multi-scan absorption corrections (Blessing, 1997) were applied to the 57453 resulting data with the *SADABS* routine (Sheldrick, 2001) to provide 7394 unique Friedel merged data ($R_{sym(2/m)}$ = 0.0903;

$-31 \leq h \leq 31$, $0 \leq k \leq 16$, $0 \leq l \leq 30$) for which 4597 have $I > 2\sigma(I)$ in the range 3.08°

< 2θ < 50.90°, giving a data completeness of 0.998 and a resolution of 0.827 Å.

The structure was solved using the *DIRDIF* system (Beurskens, Beurskens, Bosman, de Gelder, Granda, Gould, Israël, and Smits, 1996), which located the iron atom by the Patterson method and the other 56 nonhydrogen atoms by direct methods applied to the resulting difference structure factors. The structure was refined by full-matrix least-squares based on F^2 using the *SHELXL-97* (Sheldrick, 1997) software package.

Preliminary refinement showed apparent excess thermal motion of one oxygen atom of the *para*-nitro group of the axial picrato ligand. The nitro group was split into two with occupancy factors of α and 1 − α. The nitrogen atom and one oxygen atom overlap considerably requiring use of restraints to control refinement of the disorder. The final cycles of refinement included all nonhydrogen atoms with refined anisotropic atomic displacement parameters, and included the 46 hydrogen atoms as riding model contributions in idealized positions (d[C−H$_{methine}$] = 0.93 Å, d[C−H$_{methylene}$] = 0.97 Å, and d[C−H$_{methyl}$] = 0.96 Å) with thermal parameters 10% larger than those of the respective carbon atom to which the hydrogen atom is attached. Eight additional variables were added to allow rotational freedom for each of the eight methyl groups.

Refinement converged with $R_1 = \Sigma ||F_o| - |F_c|| / \Sigma |F_o| = 0.049$, $R_2 = (\Sigma w(|F_o| - |F_c|)^2 / \Sigma w(|F_o|^2))^{1/2} = 0.106$, and the standard deviation of an observation of unit weight = 1.012. For the final cycle of refinement the number of observations was 7394 (4597 with $I > 2\sigma(I)$). The largest peak in the final difference electron density map was 0.26(5) e Å^{-3} and the deepest hole was −0.29 e Å^{-3}. Crystal

data and details of the data collection and structural refinement are summarized in Table 5.1. Fractional monoclinic coordinates and equivalent isotropic atomic displacement parameters for the nonhydrogen atoms, fractional monoclinic coordinates and isotropic atomic displacement parameters for the hydrogen atoms, and anisotropic atomic displacement parameters for the nonhydrogen atoms are given in Table 5.2, 5.3, and 5.4, respectively. Selected interatomic bond distances are given in Table 5.5 and angles in Table 5.6. A perspective diagram of the molecule, including the atom numbering scheme is displayed in Figure 5.2.
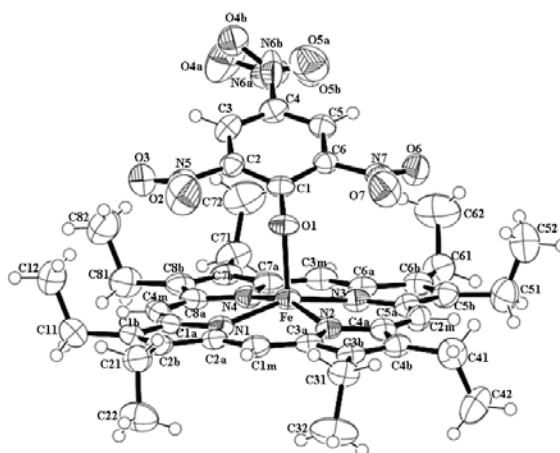
Figure 5.2 *ORTEP* diagram showing molecular structure of Fe(OEP)picrate.

Table 5.1 Crystal Data and Refinement Details for Fe(OEP)picrate.

Parameter	Value
Crystal data	
Chemical formula	$C_{42}H_{46}FeN_7O_7$
M_r (Daltons)	816.71
Cell setting, space group	monoclinic, $C2/c$ (No. 15)
Temperature (K)	298 (1)
a, b, c, (Å)	26.3997 (20), 13.7806 (18), 25.4126 (20)
β (°)	119.955 (9)°
V, Å^3	8010.2 (14)

Table 5.1 (Continued)

Z	8
D_c, (Mg m^{-3})	1.354
Radiation type / wavelength	Mo $K\alpha$ / $\lambda = 0.71073$ Å
μ (mm^{-1})	0.436
Crystal form, color	equant habit,
Crystal size (mm)	$0.15 \times 0.26 \times 0.30$

Data collection

Diffractometer	KappaCCD 95 mm CCD camera
Data collection method	$\varphi + \omega$ scans, total length 597°, Dx 36 cm
Absorption correction	multi-scan, nl = 36 (based on symmetry-related measurements)
T_{min}	0.880
T_{max}	0.939
No. of measured, independent and observed reflections	57453, 7394, 4597
Criterion for observed reflections	$I > 2\sigma(I)$
R_{int}	0.090
θ_{max} (°)	25.5

Refinement

Refinement based on	F^2
$R[F^2 > 2\sigma(F^2)]$, $wR(F^2)$, S	0.049, 0.106, 1.01
No. of reflections	7394 reflections
No. of parameters	550
H-atom treatment	Mixed independent and constrained refinement
Weighting scheme	calculated $w = 1/[\sigma^2(F_0^2) + (0.0327P)^2 + 10.7372P]$ where $P = (F_0^2 + 2F_c^2)/3$
$(\Delta/\sigma)_{max}$	0.034
$\Delta\rho_{max}$, $\Delta\rho_{min}$, err (e Å^{-3})	0.26, −0.29, 0.05

Computer programs: *Collect* (Nonius BV, 1998); *DIRAX* (Duisenberg, 1992); *EvalCCD* (Duisenberg, Kroon-Batenburg, and Schreurs, 2003); *DIRDIF* (Beurskens, Beurskens, Bosman, de Gelder, Granda, Gould, Israël, and Smits, 1996); *SADABS* (Sheldrick, 2001); *SHELXL-97* (Sheldrick, 1997); *ORTEP-III* (Burnett and Johnson, 1996; Farrugia, 1997).

Table 5.2 Fractional Monoclinic Coordinates and Equivalent Isotropic Atomic Displacement Parameters for the Nonhydrogen Atoms of Fe(OEP)picrate.[a]

Atom	x	y	z	U_{iso} (Å^2)	restraints[b]	group[c]
Fe1	0.052188(16)	0.92208(3)	0.111590(17)	0.03622(13)	.	.	.
N1	0.00803(9)	1.04042(17)	0.11596(10)	0.0391(6)	.	.	.
CA1	0.01585(12)	1.1352(2)	0.10389(13)	0.0417(7)	.	.	.
CB1	−0.01175(12)	1.2007(2)	0.12651(13)	0.0461(8)	.	.	.
C11	−0.00908(14)	1.3090(2)	0.12468(16)	0.0628(10)	.	.	.
C12	0.04576(16)	1.3498(3)	0.17705(18)	0.0840(12)	.	.	.
CB2	−0.03655(12)	1.1452(2)	0.15178(13)	0.0443(8)	.	.	.
C21	−0.07088(13)	1.1784(2)	0.18116(14)	0.0561(9)	.	.	.
C22	−0.13610(14)	1.1718(3)	0.14052(16)	0.0720(11)	.	.	.
CA2	−0.02399(11)	1.0456(2)	0.14527(12)	0.0393(7)	.	.	.
CM1	−0.04189(12)	0.9653(2)	0.16454(12)	0.0415(7)	.	.	.
N2	0.00143(9)	0.83868(17)	0.13257(10)	0.0367(6)	.	.	.
CA3	−0.03209(11)	0.8691(2)	0.15751(12)	0.0362(7)	.	.	.
CB3	−0.05449(11)	0.7874(2)	0.17447(12)	0.0404(7)	.	.	.
C31	−0.09452(12)	0.7939(2)	0.20060(13)	0.0479(8)	.	.	.
C32	−0.15755(14)	0.8089(3)	0.15348(16)	0.0856(13)	.	.	.
C32	−0.15755(14)	0.8089(3)	0.15348(16)	0.0856(13)	.	.	.
CB4	−0.03452(12)	0.7065(2)	0.16031(12)	0.0412(7)	.	.	.
C41	−0.04679(14)	0.6023(2)	0.16622(14)	0.0548(9)	.	.	.
C42	−0.09455(17)	0.5597(3)	0.10747(17)	0.0796(12)	.	.	.
CA4	0.00045(12)	0.7385(2)	0.13435(12)	0.0399(7)	.	.	.
CM2	0.02751(12)	0.6783(2)	0.11297(13)	0.0429(7)	.	.	.
N3	0.06845(9)	0.80075(17)	0.07537(10)	0.0393(6)	.	.	.
CA5	0.05876(12)	0.7052(2)	0.08470(12)	0.0401(7)	.	.	.
CB5	0.08541(13)	0.6401(2)	0.06128(13)	0.0480(8)	.	.	.
C51	0.08530(16)	0.5309(2)	0.06581(16)	0.0643(10)	.	.	.
C52	0.13420(19)	0.4936(3)	0.1251(2)	0.0978(14)	.	.	.
CB6	0.11146(12)	0.6957(2)	0.03777(13)	0.0462(8)	.	.	.
C61	0.14645(14)	0.6638(3)	0.00874(15)	0.0605(9)	.	.	.
C62	0.21162(16)	0.6699(4)	0.05007(19)	0.0967(15)	.	.	.
CA6	0.10093(11)	0.7955(2)	0.04644(12)	0.0393(7)	.	.	.
CM3	0.11989(12)	0.8763(3)	0.02888(12)	0.0450(8)	.	.	.
N4	0.07702(9)	1.00366(17)	0.06067(10)	0.0385(6)	.	.	.
CA7	0.10961(12)	0.9723(2)	0.03515(12)	0.0413(7)	.	.	.
CB7	0.12967(12)	1.0538(2)	0.01512(12)	0.0452(8)	.	.	.
C71	0.16781(14)	1.0468(3)	−0.01279(14)	0.0611(10)	.	.	.
C72	0.23198(15)	1.0305(3)	0.03352(18)	0.0869(13)	.	.	.
CB8	0.10804(12)	1.1346(2)	0.02689(13)	0.0467(8)	.	.	.
C81	0.11604(14)	1.2377(2)	0.01334(15)	0.0635(10)	.	.	.
C82	0.17507(17)	1.2805(3)	0.05733(18)	0.0912(13)	.	.	.
CA8	0.07495(12)	1.1031(2)	0.05524(12)	0.0430(8)	.	.	.
CM4	0.04638(12)	1.1634(2)	0.07523(13)	0.0453(8)	.	.	.
O1	0.12367(7)	0.92991(14)	0.18869(8)	0.0414(5)	.	.	.
C1	0.17559(12)	0.9409(2)	0.19702(11)	0.0372(7)	.	A	.
C2	0.20224(12)	1.0331(2)	0.20365(12)	0.0410(7)	D	.	.
N5	0.17356(12)	1.1207(2)	0.20972(13)	0.0572(7)	D	.	.
O2	0.14385(12)	1.1132(2)	0.23341(13)	0.0902(9)	D	.	.
O3	0.18302(11)	1.19746(18)	0.19198(12)	0.0767(8)	D	.	.
C3	0.25435(13)	1.0460(2)	0.20523(13)	0.0499(8)	.	A	.

Table 5.2 (Continued)

Atom	x	y	z	U_{iso} (Å^2)	restraints[b]		group[c]
C4	0.28314(13)	0.9655(2)	0.20171(14)	0.0448(8)	D	.	.
N6A[d]	0.3375(4)	0.9795(10)	0.2000(8)	0.068(7)	P D	A	1
O4A[d]	0.3550(16)	1.0628(16)	0.205(2)	0.120(8)	P D	A	1
O5A[d]	0.3583(7)	0.9100(10)	0.1880(9)	0.096(7)	P D	A	1
N6B[d]	0.3398(8)	0.9765(14)	0.2049(13)	0.077(13)	P D	A	2
O4B[d]	0.3696(7)	1.0475(14)	0.2312(12)	0.064(7)	P D	A	2
O5B[d]	0.3559(10)	0.9117(15)	0.1843(13)	0.069(10)	P D	A	2
C5	0.26277(12)	0.8740(2)	0.19913(12)	0.0422(7)	.	A	.
C6	0.21091(11)	0.8621(2)	0.19846(12)	0.0369(7)	D	.	.
N7	0.19315(11)	0.7620(2)	0.19989(11)	0.0471(6)	D	.	.
O6	0.21147(10)	0.69845(17)	0.17998(10)	0.0634(6)	D	.	.
O7	0.16311(10)	0.74540(17)	0.22267(12)	0.0727(7)	D	.	.

[a] The numbers given in parentheses are the estimated standard deviations in the least significant digits.

[b] Letters indicate an atom involved in a refinement restraint: A = angle restraint, D = distance restraints, and P = occupancy restraint.

[c] Numbers indicate the disorder group an atom belongs to.

[d] Disordered *para*-nitro group on the picrato ligand. Occupancy of major orientation, A, is 0.65; d[N6a−N6b] = 0.12 Å; d[O4a−O4b] = 0.09 Å; d[O5a−O5b] = 0.61 Å.

Table 5.3 Fractional Monoclinic Coordinates and Isotropic Atomic Displacement

Parameters for the Hydrogen Atoms of Fe(OEP)picrate.[a]

Atom	x	y	z	U_{iso} (Å^2)
H11A	−0.0427	1.3362	0.1253	0.069
H11B	−0.0112	1.3285	0.0869	0.069
H12A	0.0465	1.3353	0.2144	0.092
H12B	0.0466	1.4188	0.1725	0.092
H12C	0.0792	1.3212	0.1777	0.092
H21A	−0.0596	1.1395	0.2171	0.062
H21B	−0.0606	1.2453	0.1941	0.062
H22A	−0.1479	1.2111	0.1051	0.079
H22B	−0.1551	1.1947	0.1620	0.079
H22C	−0.1470	1.1056	0.1286	0.079
HM1	−0.0628	0.9776	0.1844	0.046
H31A	−0.0911	0.7346	0.2227	0.053
H31B	−0.0819	0.8472	0.2293	0.053
H32A	−0.1621	0.8710	0.1345	0.094
H32B	−0.1811	0.8066	0.1725	0.094
H32C	−0.1697	0.7588	0.1233	0.094
H41A	−0.0581	0.5968	0.1970	0.060
H41B	−0.0113	0.5649	0.1797	0.060
H42A	−0.1296	0.5972	0.0933	0.088
H42B	−0.1018	0.4939	0.1142	0.088
H42C	−0.0825	0.5609	0.0775	0.088
HM2	0.0246	0.6121	0.1180	0.047
H51A	0.0483	0.5101	0.0613	0.071
H51B	0.0888	0.5029	0.0327	0.071
H52A	0.1710	0.5073	0.1276	0.108
H52B	0.1301	0.4247	0.1274	0.108

Table 5.3 (Continued)

Atom	x	y	z	U_{iso} (Å²)
H52C	0.1327	0.5248	0.1581	0.108
H61A	0.1361	0.5973	−0.0050	0.067
H61B	0.1356	0.7038	−0.0267	0.067
H62A	0.2224	0.7356	0.0636	0.106
H62B	0.2309	0.6496	0.0284	0.106
H62C	0.2231	0.6283	0.0845	0.106
HM3	0.1423	0.8643	0.0107	0.049
H71A	0.1641	1.1061	−0.0350	0.067
H71B	0.1541	0.9937	−0.0417	0.067
H72A	0.2454	1.0811	0.0635	0.096
H72B	0.2545	1.0313	0.0134	0.096
H72C	0.2365	0.9688	0.0529	0.096
H81A	0.0859	1.2774	0.0138	0.070
H81B	0.1106	1.2406	−0.0273	0.070
H82A	0.1811	1.2774	0.0978	0.100
H82B	0.1764	1.3469	0.0467	0.100
H82C	0.2052	1.2443	0.0554	0.100
HM4	0.0477	1.2295	0.0688	0.050
H3	0.2699	1.1077	0.2086	0.055
H5	0.2836	0.8205	0.1979	0.046

[a] The numbers given in parentheses are the estimated standard deviations in the least significant digits.

Table 5.4 Anisotropic Atomic Displacement Parameters for the Nonhydrogen Atoms of Fe(OEP)picrate.[a]

Atom	U_{11}	U_{22}	U_{33}	U_{23}	U_{13}	U_{12}
Fe1	0.0278(2)	0.0466(3)	0.0352(2)	0.0019(2)	0.01639(18)	−0.00115(19)
N1	0.0277(12)	0.0467(16)	0.0413(14)	0.0005(11)	0.0161(12)	−0.0012(11)
CA1	0.0263(15)	0.049(2)	0.0389(17)	0.0058(14)	0.0079(14)	0.0022(14)
CB1	0.0321(16)	0.046(2)	0.0461(19)	0.0012(15)	0.0091(15)	0.0061(14)
C11	0.056(2)	0.055(2)	0.069(2)	0.0036(18)	0.024(2)	0.0104(17)
C12	0.086(3)	0.053(2)	0.092(3)	0.002(2)	0.029(3)	−0.011(2)
CB2	0.0291(16)	0.054(2)	0.0419(18)	−0.0090(15)	0.0116(15)	0.0000(14)
C21	0.049(2)	0.059(2)	0.057(2)	−0.0119(17)	0.0245(18)	0.0037(16)
C22	0.052(2)	0.104(3)	0.065(2)	−0.005(2)	0.034(2)	0.016(2)
CA2	0.0274(15)	0.048(2)	0.0365(17)	−0.0041(14)	0.0116(14)	−0.0021(13)
CM1	0.0306(16)	0.058(2)	0.0388(17)	−0.0054(15)	0.0193(14)	−0.0030(14)
N2	0.0290(13)	0.0454(17)	0.0360(14)	−0.0011(11)	0.0165(11)	−0.0020(11)
CA3	0.0227(14)	0.053(2)	0.0290(15)	−0.0026(13)	0.0099(13)	−0.0034(13)
CB3	0.0297(16)	0.057(2)	0.0319(16)	0.0007(14)	0.0135(14)	−0.0061(14)
C31	0.0390(17)	0.067(2)	0.0475(18)	0.0068(16)	0.0289(16)	−0.0013(15)
C32	0.043(2)	0.156(4)	0.067(3)	0.017(3)	0.034(2)	0.004(2)
CB4	0.0352(16)	0.052(2)	0.0375(17)	0.0020(14)	0.0188(15)	−0.0078(14)
C41	0.059(2)	0.058(2)	0.061(2)	0.0083(17)	0.0405(19)	−0.0027(17)
C42	0.099(3)	0.062(3)	0.080(3)	−0.013(2)	0.047(3)	−0.030(2)
CA4	0.0341(16)	0.047(2)	0.0372(17)	0.0010(14)	0.0169(14)	−0.0027(14)
CM2	0.0415(17)	0.0413(19)	0.0496(19)	−0.0004(14)	0.0254(16)	−0.0054(14)
N3	0.0333(13)	0.0518(17)	0.0359(13)	−0.0016(11)	0.0197(12)	−0.0023(11)
CA5	0.0351(16)	0.045(2)	0.0390(17)	−0.0035(14)	0.0180(15)	−0.0035(14)
CB5	0.0449(19)	0.054(2)	0.0441(19)	−0.0079(16)	0.0213(16)	−0.0006(16)

Table 5.4 (Continued)

Atom	U_{11}	U_{22}	U_{33}	U_{23}	U_{13}	U_{12}
C51	0.074(2)	0.056(2)	0.078(3)	−0.0126(19)	0.050(2)	−0.0012(19)
C52	0.109(3)	0.059(3)	0.118(4)	0.004(3)	0.051(3)	0.005(2)
CB6	0.0392(17)	0.063(2)	0.0362(17)	−0.0057(15)	0.0189(15)	0.0015(15)
C61	0.060(2)	0.072(3)	0.060(2)	−0.0125(18)	0.039(2)	−0.0001(18)
C62	0.064(3)	0.149(4)	0.093(3)	−0.019(3)	0.052(3)	0.014(3)
CA6	0.0304(15)	0.055(2)	0.0312(16)	−0.0014(14)	0.0147(14)	−0.0012(14)
CM3	0.0338(17)	0.072(2)	0.0335(17)	−0.0010(15)	0.0198(15)	−0.0032(16)
N4	0.0312(13)	0.0478(17)	0.0365(14)	0.0053(11)	0.0168(12)	−0.0002(11)
CA7	0.0319(16)	0.061(2)	0.0282(16)	0.0039(14)	0.0130(14)	−0.0025(15)
CB7	0.0326(16)	0.068(2)	0.0301(16)	0.0062(14)	0.0117(14)	−0.0102(15)
C71	0.062(2)	0.083(3)	0.050(2)	0.0003(17)	0.0367(19)	−0.0154(19)
C72	0.063(3)	0.121(4)	0.094(3)	−0.017(3)	0.053(3)	−0.012(2)
CB8	0.0366(17)	0.061(2)	0.0355(17)	0.0125(15)	0.0130(15)	−0.0036(16)
C81	0.059(2)	0.072(3)	0.064(2)	0.0155(19)	0.034(2)	−0.0068(18)
C82	0.088(3)	0.072(3)	0.095(3)	−0.004(2)	0.032(3)	−0.023(2)
CA8	0.0304(16)	0.056(2)	0.0352(17)	0.0094(14)	0.0107(14)	−0.0012(14)
CM4	0.0355(17)	0.0433(19)	0.0486(19)	0.0100(15)	0.0146(16)	0.0019(14)
O1	0.0264(10)	0.0619(14)	0.0349(11)	0.0023(9)	0.0144(9)	0.0003(9)
C1	0.0335(16)	0.052(2)	0.0226(14)	0.0001(12)	0.0114(13)	0.0003(14)
C2	0.0395(17)	0.0430(19)	0.0382(17)	−0.0065(13)	0.0177(15)	−0.0012(14)
N5	0.0473(17)	0.058(2)	0.0529(18)	−0.0141(15)	0.0151(15)	−0.0012(15)
O2	0.094(2)	0.088(2)	0.118(2)	−0.0260(17)	0.074(2)	0.0043(16)
O3	0.0732(17)	0.0493(17)	0.0861(19)	−0.0023(14)	0.0236(15)	0.0047(13)
C3	0.051(2)	0.047(2)	0.052(2)	−0.0095(15)	0.0261(17)	−0.0147(16)
C4	0.0355(18)	0.056(2)	0.0504(19)	−0.0035(15)	0.0270(16)	−0.0062(16)
N6A	0.041(6)	0.097(16)	0.089(10)	0.002(8)	0.050(6)	−0.021(6)
O4A	0.113(11)	0.109(7)	0.19(2)	−0.040(9)	0.117(14)	−0.059(7)
O5A	0.076(9)	0.106(14)	0.113(11)	0.003(10)	0.052(9)	0.016(8)
N6B	0.12(3)	0.035(16)	0.082(17)	−0.005(11)	0.052(14)	0.007(13)
O4B	0.043(8)	0.060(9)	0.097(12)	0.003(7)	0.041(8)	−0.007(7)
O5B	0.069(14)	0.069(19)	0.13(2)	0.013(15)	0.093(16)	0.008(12)
C5	0.0359(17)	0.050(2)	0.0414(18)	0.0008(14)	0.0196(15)	0.0037(15)
C6	0.0350(16)	0.0409(19)	0.0317(16)	0.0013(13)	0.0143(14)	−0.0016(13)
N7	0.0414(15)	0.0523(19)	0.0400(15)	0.0077(13)	0.0147(13)	−0.0002(13)
O6	0.0708(16)	0.0507(15)	0.0655(15)	−0.0060(12)	0.0317(13)	−0.0021(12)
O7	0.0743(17)	0.0672(17)	0.0945(19)	0.0224(14)	0.0555(16)	−0.0011(13)

[a] The numbers given in parentheses are the estimated standard deviations in the least significant digits.

Table 5.5 Selected Interatomic Distances for Fe(OEP)picrate.[a]

Atom 1	Atom 2	Distance (Å)
Fe1	O1	1.9286(17)
Fe1	N2	2.028(2)
Fe1	N1	2.040(2)
Fe1	N4	2.053(2)
Fe1	N3	2.055(2)
N1	CA2	1.379(3)
N1	CA1	1.381(4)
CA1	CM4	1.385(4)
CA1	CB1	1.447(4)
CB1	CB2	1.359(4)

Table 5.5 (Continued)

Atom 1	Atom 2	Distance (Å)
CB1	C11	1.496(4)
C11	C12	1.503(4)
CB2	CA2	1.441(4)
CB2	C21	1.505(4)
C21	C22	1.505(4)
CA2	CM1	1.385(4)
CM1	CA3	1.380(4)
N2	CA4	1.382(4)
N2	CA3	1.386(3)
CA3	CB3	1.433(4)
CB3	CB4	1.357(4)
CB3	C31	1.506(4)
C31	C32	1.502(4)
CB4	CA4	1.446(4)
CB4	C41	1.496(4)
C41	C42	1.511(4)
CA4	CM2	1.371(4)
CM2	CA5	1.388(4)
N3	CA6	1.382(3)
N3	CA5	1.385(3)
CA5	CB5	1.440(4)
CB5	CB6	1.352(4)
CB5	C51	1.508(4)
C51	C52	1.503(5)
CB6	CA6	1.441(4)
CB6	C61	1.507(4)
C61	C62	1.505(5)
CA6	CM3	1.383(4)
CM3	CA7	1.375(4)
N4	CA8	1.376(4)
N4	CA7	1.380(4)
CA7	CB7	1.439(4)
CB7	CB8	1.351(4)
CB7	C71	1.496(4)
C71	C72	1.521(4)
CB8	CA8	1.449(4)
CB8	C81	1.501(4)
C81	C82	1.512(4)
CA8	CM4	1.378(4)
CM4	HM4	0.9300
O1	C1	1.287(3)
C1	C6	1.419(4)
C1	C2	1.422(4)
C2	C3	1.368(4)
C2	N5	1.474(4)
N5	O2	1.208(3)
N5	O3	1.223(3)
C3	C4	1.373(4)
C4	C5	1.359(4)
C4	N6B[b]	1.465(10)
C4	N6A[b]	1.471(6)
N6A[b]	O4A[b]	1.219(9)
N6A[b]	O5A[b]	1.217(7)
N6B[b]	O5B[b]	1.214(9)
N6B[b]	O4B[b]	1.224(10)

Table 5.5 (Continued)

Atom 1	Atom 2	Distance (Å)
C5	C6	1.371(4)
C6	N7	1.464(4)
N7	O7	1.215(3)
N7	O6	1.225(3)

[a] The numbers given in parentheses are the estimated standard deviations in the least significant digits.
[b] Disordered *para*-nitro group on the picrato ligand. Occupancy of major orientation, A, is 0.65.

Table 5.6 Selected Interatomic Angles for Fe(OEP)picrate.[a]

Atom 1	Atom 2	Atom 3	Angle (°)
O1	Fe1	N2	101.80(8)
O1	Fe1	N1	101.30(8)
N2	Fe1	N1	88.17(9)
O1	Fe1	N4	98.70(8)
N2	Fe1	N4	159.50(8)
N1	Fe1	N4	88.14(9)
O1	Fe1	N3	100.56(8)
N2	Fe1	N3	88.28(9)
N1	Fe1	N3	158.12(9)
N4	Fe1	N3	87.67(9)
CA2	N1	CA1	105.7(2)
CA2	N1	Fe1	126.3(2)
CA1	N1	Fe1	126.27(19)
N1	CA1	CM4	124.9(3)
N1	CA1	CB1	109.9(3)
CM4	CA1	CB1	125.1(3)
CB2	CB1	CA1	107.1(3)
CB2	CB1	C11	128.2(3)
CA1	CB1	C11	124.7(3)
CB1	C11	C12	112.6(3)
CB1	CB2	CA2	106.8(3)
CB1	CB2	C21	127.9(3)
CA2	CB2	C21	125.2(3)
C22	C21	CB2	114.1(3)
N1	CA2	CM1	124.0(3)
N1	CA2	CB2	110.4(3)
CM1	CA2	CB2	125.6(3)
CA3	CM1	CA2	127.1(3)
CA4	N2	CA3	105.1(2)
CA4	N2	Fe1	126.88(19)
CA3	N2	Fe1	127.27(19)
CM1	CA3	N2	123.6(3)
CM1	CA3	CB3	125.7(3)
N2	CA3	CB3	110.7(3)
CB4	CB3	CA3	107.0(2)
CB4	CB3	C31	128.1(3)
CA3	CB3	C31	124.9(3)
C32	C31	CB3	113.5(2)
CB3	CB4	CA4	107.0(3)
CB3	CB4	C41	129.1(3)

Table 5.6 (Continued)

Atom 1	Atom 2	Atom 3	Angle (°)
CA4	CB4	C41	123.9(3)
CB4	C41	C42	112.9(3)
CM2	CA4	N2	124.7(3)
CM2	CA4	CB4	125.0(3)
N2	CA4	CB4	110.2(3)
CA4	CM2	CA5	127.3(3)
CA6	N3	CA5	105.0(2)
CA6	N3	Fe1	127.2(2)
CA5	N3	Fe1	126.84(18)
N3	CA5	CM2	123.4(3)
N3	CA5	CB5	110.6(3)
CM2	CA5	CB5	126.0(3)
CB6	CB5	CA5	106.9(3)
CB6	CB5	C51	128.3(3)
CA5	CB5	C51	124.7(3)
C52	C51	CB5	112.6(3)
CB5	CB6	CA6	107.1(3)
CB5	CB6	C61	128.5(3)
CA6	CB6	C61	124.4(3)
C62	C61	CB6	114.1(3)
N3	CA6	CM3	123.4(3)
N3	CA6	CB6	110.4(3)
CM3	CA6	CB6	126.2(3)
CA7	CM3	CA6	127.8(3)
CA8	N4	CA7	105.5(2)
CA8	N4	Fe1	126.8(2)
CA7	N4	Fe1	126.5(2)
CM3	CA7	N4	124.1(3)
CM3	CA7	CB7	125.5(3)
N4	CA7	CB7	110.4(3)
CB8	CB7	CA7	107.1(3)
CB8	CB7	C71	128.1(3)
CA7	CB7	C71	124.8(3)
CB7	C71	C72	113.3(3)
CB7	CB8	CA8	106.8(3)
CB7	CB8	C81	127.3(3)
CA8	CB8	C81	125.9(3)
CB8	C81	C82	114.2(3)
N4	CA8	CM4	124.4(3)
N4	CA8	CB8	110.2(3)
CM4	CA8	CB8	125.4(3)
CA8	CM4	CA1	126.5(3)
C1	O1	Fe1	126.52(17)
O1	C1	C6	123.1(3)
O1	C1	C2	123.2(3)
C6	C1	C2	113.6(2)
C3	C2	C1	123.4(3)
C3	C2	N5	116.9(3)
C1	C2	N5	119.7(3)
O2	N5	O3	124.1(3)
O2	N5	C2	118.5(3)
O3	N5	C2	117.4(3)
C2	C3	C4	118.4(3)
C5	C4	C3	122.3(3)
C5	C4	N6B [b]	117.9(8)

Table 5.6 (Continued)

Atom 1	Atom 2	Atom 3	Angle (°)
C3	C4	N6B [b]	119.7(8)
C5	C4	N6A [b]	119.3(6)
C3	C4	N6A [b]	118.4(6)
O4A [b]	N6A [b]	O5A [b]	125.2(10)
O4A [b]	N6A [b]	C4	116.2(10)
O5A [b]	N6A [b]	C4	118.3(9)
O5B [b]	N6B [b]	O4B [b]	123.7(15)
O5B [b]	N6B [b]	C4	117.9(12)
O4B [b]	N6B [b]	C4	118.2(13)
C4	C5	C6	118.7(3)
C5	C6	C1	123.3(3)
C5	C6	N7	116.3(3)
C1	C6	N7	120.5(3)
O7	N7	O6	123.3(3)
O7	N7	C6	118.9(3)
O6	N7	C6	117.8(3)

[a] The numbers given in parentheses are the estimated standard deviations in the least significant digits.
[b] Disordered *para*-nitro group on the picrato ligand. Occupancy of major orientation, A, is 0.65.

Density Functional Theory (DFT) Calculations. To assist in the analysis of IR and Raman spectra, a series of DFT calculations were performed at the B3LYP/6-31G(d) level using the Gaussian03 suite of programs (Frisch *et al*., 2004). Geometry optimizations preceded vibrational frequency calculations, with wavenumber values scaled by the factor 0.97.

5.3 Results and Discussion

UV-visible Spectroscopy. The electronic spectra are useful in distinguishing the Fe(OEP)picrate and Fe(OEP)Cl as product and starting material, respectively by the differences in the λ_{max}. Fe(OEP)picrate has a very intense blue-shifted Soret band and a strong single feature near the visible region. Addition of Fe(OEP) was formed by O atom of picrate which is an acidic ligand forming complex by electrostatic with

iron(III) and hydrogen bond interactions with porphyrin plane exhibits the absorption band at longer wavelength shown in Figure 5.3.

Attenuated Total Reflection Fourier Transform Infrared Spectroscopy (ATR/FTIR). ATR/FTIR spectra are shown in Figure 5.4. The frequency of ν(C−O) at 1270 cm^{-1} in free picric acid is shifted to higher frequency at 1283 cm^{-1} in Fe(OEP)picrate. Because the hydrogen atom of OH group in picric acid is replaced by iron(III) increasing the π-character in the C−O bond. It corresponded with the frequency of δ(OH) of picric acid is the band at 1612 cm^{-1} and disappeared in Fe(OEP)picrate. The frequency of $\nu_{as}(NO)_2$ and $\nu_s(NO)_2$ assigned at 1540 and 1339 cm^{-1} in picric acid split to 1533, 1582 cm^{-1} and 1331, 1367 cm^{-1} in Fe(OEP)picrate (Wang, Liu, Tang, Tan, and Yu, 2003).

Resonance Raman Spectroscopy

(a) Assignment of the RR Spectra of Solid State Picric Acid. Experimental RR spectra of deep yellow picric acid are compared with a computed (DFT) spectrum in Figure 5.5. Observed and computed wavenumber values are listed in Table B1 and B2 (Appendix B), respectively. The bands at 1610, 1345, and 830 cm^{-1} were assigned to the antisymmetric stretch, symmetric stretch, and in-plane (scissoring) deformation, respectively of the aromatic NO_2 groups of picric acid. The exact position of the in-plane NO_2 wagging deformation cannot be verified (Lewis, Lewis, and Griffiths, 2005), however in this work, a broad band at 722 cm^{-1} was expected.
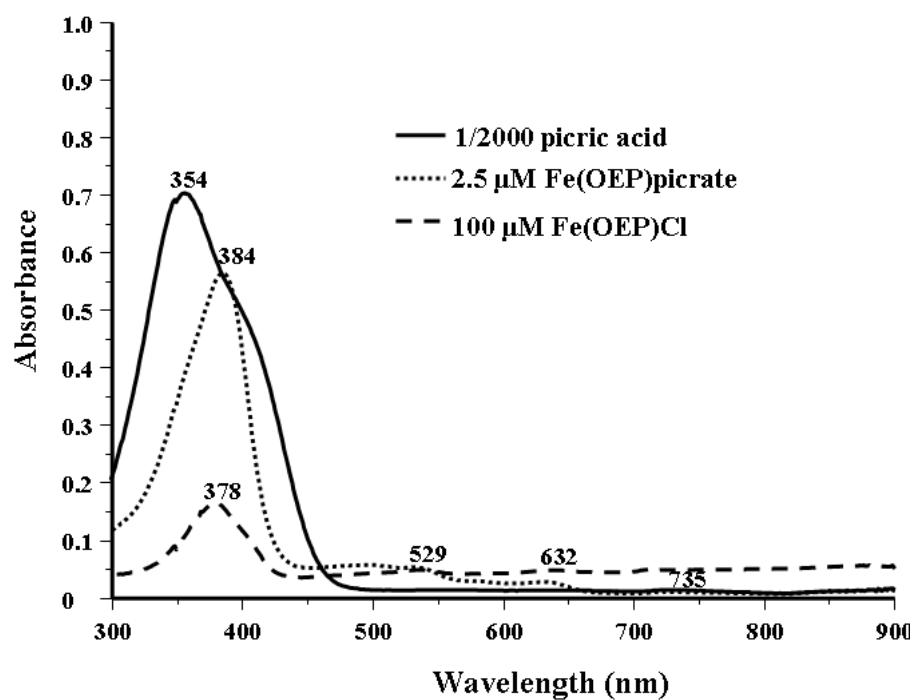
Figure 5.3 UV-visible absorbance spectra.
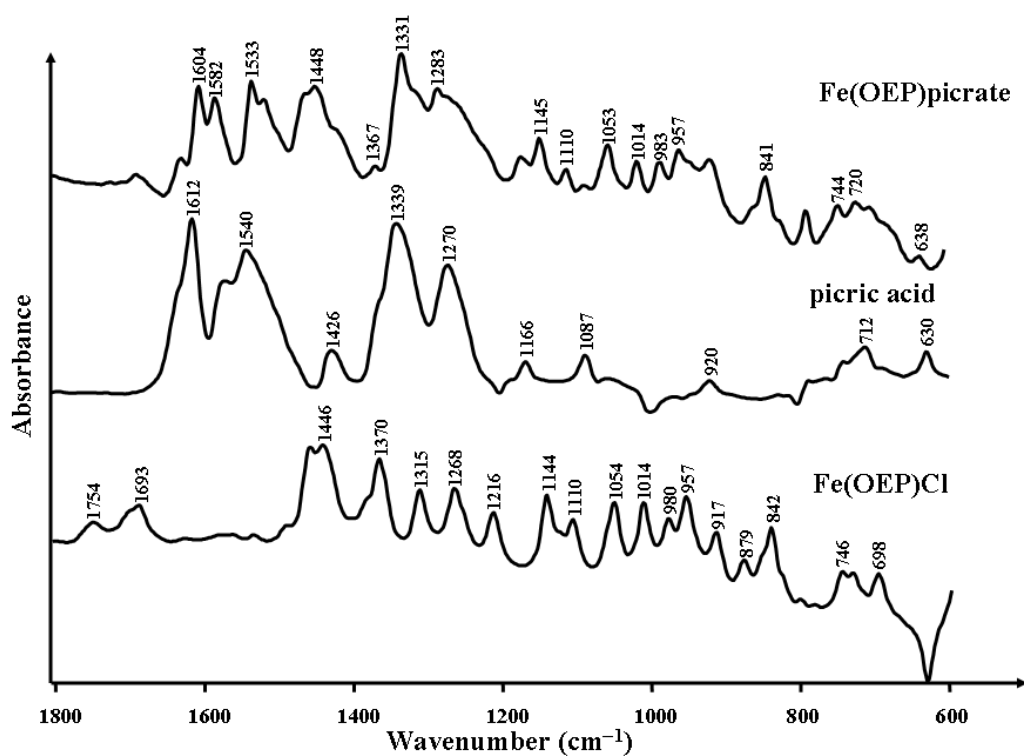
Figure 5.4 ATR/FTIR spectra.
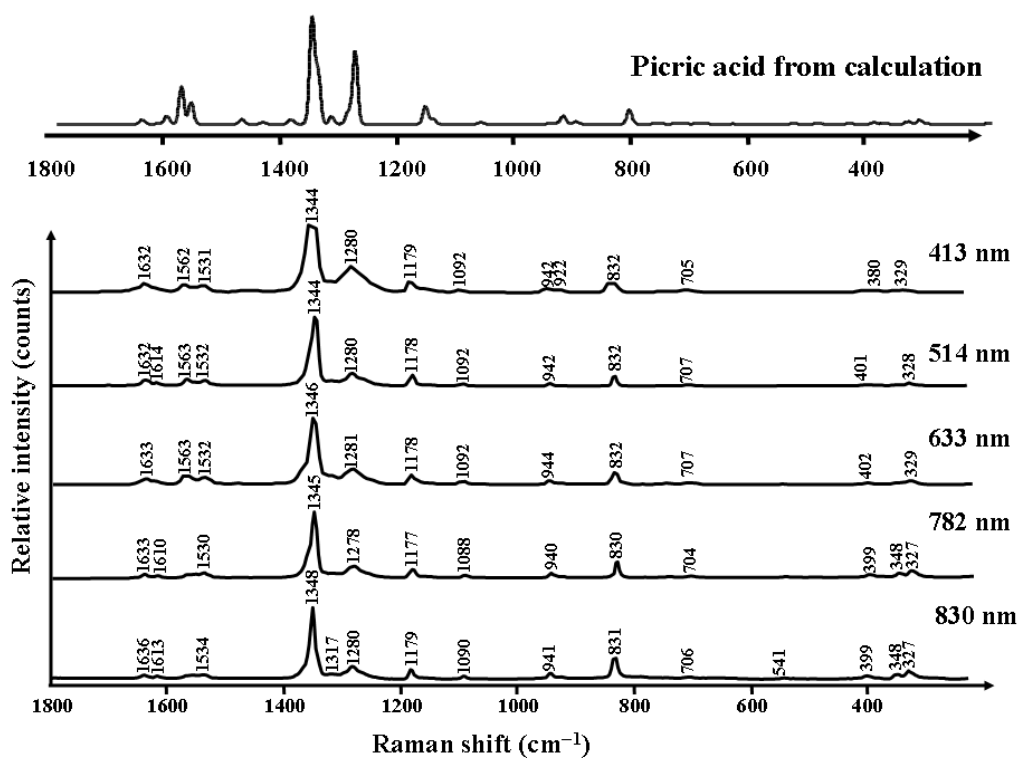
Figure 5.5 RR spectra of picric acid.
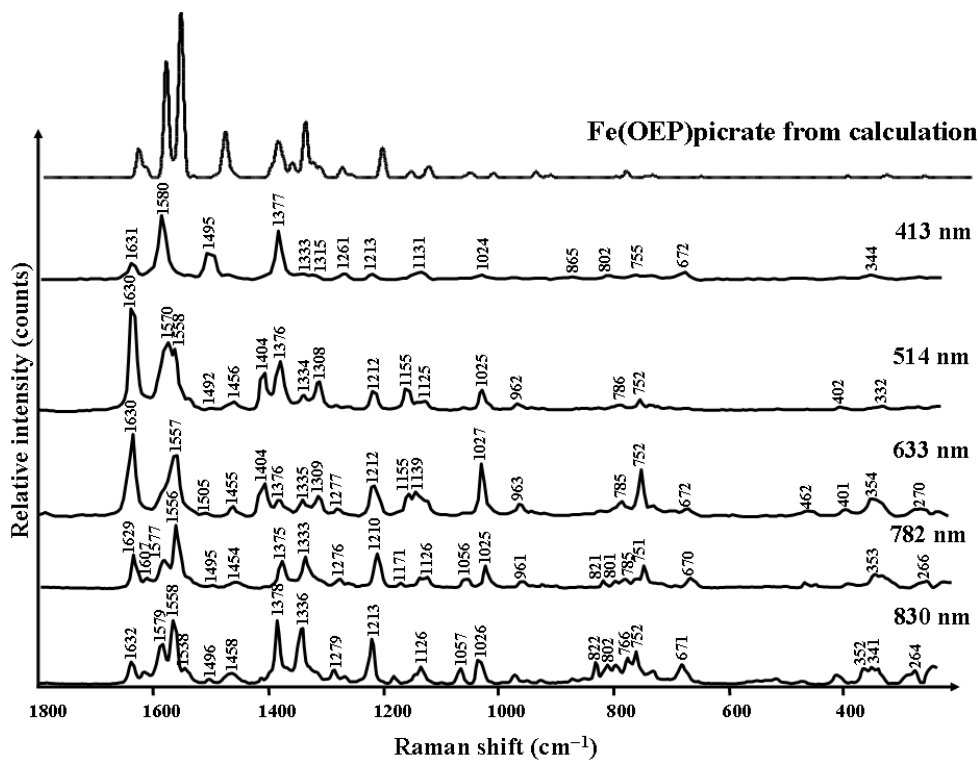
Figure 5.6 RR spectra of Fe(OEP)picrate.

(b) Assignment of the RR Spectra of Solid State Fe(OEP)picrate

Spin state marker band region (1300–1700 cm^{-1}). Figure 5.6 compares experimental RR spectra with a spectrum computed from the DFT calculations. Finite computational resources prevented direct calculation of the spectra for the Fe(OEP)picrate complex. Instead, the simulated spectrum was obtained by combining vibrations from two separate structures. Octaethylprophyrin vibrations were obtained from an Fe(OEP)Cl complex, computed using the crystal structure as a starting point. Picrate vibrational modes were derived from an Fe(porphyrin)picrate complex in which the C_{para}(picrate)–C_α(heme) distance was constrained to 4.42 Å, corresponding to the crystal structure. This compares to 5.71 in the optimised B3LYP/6-31G(d) structure. The computed spectra of the optimized and constrained structures are similar overall, though the constrained structure has slightly better agreement with experiment. Observed bands attributed to picrate ligand are listed in Table B2 (Appendix B), and compared to the corresponding computed ones. The pattern of spectral shifts between picric acid and the picrate complex confirms the assignments.

RR spectra and DFT calculated RR spectra (Table B3 and B4) of Fe(OEP)picrate in Figure 5.6 exhibits ν_{10} at ~1630 cm^{-1}. This wavenumber value is in agreement with the empirical correlation between the ν_{10} wavenumber value of Fe(OEP) derivatives and five-coordinated high-spin state complexes (Teraoka and Kitagawa 1980; Kitagawa and Ozaki, 1987). This is also the expected wavenumber value for a heme with a strong π acceptor axial ligand such as picrate bound to the Fe(III) (Teraoka and Kitagawa, 1980).

Oxidation state marker band region (1350–1400 cm^{-1}). The oxidation state marker band, ν_4 was observed at 1375 cm^{-1}, indicating that the oxidation state of iron

is iron(III) (Uno, Hatano, Nishimura, and Arata 1990). The ν_4 band is shifted from 1372 cm^{-1} in Fe(OEP)Cl to 1375 cm^{-1} in Fe(OEP)picrate due to the effect of retention of planar pyrrole units on the geometry of the 16-membered ring and the resulting induced vibrational frequency shifts (Spaulding, Chang, Yu, and Felton, 1975). Binding of the O atom of picrate as a π acceptor axial ligand to Fe competes with Fe $d_\pi \rightarrow$ porphyrin π^* back-bonding, thereby slightly increasing the wavenumber value of the ν_4 band (Spiro and Burke, 1976; Spiro and Czernuszewicz, 1995). It should be noted that not only is the ν_4 band sensitive to the back donation into porphyrin π^* and π-acid ligand orbitals of iron π electrons (Spiro and Burke, 1976), but it is also sensitive to the oxidation and spin state (Uno, Hatano, Nishimura, and Arata, 1990).

NO$_2$(picrate) stretching region. The Raman spectrum of Fe(OEP)picrate exhibits a band at 1607 and 1333 cm^{-1} in the region of ν_{as}(NO$_2$) and ν_s(NO$_2$) (Nakamoto, 1997), compared to the Raman wavenumber value of the NO$_2$ group of picric acid at 1614 and 1345 cm^{-1}, respectively. This indicates the N−O bond is weaker because of the hydrogen bond intramolecular interactions between C−H of substituent ethyl groups of Fe(OEP)picrate and oxygen atoms of nitro groups.

Low-wavenumber region (< 1200 cm^{-1}). It is interesting to note that the bands at 822, 802, and 751 cm^{-1} assigned to γ(CmH), ν(pyrrole breathing), and ν(pyrrole breathing), respectively of Fe(OEP)picrate show a similar enhancement profile and relative enhancement factors to β-hematin when compare to the same excitation laser (see RR spectra of β-hematin in Figure 3.7, Chapter III).

The RR bands of Fe(OEP)picrate at 610 and 266 cm^{-1} are assigned to the ν(Fe−OPh) and δ(Fe−OPh), respectively. The wavenumber value of ν(Fe−OPh) for Fe(OEP)picrate is shifted to higher wavenumber value than ν(Fe−OPh) of 607 cm^{-1} in Fe(OEP)OPh and ν(Fe−OMe) of 541 cm^{-1} in Fe(OEP)OMe (Uno, Hatano, Nishimura, and Arata, 1990),

The wavenumber value at 350 cm^{-1} which is assigned to ν(Fe−Cl) of Fe(OEP)Cl (Ivashin, Shula, Terekhov, and Dzilinski, 1996) is enhanced due to the charge-transfer transition from Cl to Fe(III) (Spiro, 1988). This band is strong in the spectrum of Fe(OEP)Cl but weak for Fe(OEP)picrate, and shifted to 401 cm^{-1}.

Relative Raman intensities. The Raman spectra of Fe(OEP)picrate shows a similar pattern of enhancement to β-hematin synthesized by the anhydrous dehydrohalogenation of hemin (Wood, Langford, Cooke, Lim, Glenister, Duriska, Unthank, and McNaughton, 2004) and extracted malaria pigment hemozoin (Frosch, Koncarevic, Zedler, Schmitt, Schenzel, Becker, and Popp, 2007) depending on the applied Raman excitation wavelength. Figure 5.7 displays the Raman intensity as a function of wavelength of Fe(OEP)picrate and β-hematin (see RR spectra of β-hematin in Figure 3.7, Chapter III) for the totally symmetric mode ν_2 and ν_4 normalized to ν_{10} (1623−1630 cm^{-1}) because this band appears intense at every excitation wavelength investigated. The ν_4 band is enhanced when exciting with 413 nm wavelength laser source but is weaker when excited with 514 nm. It also exhibits a much weaker intensity when applying 633 nm excitation. While the ν_4 band is stronger when using 633 nm excitation wavelength, it is even more dominant when applying the 782 nm laser source. It completely dominates the Raman spectrum when

the 830 nm excitation wavelength is applied. Not only Fe(OEP)picrate show a similar relative enhancement factor of totally symmetric mode A_{1g}, ν_4 assigned to 1370 cm^{-1}, but also it show a similar relative enhancement factor for nontotally symmetric mode B_{1g}, ν_{15} assigned to 750 cm^{-1}. The enhancement of Fe(OEP)picrate modes is very similar to that of β-hematin at all excitation wavelengths investigated.

The ν_4 band of Fe(OEP)picrate shows more enhancement than Fe(OEP)Cl because Fe(OEP)picrate contains π–π stacking between adjacent porphyrin cores. The porphyrin core is changed due to the retention of planar pyrrole units which affect the geometry of the 16-membered ring and induce vibrational frequency shifts (Spaulding, Chang, Yu, and Felton, 1975).

Structure Determination (Molecular Structure)

The molecular structure of Fe(OEP)picrate is displayed in Figure 5.2, which also gives the atom labels used for the structure determination of the Fe(OEP)picrate molecule as it exists in the crystal. A schematic diagram of the porphyrin core in Fe(OEP)(picrate) showing the displacements of the 25 atoms (in units of 0.01 Å) and the Fe−Np bond distances (in Å) is shown in Figure 5.8.

The four equatorial Fe−Np bonds show nonequivalent distances (2.040(2), 2.028(2), 2.055(2), and 2.053(2) Å) in the range of high-spin d^5 Fe(III) (Scheidt and Reed, 1981). The four equatorial Fe−Np bond lengths of Fe(OEP)picrate are shorter than the 2.074 Å of Fe(OEP)(OMe) (Hatano and Uno, 1990) and 2.061 Å of Fe(OEP)(OPh) (Kanamori, Yamada, Onoda, Okamura, Adachi, Yamamoto, and Ueyama, 2005), and show a rather large range of values when compared to the 2.050(1) Å high spin iron(III) in Fe(OEP)trichloroacetate (Neal, Cheng, Ma, Shelnutt,

Schulz, and Scheidt, 1999). The d[Fe–N3] and d[Fe–N4] are the largest distance due to they are effect by the π–π stacking intramolecular interaction between two *ortho*-NO$_2$ groups and pyrrole ring of N3 and N4, respectively rather than the streric hindrance between the porphyrin plane and axial ligand (Scheidt, Geiger, Lee, Reed, and Lang, 1985). The crystallography results supported the behavior with the wavenumber value of the ν_4 band increasing in Fe(OEP)picrate while the average Fe–N distance decreased to 2.044(4) Å in Fe(OEP)picrate from 2.071(2) Å in Fe(OEP)Cl (Senge, 2005).
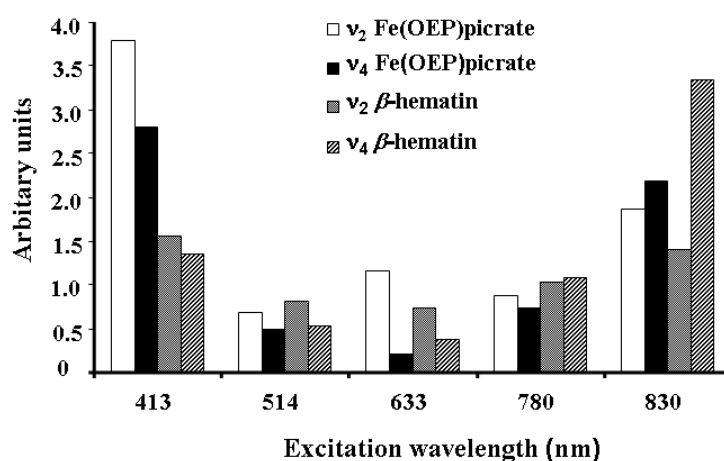
Figure 5.7 Raman intensity as a function of wavelength of Fe(OEP)picrate and β-hematin for the totally symmetric modes ν_2 and ν_4.

The Fe–O distance to the axial ligand is 1.928(2) Å. It is larger than the average 1.913 Å for Fe–O(OAr) found by structure correlation (Bürgi and Dunitz, 1994), 1.843(2) Å of Fe(OEP)(OMe) (Hatano and Uno, 1990), and 1.848(4) Å of Fe(OEP)(OPh) (Kanamori, Yamada, Onoda, Okamura, Adachi, Yamamoto, and Ueyama, 2005). The Fe–O distance is larger than expected due to the intramolecular

hydrogen bond decreases π donation of oxygen to iron (Ueyama, Nishikawa, Yamada, Okamura, Oka, Sakurai, and Nakamura, 1998; Kanamori, Yamada, Onoda, Okamura, Adachi, Yamamoto, and Ueyama, 2005) rather than the streric hindrance between the porphyrin plane and axial ligand (Scheidt, Geiger, Lee, Reed, and Lang, 1985). The d[Fe−O] in Fe(OEP)picrate is longer than in Fe−O(OPh). This corresponds to the wavenumber value of ν(Fe−OPh) for Fe(OEP)picrate is shifted to higher wavenumber value than in Fe(OEP)OPh and Fe(OEP)OMe (Uno, Hatano, Nishimura, and Arata, 1990). The crystallographic structure which shows the Fe−O distance is longer than expected because of the steric hindrance between the porphyrin plane and axial ligand (Scheidt, Geiger, Lee, Reed, and Lang, 1985) also hydrogen bond intramolecular interactions between C−H of substituent ethyl groups and oxygen atoms of nitro groups are evident.

Figure 5.8 Schematic diagram of the porphyrin core displaying the perpendicular displacements, in units of each atom from the mean plane of the core.

The Fe(OEP)picrate display of five ethyl groups up are influence by intramolecular hydrogen bond interactions for ethyl C52–H, C62–H, C82–H groups and intermolecular hydrogen bond interactions for ethyl C12–H also steric hindrance for ethyl C72–H and three ethyl groups down is also influenced by intermolecular interactions between the ethyl C–H groups and oxygen atoms of the axial ligand nitro groups. The distances and angles between the hydrogen donors and acceptors in Table B5 for intermolecular hydrogen bond interaction and Table B6 for intramolecular hydrogen bond interaction (Appendix B).

3.443(3) Å
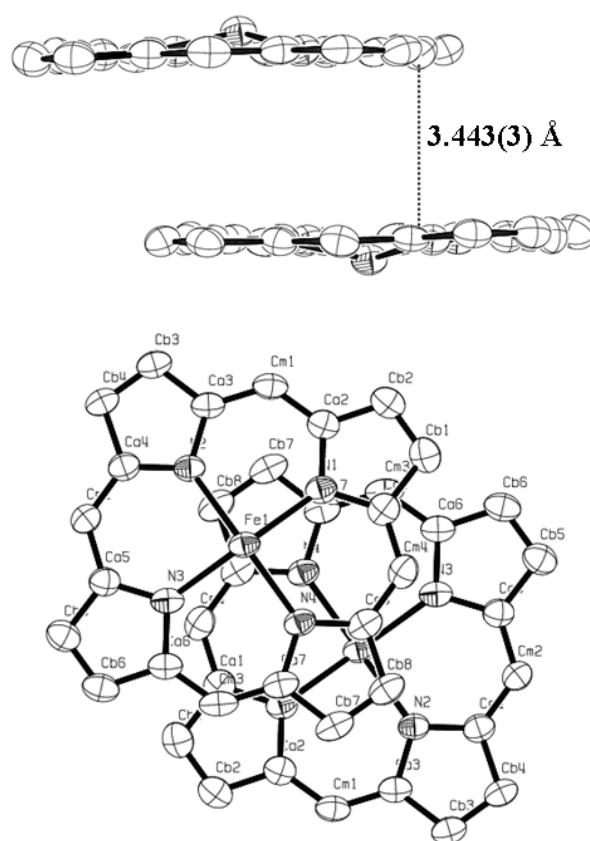
Figure 5.9 Diagram showing two inversion-related porphyrin cores. *ORTEP* projection diagram drawn, (top) perpendicular to the (vertical) Fe–O vector, and (bottom) perpendicular to the porphyrin planes.

Adjacent Fe(OEP)picrate molecules are related by an inversion center making the porphyrin planes parallel. The resulting π–π complex exhibits the parallel slipped configuration as shown in Figure 5.9 (top) with mean plane separation between the two porphyrin planes of 3.443(3) Å, and Fe$\cdots$Fe distance of 5.363(1) Å. Figure 5.9 (bottom) shows the molecule viewed perpendicular to the porphyrin planes displaying the parallel slipped π–π stacking between porphyrin planes of adjacent molecules.

Figure 5.10 shows picrate nitro–nitro packing interactions between adjacent molecules. Oxygen and nitrogen atoms from adjacent nitro groups exhibit reciprocal N$\cdots$O interactions with distances are 3.172(3) and 3.118(3) Å, which can be compared with the sum of van der Waals radii of 3.17 Å (Rowland and Taylor, 1996). The π–π stacking between benzene ring as axial ligand and porphyrin plane is absence. However the π–π stacking between two *ortho*-NO$_2$ groups and porphyrin plane would be the reason for the angles of twist of nitro groups from the phenyl ring increase 28.70(3)° and 27.21(2)° from 7.4° and 17.2° in picric acid (Duesler, Engelmann, David, Curtin, and Paul, 1978). The two *ortho*-NO$_2$ groups are coplanar with benzene ring as they are involved in the intramolecular hydrogen bond interaction.

Implications for Intermolecular Interaction of Fe(OEP)picrate in *β*-hematin

To predict the intermolecular interaction and crystal packing of *β*-hematin, we used the correlation of the enhancement of ν_4 band of Fe(OEP)picrate and *β*-hematin when applying near-IR excitation wavelengths including 782 and 830 nm. It was hypothesized that the enhancement of the totally symmetric mode at near-IR excitation wavelengths could in part be attributed to supramolecular interaction. This

implies that the study of crystal structures of malaria pigment models may be a very fruitful source of information on intermolecular interaction of β-hematin.

Fe(OEP)picrate shows a similar Raman enhancement profile to that of β-hematin, indicating the same chromophoric and electronic structure. Thus, it is hypothesized that the strength of supramolecular interaction of both compounds are similar.
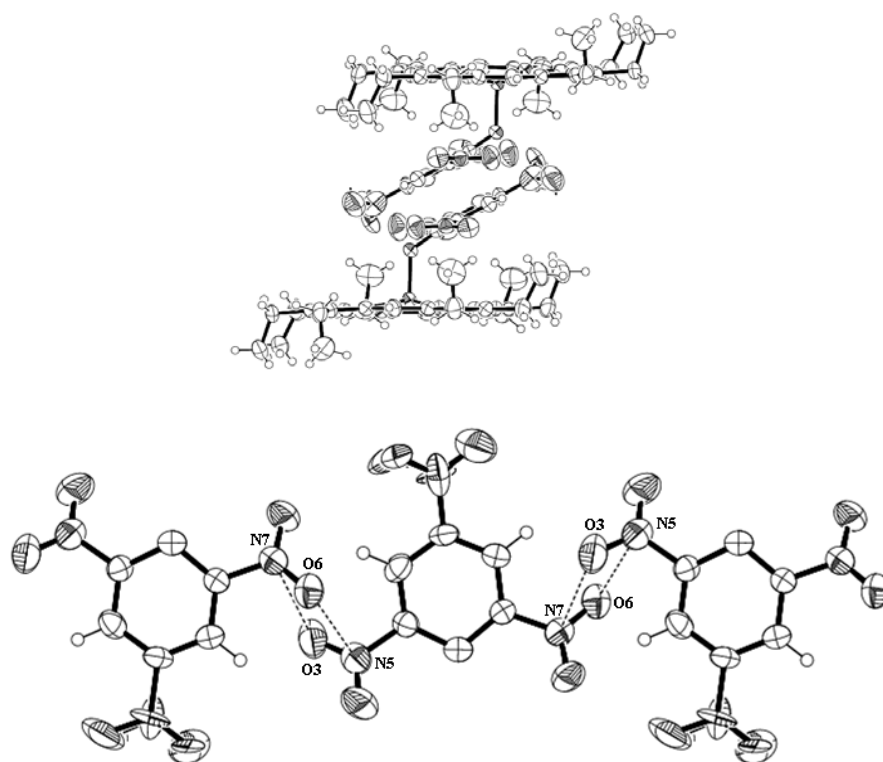
Figure 5.10 Diagram showing the interactions between adjacent inversion-related nitro groups. *ORTEP* projection diagrams drawn, (top) parallel to the plane of the picrate ligands, and (bottom) perpendicular to the picrate ligand plane.

Analysis of the crystal packing of Fe(OEP)picrate in Figure 5.11 shows a $\pi-\pi$ stacking between adjacent porphyrin cores is related by an inversion center with a

porphyrin to porphyrin contact. However, β-hematin does not show a $\pi-\pi$ stacking between reciprocal porphyrin cores because of the propionate linkage. The intermolecular distance between dimeric β-hematin is 3.6 Å (Figure 3.10, Chapter III) by *DIAMOND* (Crystal Impact, 2006) calculation.

The enhancement of the vibrational mode ν_4 in β-hematin when using near-IR laser excitation indicates β-hematin contains many more strong supramolecular interactions. This demonstrates that β-hematin contains strong hydrogen bonds to the propionate linkage. In this case not only the relative intensity of ν_4 may be an indicator of the strength of $\pi-\pi$ interactions (Webster, Tilley, Deed, McNaughton, and Wood, 2008) but also may be an indicator of the strength of supramolecular interactions.
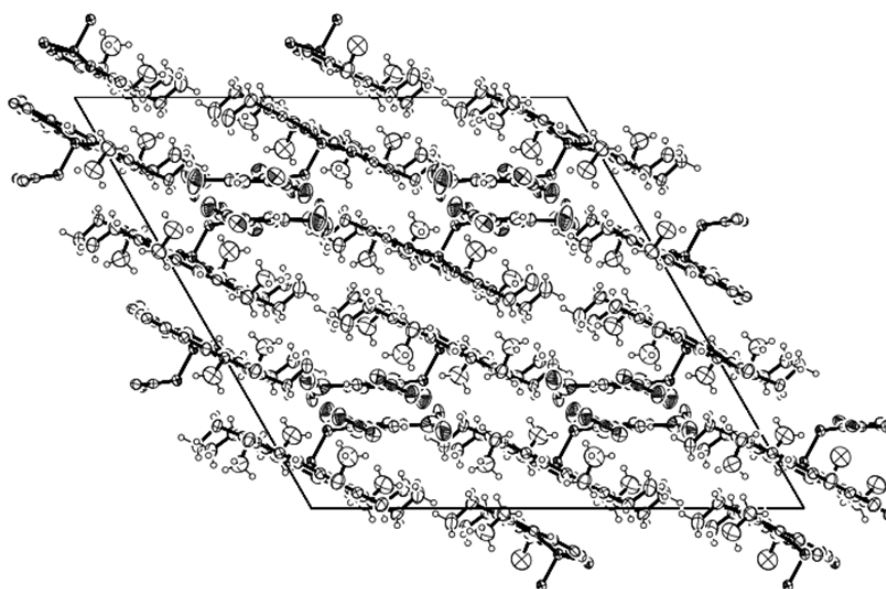
Figure 5.11 The crystal packing of Fe(OEP)picrate.

5.4 Conclusions

Fe(OEP)picrate was synthesized by the reaction of Fe(OEP)Cl and picric acid. The molecular structure information provided by RR spectroscopy correlates well with that from single crystal X-ray crystallographic analysis; both techniques verify Fe(OEP)picrate to be a five-coordinate high-spin iron(III) complex. Fe(OEP)picrate is a good model to understand the stereochemistry of β-hematin based on the similar enhancement of the vibrational mode v_4 and other bands that are also enhanced between 850-650 cm^{-1} when using near-IR excitation laser. The enhancement of the above mentioned modes are greater for β-hematin than Fe(OEP)picrate becasue β-hematin contains a closer intermolecular porphyrin ring because of the extensive hydrogen bonding in comparison to Fe(OEP)picrate. Accordingly, β-hematin does not dissolve in dichloromethane whereas Fe(OEP)picrate dissolves. It is therefore concluded that β-hematin contains much more stronger supramolecular interactions compared to Fe(OEP)picrate mainly because of the hydrogen bonded propionate linkage.

5.5 References

Abe, M., Kitagawa, T., Kyogoku, K. (1978). Resonance Raman spectra of octaethylporphyrinato-Ni(II) and meso-deuterated and ^{15}N substituted derivatives. II. A normal coordinate analysis. **J. Chem. Phys.** 69: 4526–4534.

Beurskens, P. T., Beurskens, G., Bosman, W. P., de Gelder, R., Granda, S., Gould, R. O., Israël, R., Smits, J. M. M. (1996). *DIRDIF-96: A Computer Program System for Crystal Structure Determination by Patterson Methods and Direct*

Methods Applied to Difference Structrue Factors, Tecnical Report of the Crystallography Laboratory, University of Nijimegen, Nijmegen, The Netherlands.

Blessing, R. H. (1997). Outlier treatment in data merging. **J. Appl. Cryst.** 30(4): 421−426.

Brennan, T. D., Scheidt, W. R., Shelnutt, J. A. (1988). New crystalline phase of (octaethylporphinato)nickel(II). Effects of π−π interactions on molecular structure and resonance Raman spectra. **J. Am. Chem. Soc.** 110(12): 3919−3924.

Bürgi, H. B., Dunitz, J. D. (1994). *Structure Correlation*. Vol. 2, VCH, pp. 817.

Burke, J. M., Kincaid, J. R., Peters, S., Gagne, R. R., Collman, J. P., Spiro, T. G. (1978). Structural-sensitive resonance Raman bands of tetraphenyl and "picket fence" porphyrin-iron complexes, including an oxyhemoglobin analogue. **J. Am. Chem. Soc.** 100(19): 6083−6088.

Burke, J. M., Kincaid, J. R., Spiro, T. G. (1978). Resonance Raman spectra and vibrational modes of iron(III) tetraphenylporphine μ-oxo dimer. Evidence for phenyl interaction and lack of dimer splitting. **J. Am. Chem. Soc.** 100(19): 6077−6083.

Burnett, M. N., Johnson, C. K. (1996). *ORTEP-III*: *Oak Ridge Thermal Ellipsoid Plot Program for Crystal Structure Illustrations*, Report ORNL-6895, Oak Ridge National Laboratory, Oak Ridge TN.

Callahan, P. M., Badcock, G. T. (1981). Insights into heme structure from Soret excitation Raman spectroscopy. **Biochem.** 20(4): 952−958.

Cheng, B., Hobbs, J. D., Debrunner, P. G., Erlebacher, J., Shelnutt, J. A., Scheidt, W. R. (1995). An unusual near-eclipsed porphyrin ring orientation in two crystalline forms of (μ-Oxo)bis[(octaethylporphinato)iron(III)]. Structural and molecular mechanics studies. **Inorg. Chem.** 34(1): 102−110.

Crystal Impact. (2006). *DIAMOND*. version 3.1. Crystal Impact GbR. Bonn, Germany.

Duesler, E. N., Engelmann, J. H., Curtin, D. Y., Paul, I. C. (1978). Picric acid. **Cryst. Struct. Comm.** 7: 449−453.

Duisenberg, A. J. M. (1992). Indexing in single-crystal diffractometry with an obstinate list of relections. **J. Appl. Cryst.** 25(2): 92−96.

Duisenberg, A. J. M., Kroon-Batenburg, L. M. J., Schreurs, A. M. M. (2003). An intensity evaluation method: *EVAL-14*. **J. Appl. Cryst.** 36: 220−229.

Ellison M. K., Scheidt W. R. (1999). Synthesis, molecular structures, and properties of six-coordinate [Fe(OEP)(L)(NO)]$^{+}$ derivatives: Elusive nitrosyl ferric porphyrins. **J. Am. Chem. Soc.** 121(22): 5210−5219.

Falk, J. E. (1964). **Porphyrins and metalloporphyrins**. Vol. 2, Elsevier.

Farrugia, L. J. (1997) *ORTEP*-3 for Windows- a version of *ORTEP*-III with a graphic user interface (GUI). **J. Appl. Cryst.** 30(1): 565.

Frisch, M. J., Trucks, G. W., Schlegel, H. B., Scuseria, G. E., Robb, M. A., Cheeseman, J. R., Montgomery, Jr., J. A., Vreven, T., Kudin, K. N., Burant, J. C., Millam, J. M., Iyengar, S. S., Tomasi, J., Barone, V., Mennucci, B., Cossi, M., Scalmani, G., Rega, N., Petersson, G. A., Nakatsuji, H., Hada, M., Ehara, M., Toyota, K., Fukuda, R., Hasegawa, J., Ishida, M., Nakajima, T., Honda, Y., Kitao, O., Nakai, H., Klene, M., Li, X., Knox, J. E., Hratchian, H. P., Cross, J.

B., Bakken, V., Adamo, C., Jaramillo, J., Gomperts, R., Stratmann, R. E., Yazyev, O., Austin, A. J., Cammi, R., Pomelli, C., Ochterski, J. W., Ayala, P. Y., Morokuma, K., Voth, G. A., Salvador, P., Dannenberg, J. J., Zakrzewski, V. G., Dapprich, S., Daniels, A. D., Strain, M. C., Farkas, O., Malick, D. K., Rabuck, A. D., Raghavachari, K., Foresman, J. B., Ortiz, J. V., Cui, Q., Baboul, A. G., Clifford, S., Cioslowski, J., Stefanov, B. B., Liu, G., Liashenko, A., Piskorz, P., Komaromi, I., Martin, R. L., Fox, D. J., Keith, T., Al-Laham, M. A., Peng, C. Y., Nanayakkara, A., Challacombe, M., Gill, P. M. W., Johnson, B., Chen, W., Wong, M. W., Gonzalez, C., and Pople, J. A. (2004). Gaussian 03, Revision E.01, Gaussian, Inc., Wallingford CT.

Frosch, T., Koncarevic, S., Zedler, L., Schmitt, M., Schenzel, K., Becker, K., Popp, J. (2007). In situ localization and structural analysis of the malaria pigment hemozoin. **J. Phys. Chem. B** 111(37): 11407−11056.

Fuchsman, W. H., Smith, Q. R., Stein, M. M. (1977). Direct Raman evidence for resonance interactions between the porphyrin ring system and ring-conjugated substituents in porphyrins, porphyrin dications, and metalloporphyrins. **J. Am. Chem. Soc.**, **99**(12): 4190−4192.

Galich, L.,; Hückstädt, H., Homborg, H. (1998). *J. Porphyrins Phthalocyanines.* 2: 79−87.

Hatano, K., Uno, T. (1990). Preparation and molecular structure of (methoxo) (octaethylporphinato)iron(III). **Bull. Chem. Soc. Jpn.** 63: 1825−1827.

Ivashin, N. V., Shula, A. M., Terekhov, S. N., Dzilinski, K. (1996). Physical and chemical transformations of μ-oxo dimers and alkoxy complexes of Fe-

octaethylporphyrins in solids and in solutions. **Spectrochim. Acta** Part A. 52: 1603−1614.

Kanamori, D., Yamada, Y., Onoda, A., Okamura, T., Adachi, S., Yamamoto, H., Ueyama, N. (2005). Structures and properties of octaethylporphinato (phenolate)iron(III) complexes with NH⋯O hydrogen bond modulation of Fe−O bond character by the hydrogen bond. **Inorg. Chim. Acta** 358: 331−338.

Kitagawa, T., Ozaki, Y. (1987). Recent advances in the sterochemistry of metalloporphyrins. **Struct. Bond.** 64: 73−114.

Lewis, M. L., Lewis, I. R., Griffiths, P.R. (2005). Evaluation of a dispersive Raman spectrometer with a Ge array detector and a 1064 nm laser for the study of explosives. **Vib. Spectrosc.** 38: 11−16.

Nakamoto, K. (1997). **Infrared and Raman spectra of inorganic and coordination compounds**; Part B: Applications in coordination, organometallic, and bioinorganic chemistry. 5th edition, Wiley, New York, pp. 322.

Neal, T. J., Cheng, B., Ma, J. G., Shelnutt, J. A., Schulz, C. E., Scheidt, W. R. (1999). Conformational diversity in (octaethylporphinato)(trichloroacetato)-iron(III) derivatives. **Inorg. Chim. Acta** 291(1−2): 49−59.

Nonius, B. V. (1998). *COLLECT*: *KappaCCD Software*, Nonius BV, Delft, The Netherlands.

Paulat, F., Praneeth, V. K. K., Näther, C., Lehnert, N. (2006). Quantum chemistry based analysis of the vibrational spectra of five-coordinate metalloporphyrins [M(TPP)Cl]. **Inorg. Chem.** 45(7): 2835−2856.

Puntharod, R., Haller, K. J. (2006). American Crystallographic Association Annual Meeting, Hawaii, Poster Presentation.

Rowland R. S., Taylor, R. (1996). Intermolecular nonbonded contact distances in organic crystal structures: Comparison with distances expected from van der Waals radii, **J. Phys. Chem.** 100(18): 7384−7391.

Scheidt, W. R., Geiger, D. K., Lee, Y. J., Reed, C. A., Lang, G. (1985). Characterization of five-coordinate mono(imidazole)(porphinato)iron(III) complexes. **J. Am. Chem. Soc.** 107(20): 5693−5699.

Scheidt, W. R., Reed, C. A. (1981). Spin-state/stereochemical relationships in iron porphyrins: Implications for the hemoproteins. **Chem. Rev.** 81(6): 543−555.

Scholler, D. M., Hoffman, B. M. (1979). Resonance Raman and electron paramagnetic resonance studied of the quaternary structure change in carp hemoglobin. Sensitivity of these spectroscopic probes to heme strain. **J. Am. Chem. Soc.** 101(7): 1655−1662.

Senge, M. O. (2005). Chloro(2,3,7,8,12,13,17,18-octaethylporphinato)iron(III). **Acta Cryst. E** 61: m399−m400.

Sheldrick, G. M. (1997). *SHELXL97*: *Program for Crystal Structure Refinement*. University of Göttingen, Göttingen, Germany.

Sheldrick, G. M. (2001). *SADABS*: *Multi-Scan Absorption Correction Program*. Version 2. University of Göttingen, Göttingen, Germany.

Slater, A. F. G., Swiggard, W. J., Orton, B. R. (1991). An iron-carboxylate bond links the heme units of malaria pigment. **Proc. Natl. Acad. Sci. USA** 88(2): 325−329.

Sparks, L. D., Scheidt, W. R., Shelnutt, J. A. (1992). Effects of $\pi-\pi$ interactions on molecular structure and resonance Raman spectra of crystalline copper(II) octaethylporphyrin. **Inorg. Chem.** 31(11): 2191−2196.

Spaulding, L. D., Chang, C. C., Yu, N., Felton, R. H. (1975). Resonance Raman spectra of metalloporphyrins. A structure probe of metal displacement. **J. Am. Chem. Soc.** 97(9): 2517−2525.

Spiro, T. G., Burke, J. M. (1976). Protein control of porphyrin comformation. Comparison of resonance Raman spectra of heme proteins with mesoporphyrin IX analogues. **J. Am. Chem. Soc.** 98(18): 5482−5489.

Spiro, T. G., Czernuszewicz, R. S. (1995). Resonance Raman spectroscopy of metalloproteins. **Methods Enzymol**. 246(18): 416−460.

Spiro, T.G., Li, X.-Y. (1988). In **Biological Applications of Raman Spectroscopy**. Spiro, T. G., Ed., Vol. 3, John Wiley & Sons, pp. 1−38.

Spiro, T. G., Stong, J. D., Stein, P. (1979). Porphyrin core expansion and doming in heme proteins. New evidence from resonance Raman spectra of six-coordinate high-spin iron(III) hemes. **J. Am. Chem. Soc.** 101(10): 2648−2655.

Spiro, T. G., Strekas, T. C. (1974). Resonance Raman spectra of heme proteins. Effects of oxidation and spin state. **J. Am. Chem. Soc.** 96(2): 338−345.

Teraoka, J., Kitagawa, T. (1980). Raman characterization of axial ligands for penta-hexacoordinate ferric high- and intermediate-spin (octaethylporphyrinato) iron(III) complexes. Elucidation of unusual resonance Raman spectra of cytochrome *C'*. **J. Phys. Chem.** 84: 1928−1935.

Ueyama, N., Nishikawa, N., Yamada, Y., Okamura, T., Oka, S., Sakurai, H., Nakamura, A. (1998). Synthesis and properties of octaethylporphinato (arenethiolato)iron(III) complexes with intramolecualr NH···S hydrogen bond: Chemical function of the hydrogen bond. **Inorg. Chem.** 37(10): 2415−2421.

Uno, T., Hatano, K., Nishimura, Y., Arata, Y. (1990). Spectrophotometric and resonance Raman studied on the formation of phenolate and thiolate complexes of (octaethylporphinato)iron(III). **Inorg. Chem.** 29(15): 2803−2807.

Wang, Y-W., Liu, W.-S., Tang, N., Tan, M.-Y., Yu, K.-B. (2003). Synthesis structural characterization of lanthanide picrate complexes with a new binaphthylamide. **J. Mol. Struct.** 660(1−3): 41−47.

Webster, G. T., Tilley, L., Deed, S., McNaughton, D., Wood, B. R. (2008). Resonance Raman spectroscopy can detect structural changes in haemozoin (malaria pigment) following incubation with chloroquine in infected erythrocytes. **FEBS Letters** 582(7): 1087−1092.

Wood, B. R., Langford, S. J., Cooke, B. M., Lim, J., Glenister, F. K., Duriska, M., Unthank, J. K., McNaughton, D. (2004). Resonance Raman spectroscopy reveals new insight into the electronic structure of β-hematin and malaria pigment. **J. Am. Chem. Soc.** 126(30): 9233−9239.

CHAPTER VI

SUMMARY AND CONCLUSION

Many researchers have studied malaria pigment using various techniques for more than a century, but the precise relationship between the structure and properties of malaria pigment remain somewhat elusive. β-hematin contains the same protoporphyrin IX heme group as malaria pigment and is indistinguishable by spectroscopic and X-ray powder diffraction techniques. β-hematin also shares the low solubility property with malaria pigment and crystallizes only as microcrystalline material that to date has resisted all attempts to recrystallize or Ostwald ripen into crystals suitable for a more definitive single crystal X-ray structural determination.

To circumvent the structural dilemma, the current work employs bioinorganic model systems based on the synthetic TPP and OEP heme complex systems. The model compounds studied all share several key features of malaria pigment (and of β-hematin) because they are all five-coordinate, square-pyramidal, high-spin, iron(III) porphyrin complexes. The spectral and physical properties are greatly influenced by the number and nature of axial ligands, the spin state and oxidation state of the iron which inturn influence the Fe−N bond distances, the Fe−axial ligand bond distances, and the stereochemistry of the heme, The model compounds investigated in this study have the common advantage in that all may be obtained in high-purity single crystal form suitable for single crystal X-ray structural characterization.

This study explores the correlation between solid state crystallographic structures and resonance Raman spectroscopic structures to study the mechanism of the near-IR resonance enhancement observed in malaria pigment samples.

The excitation profiles for Raman bands of selected malaria pigment model complexes were compared. The crystallographic data for a number of super facial molecular features are similar. However, only one of the five compounds studied namely [Fe(OEP)]$_2$O, does not show the enhancement of the totally symmetric modes at near-IR excitation demonstrating that the intramolecular spin-state, oxidation-state, and stereochemical features of the iron as well as that of the heme are not sufficient to explain the observed resonance enhancement pheonomenon. Moreover, π–π stacking between adjacent intermolecular porphyrin planes, or other aryl fragments, intramolecular delocalization between the phenyl and porphyrin π system, and the steric hindrance from the substituent groups are not sufficient to create the enhancement of the oxidation state marker band, ν_4 at near-IR excitation wavelengths.

Further, the solution phase resonance Raman spectra of the monomers and dimers Fe(TPP) and Fe(OEP) using near-IR excitation wavelengths at high laser power (20 mW) at high concentration (> 10 mM) showed no bands and only a broad baseline feature. The lack of resonance enhancement provides supporting evidence that the band enhancement observed when applying with near-IR excitation is a solid state phenomenon involving intermolecular interactions. One additional parameter was considered, which is the supramolecular chemistry of heme derivatives. These noncovalent supramolecular interactions were studied to investigate the mechanism of the enhancement. It was found that [Fe(OEP)]$_2$O exhibited the weakest hydrogen

bond interactions. It is hypothesized that the enhancement must therefore be, in a large part, attributed to noncovalent supramolecular interaction.

The enhancement of some of the A_{1g} modes in β-hematin was explained under this hypothesis. The enhancement of A_{1g} modes results from the excitonic coupling in the extended heme aggregate through strong intermolecular interaction. The summation of the concerted weaker intermolecular interactions between the porphyrin units appears to be the most important factor in explaining the enhancement of totally symmetric A_{1g} mode when applying with near-IR excitation wavelengths.

The enhancement of the A_{1g} modes in heme porphyrins at near-IR excitation could be interpreted in terms of the presence of intermolecular $C-H\cdots X$ hydrogen bonding where X is a π system or an electron donor atom. Consequently, the enhancement of ν_4 at near-IR excitation can be used as an indicator of the supramolecular interactions in heme aggregates. Moreover the relative intensity of ν_4 may be an indicator of the strength of concerted supramolecular interactions in heme systems. This is the first time that hydrogen bonds have been implicated in causing resonance Raman enhancement via the excitonic coupling mechanism. Excitonic coupling will essentially split the electronic states into a broad band of states with different geometries, energies, and oscillator strengths. The Raman intensities for a particular wavelength will then reflect the extent of the excitonic coupling. The net effect is that both Type A and Type B modes can become enhanced in these highly conjugate systems.

[Fe(TPP)]$_2$O, [Fe(OEP)]$_2$O, and Fe(OEP)picrate make excellent models to study the molecular and electronic structure of β-hematin because of the similar

stereochemistry with the iron coordinated to an oxygen atom from the axial ligand. However, the bands at 1627 and 751 cm^{-1} assigned to the $\nu(C_{\alpha}C_m)_{asym}$ and ν(pyr breathing), respectively, which are observed in β-hematin, disappeared in [Fe(TPP)]$_2$O. Furthermore, [Fe(OEP)]$_2$O does not exhibit the enhancement of oxidation state marker band, ν_4, unlike β-hematin. On the other hand, near-IR RR spectra of Fe(OEP)picrate do show bands at 1627 and 751 cm^{-1} and the dramatic enhancement of ν_4. Moreover Density Functional Theory calculations supported the band assignments and further clarified the experimental results. Therefore, Fe(OEP)picrate is an ideal model to understand the supramolecular interaction of β-hematin.

The enhancement of the vibrational mode ν_4 band in β-hematin is higher than Fe(OEP)picrate when exciting with near-IR excitation laser. The crystal structure of Fe(OEP)picrate shows $\pi-\pi$ stacking between adjacent porphyrin cores are related by an inversion center and another packing interaction between the adjacent molecule via NO−NO interaction. It is hypothesized that β-hematin has closer porphyrin rings in the aggregated array due to hydrogen bonds compared to Fe(OEP)picrate. Accordingly β-hematin does not dissolve in dichloromethane whereas Fe(OEP)picrate dissolved. It appears that β-hematin contains either many more supramolecular interactions. This work indicates that a major contributing factor to the greater enhancement of ν_4 in β-hematin compared to Fe(OEP)picrate is the hydrogen bonded propionate linkage.

A novel method was developed to synthesize β-hematin, namely the hydrothermal method in which entails acidification with glacial acetic acid at high

temperature. The product β-hematin could be verified by comparison with FTIR spectra of the products and β-hematin from the literature. Unfortunately, the size of the product crystals is not sufficient for single crystal X-ray structural characterization. More work is required to determine whether or not the hydrothermal method can be used to grow crystals of an adequate size for X-ray crystallography.

The study has important implications in the development of antimalarial drugs that are designed to disrupt hydrogen bond interaction in the hemozoin formation step. Moreover the discovery of the importance of hydrogen bonding interactions play in energy transfer in heme supramolecular aggregates may pave the way forward to the development of nano-wire heme based assemblies and other near-IR photon transfer sensors.

More experiments correlating RR and crystallography data on Fe(TMPP)Cl and [Fe(TMPP)]$_2$O (tetra(*para*-methoxyphenyl)porphyrin iron(III)) will help to strengthen the hypothesis that ν_4 is an indicator of either strong or concerted-weak intermolecular interactions in heme systems.

APPENDICES

APPENDIX A

SUPPORTING INFORMATION CHPATER IV

Table A1 Observed Raman Bands (cm^{-1}), Assignments, Local Coordinates, and Symmetry Modes for of Fe(TPP)Cl and [Fe(TPP)]$_2$O at 413, 514, 633, 782, and 830 nm.

Fe(TPP)Cl					[Fe(TPP)]₂O					assignment	symmetry term	local coordinate
413	514	633	782	830	413	514	633	782	830			
		1754										
		1725										
		1663										
		1617										
	1595		1597	1599	1599	1597		1597	1602	Φ_4	A_{1g}	ph, ν_{sym}(C–C)
	1571	1574		1575						Φ_4'	B_{2g}	ph, ν_{sym}(C–C)
1556	1553	1556	1552	1556	1555	1553	1556	1553	1557	ν_2	A_{1g}	ν(C$_\beta$C$_\beta$)
	1515	1518					1515			ν_{19}	A_{2g}	ν_{as}(C$_\alpha$C$_m$)
1496	1495	1496	1495	1497	1497	1495	1496			ν_{11}	B_{1g}	ν(C$_\beta$C$_\beta$)
								1464	1469	ν_{28}	B_{2g}	ν_{sym}(C$_\alpha$C$_m$)
1453		1453	1450	1452	1453	1462	1455			ν_3	A_{1g}	ν_{sym}(C$_\alpha$C$_m$)
1363	1362	1365	1362	1365	1362	1361	1361	1361	1365	ν_4	A_{1g}	ν_{sym}(pyr half-ring)
	1335	1335					1335			ν_{20}	A_{2g}	ν(pyr quarter-ring)
								1294	1299	ν_{12}	B_{1g}	ν_{sym}(pyr half-ring)
1273	1268	1271				1268					B_{1g}, B_{2g}	ν(C$_\alpha$–N)
1236	1235	1231	1232	1234	1239	1236	1237	1236	1239	ν_{26}	A_{2g}	ν_{as}(C$_\beta$–C1)
1182	1182	1183	1182	1174		1181	1183	1182	1183			
				1143								
1076	1074	1077	1073	1075	1078	1082	1079	1077	1078	ν_{17}	B_{1g}	δ_{sym}(C$_\beta$C1)
										ν_9	A_{1g}	δ_{sym}(C$_\beta$C1)
								1044		Φ_7'		ph in
			1029	1030						Φ_7	A_{1g}	ph, ν(C–C)
		1014				1015	1014	1017		ν_{30}	B_{2g}	ν_{asym}(pyr half-ring)
1009	1003		1004	1006	1005	1003			1006	ν_6	A_{1g}	ν(pyr breathing)
887	886	889	885	886	888	888	875	886		ν_7	A_{1g}	δ_{sym}(pyr def)
850						847	846	840	833	ν_{32}	B_{2g}	δ_{asym}(pyr def)
		832	833	833						ν_{24}	A_{2g}	δ_{asym}(pyr def)
				805						γ_5	A_{2u}	pyr fold sym
780	779									$2\nu_8$	A_{1g}	
				764								
724			723		722	723	727	726	727	γ_{26}	E_g	γ_{asym}(C$_\beta$C1)
									703	π_4''	E_u	ph ip
			666					666	666	Φ_9''	E_u	ph ip
	638	638	636	637	640	638			639	Φ_9	A_{1g}	ph ip
573	570		570	569	572					$\nu_8+\nu_{18}$	B_{1g}	ν(Fe–N)
								543		γ_{13}	B_{1u}	γ(C$_\alpha$C$_m$)
							497		501	π_5		ph ip
					394	389	392	392	394		A_{1g}	ν(Fe–O)
391	389	388	388	375								ν(Fe-Cl)
	366					366	365	366	366		A_{1g}	ν(Fe–O)
									324	γ_6	A_{2u}	pyr tilt
257	256	256	255	254				257	258	γ_{16}	B_{2u}	pyr tilt

Table A2 Observed Raman Bands (cm^{-1}), Assignments, Local Coordinates, and Symmetry Modes for of Fe(OEP)Cl and [Fe(OEP)]$_2$O at 413, 514, 633, 782, and 830 nm.

Fe(OEP)Cl					[Fe(OEP)]$_2$O					assignment	symmetry term	local coordinate
413	514	633	782	830	413	514	633	782	830			
				1725								
1632	1628	1630	1629	1631	1625	1624	1626	1624	1628	ν_{10}	B$_{1g}$	ν_{asym}(C$_\alpha$C$_m$)
1581			1582	1583	1588	1586		1586	1590	ν_2	A$_{1g}$	ν(C$_\beta$C$_\beta$)
	1563	1562	1560	1561	1567	1562	1563	1560	1565	ν_{19} ν_2 ν_{19}	A$_{2g}$ A$_{1g}$ A$_{2g}$	ν_{asym}(C$_\alpha$C$_m$) ν(C$_\beta$C$_\beta$) ν_{asym}(C$_\alpha$C$_m$)
1494				1495	1494	1492				ν_{11}	B$_{1g}$	ν(C$_\beta$C$_\beta$)
	1453	1454	1453	1454		1452	1452	1147	1453	ν_{28}	B$_{2g}$	ν_{sym}(C$_\alpha$C$_m$)
	1402	1404				1402	1403			ν_{29}	B$_{2g}$	ν(pyr quarter-ring)
1376	1372	1373	1375	1376	1378	1376	1374	1386	1388	ν_4	A$_{1g}$	ν(pyr half-ring)sym
1313	1308	1308	1312	1311	1313	1313	1314	1315	1317	ν_{21}	A$_{2g}$	δ(C$_m$H)
		1275	1275	1277			1274	1274	1276			ethyl
1262				1262	1263	1257				$\nu_5+\nu_9$	A$_{1g}$	δ_{sym}(C$_\beta$C1)
1213	1210	1211	1210	1211	1219	1210	1212	1210	1213	ν_{13}	B$_{1g}$	δ(C$_m$H)
	1155	1157				1160	1162			ν_{30}	B$_{2g}$	ν_{asym}(pyr half-ring)
1134	1134	1134	1136		1135	1135	1136	1135	1137	$\nu_6+\nu_8$	A$_{1g}$	ν_{sym}(C$_\alpha-$C$_\beta$) +
		1124		1127						ν_{22}	A$_{2g}$	ν_{asym}(pyr half-ring)
		1054	1054	1055	1055			1056	1059	ν_{23}	A$_{2g}$	ν_{asym}(C$_\beta$C1)
1024	1024	1026	1024	1026	1024	1023	1024	1023	1025	ν_5	A$_{1g}$	ν_{sym}(C$_\beta$C1)
959	962	962	961	962	964	960	960	959	960	$\nu_{32}+\nu_{35}$	A$_{1g}$	porph def+pyr transl
	873		874	875	887							ethyl
			800	801	804		803	802	804	ν_6	A$_{1g}$	ν(pyr breathing)
		779					782	781	783	ν_{32}	B$_{2g}$	δ_{asym}(pyr def)
			765	766	767				767	ν_{47}	E$_u$	ν(pyr breathing)
753	751	752	751	752		752	753	752	753	ν_{15}	B$_{1g}$	ν(pyr breathing)
				735	732					γ_5	A$_{2u}$	pyr fold sym
672			670	671	671	672	673	672	673	ν_7	A$_{1g}$	porph def
454		464	466	464	487							
					387	391		387	386		A$_{1g}$	ν(Fe–O)
353	350	345	353	352								ν(Fe–Cl)
					342	338	341	337	338			ν(Fe–O)
		280	281	278								ν(Fe–N)
						269	270	269	270			
244		251			252					γ_{23}	E$_g$	pyr tilt

Table A3 Assignment of the UV-visible Absorption Spectra of Fe(TPP)(Cl).

Experimental	Calculated	Assignment
369*	364	$p_x, p_y \rightarrow d_\pi$, $a_{2u} \rightarrow d_\pi$, $b_{2u} \rightarrow d_\pi^*$
378 st	375, 382	$b_{2u} \rightarrow d_z^2$, ($a_{2u} \rightarrow d_\pi$, $b_{2u} \rightarrow d_\pi^*$)
397*	392	$b_{2u} \rightarrow d_\pi$, $b_{2u} \rightarrow d_\pi^*$
416 vst	409, 411	B ($\pi \rightarrow \pi^*$), $b_{2u} \rightarrow d_\pi$
430*?	429, 439	$b_{2u} \rightarrow d_\pi$, B ($\pi \rightarrow \pi^*$)
511 st	523	Q_v ($\pi \rightarrow \pi^*$)
573	577	Q_0 ($\pi \rightarrow \pi^*$), $a_{1u}(\pi) \rightarrow d_\pi$
608* w	628	$a_{2u}(\pi) \rightarrow d_z^2$
648, 665	685, 706	$a_{1u}(\pi) \rightarrow d_\pi$, $a_{2u}(\pi) \rightarrow \pi^*$
691, 707	747, 763	$a_{1u}(\pi) \rightarrow d_\pi$, $a_{2u}(\pi) \rightarrow \pi^*$
875* br	890, 928	$a_{2u} \rightarrow d_\pi$

Table A4 Supramolecular Interactions of Fe(TPP)Cl.

D–H···A	D–H (Å)	H···A (Å)	D···A (Å)	<D–H···A>	Type of interaction
C15_ii–H7_ii···Cl	0.948	2.953	3.826	153.68	C–H···Cl
C42_i–H26_i···Cl	0.945	3.040	3.734	131.60	C–H···Cl
C24_iv–H11_iv···Cl	0.951	3.146	3.773	125.02	C–H···Cl
C40_ii–H24_ii···(N1–C2)	0.950	2.802	3.660	150.79	C–H···π
C40_ii–H24_ii···N1	0.950	2.926	3.825	158.32	C–H···π
C41_ii–H25_ii···(N2–C3)	0.953	2.725	3.492	138.12	C–H···π
C41_ii–H25_ii···(N2–C4)	0.953	2.847	3.760	160.77	C–H···π
C41_ii–H25_ii···N2	0.953	2.791	3.635	148.13	C–H···π
C41_ii–H25_ii···(C3–C11)	0.953	2.921	3.586	127.95	C–H···π
C31_iii–H17_iii···(N4–C7)	0.950	2.750	3.550	142.45	C–H···π
C31_iii–H17_iii···N4	0.950	3.002	3.759	137.61	C–H···π
C31_iii–H17_iii···(C7–C15)	0.950	2.668	3.561	156.88	C–H···π
C31_iii–H17_iii···(C15–C16)	0.950	2.984	3.933	178.01	C–H···π
C9_iii–H1_iii···(C30–C31)	0.945	2.887	3.497	121.85	C–H···π

Table A5 Supramolecular Interactions of [Fe(TPP)]₂O.

D–H···A	D–H (Å)	H···A (Å)	D···A (Å)	<D–H···A>	Type of interaction
C43f_i–H27f_i···N1	0.964	2.943	3.578	124.54	C–H···π
C43f_i–H27f_i···(N1–C4)	0.964	2.982	3.455	111.59	C–H···π
C44f_i–H28f_i···N2	0.970	2.870	3.318	109.21	C–H···π
C44f_i–H28f_i···(N2–C9)	0.970	2.786	3.362	118.79	C–H···π
C31f_ii–H17f_ii···N3	0.971	3.085	3.846	136.21	C–H···π

Table A5 (Continued)

D–H···A	D–H (Å)	H···A (Å)	D···A (Å)	<D–H···A>	Type of interaction
C31f_ii–H17f_ii···(N3–C14)	0.971	2.894	3.755	148.37	C–H···π
C32f_i–H18f_i···(N4–C16)	0.979	2.986	3.555	118.19	C–H···π
C32f_i–H18f_i···N4	0.979	3.118	3.590	111.25	C–H···π
C32f_i–H18f_i···(C16–C17)	0.979	2.970	3.754	137.90	C–H···π
C29f_ii–H15f_i···(C41–C42)	0.959	2.832	3.686	148.93	C–H···π
C26f_i–H13f_i···(C40–C41)	0.955	2.816	3.757	168.80	C–H···π
C26f_i–H13f_i···(C41–C42)	0.955	2.851	3.711	150.40	C–H···π
C43_i–H27_i···N1f	0.964	2.943	3.578	124.54	C–H···π
C43_i–H27_i···(N1f–C4f)	0.964	2.982	3.455	111.59	C–H···π
C44_i–H28_i···N2f	0.970	2.870	3.318	109.21	C–H···π
C44_i–H28_i···(N2f–C9f)	0.970	2.786	3.362	118.79	C–H···π
C31_ii–H17_ii···N3f	0.971	3.085	3.846	136.21	C–H···π
C31_ii–H17_ii···(N3f–C14f)	0.971	2.894	3.755	148.37	C–H···π
C32_i–H18_i···(N4f–C16f)	0.979	2.986	3.555	118.19	C–H···π
C32_i–H18_i···N4f	0.979	3.118	3.590	111.25	C–H···π
C32_i–H18_i···(C16f–C17f)	0.979	2.970	3.754	137.90	C–H···π
C29_iii–H15_iii···(C41f–C42f)	0.959	2.832	3.686	148.93	C–H···π
C26_ii–H13_ii···(C40f–C41f)	0.955	2.816	3.757	168.80	C–H···π
C26_ii–H13_ii···(C41f–C42f)	0.955	2.851	3.711	150.40	C–H···π

Table A6 Supramolecular Interactions of Fe(OEP)Cl.

D–H···A	D–H (Å)	H···A (Å)	D···A (Å)	<D–H···A>	Type of interaction
C33_i–H39_i···Cl	0.990	2.864	3.664	138.43	C–H···Cl
C13_ii–H15_ii···Cl	0.981	2.887	3.706	141.62	C–H···Cl
C24_iv–H28_iv···Cl	0.991	3.108	3.657	116.34	C–H···Cl
C3_i–H2_i···Cl	0.989	2.979	3.790	139.88	C–H···Cl
C33_iii–H39_iii···(N1–C1)	0.990	2.786	3.593	139.14	C–H···π
C33_iii–H39_iii···N1	0.990	2.849	3.701	144.76	C–H···π
C33_iii–H39_iii···(N1–C8)	0.990	2.880	3.623	132.53	C–H···π
C33_iii–H39_iii···(C1–C2)	0.990	2.963	3.530	117.42	C–H···π
C12_ii–H13_ii···(N3–C19)	0.990	2.968	3.622	124.49	C–H···π
C12_ii–H13_ii···N3	0.990	3.116	3.898	136.82	C–H···π
C12_ii–H13_ii···(C19–C20)	0.990	2.904	3.347	108.10	C–H···π
C12_ii–H13_ii···(C20–C23)	0.990	2.995	3.512	113.64	C–H···π
C3_ii–H2_ii···(N4–C28)	0.989	2.979	3.820	143.45	C–H···π
C3_ii–H2_ii···N4	0.989	3.075	3.986	153.62	C–H···π
C3_ii–H2_ii···(C28–C29)	0.989	2.998	3.610	121.08	C–H···π

Table A7 Supramolecular Interactions of Triclinic [Fe(OEP)]$_2$O.

D–H···A	D–H (Å)	H···A (Å)	D···A (Å)	<D–H···A>	Type of interaction
C53_i–H34_i···(N1–C1)	0.949	2.886	3.576	130.54	C–H···π
C53_i–H34_i···N1	0.949	2.979	3.757	140.16	C–H···π
C66_i–H69_i···N3	0.948	3.032	3.349	101.25	C–H···π
C66_i–H70_i···(N3–C5)	0.949	2.938	3.377	109.59	C–H···π
C66_i–H70_i···N3	0.949	3.047	3.349	100.27	C–H···π
C41_i–H10_i···N7	0.949	3.197	3.741	118.23	C–H···π

Table A8 Supramolecular Interactions of Monoclinic [Fe(OEP)]$_2$O.

D–H···A	D–H (Å)	H···A (Å)	D···A (Å)	<D–H···A>	Type of interaction
C62_i–H16_i···(N1–C1)	0.949	2.999	3.561	119.32	C–H···π
C62_i–H16_i···N1	0.949	3.096	3.524	109.21	C–H···π
C57_i–H88_i···N3	0.946	2.997	3.599	122.81	C–H···π
C53_i–H80_i···N5	0.945	3.106	3.932	146.82	C–H···π
C53_i–H80_i···(N5–C10)	0.945	2.958	3.704	136.75	C–H···π
C50_i–H73_i···N7	0.948	3.161	3.671	115.53	C–H···π

Table A9 Supramolecular Interactions of β-hematin.

D–H···A	D–H (Å)	H···A (Å)	D···A (Å)	<D–H···A>	Type of interaction
C19_i–H···O36			3.949		C–H···O
C31_i–H···O36			3.778		C–H···O
C33_i–H···O36			3.959		C–H···O
O36–H···O37_iii			2.830		O–H···O
O36–H···O40_i			3.802		O–H···O
C31–H···O37			3.214		C–H···O
C30_i–H···O40			3.207		C–H···O
C38_i–H···O40			3.191		C–H···O
C13_i–H···O40			3.667		C–H···O
C18_ii–H···O40			3.651		C–H···O
C19_ii–H···O40			3.543		C–H···O
C21_ii–H···O40			3.973		C–H···O
C29_i–H···O40			3.884		C–H···O
C34_i–H···O40			3.146		C–H···O
C35_i–H···O40			3.733		C–H···O
C13_i–H···O41			3.841		C–H···O

Table A9 (Continued)

D–H···A	D–H (Å)	H···A (Å)	D···A (Å)	<D–H···A>	Type of interaction
C29_i–H···O41			3.464		C–H···O
C30_i–H···O41			3.570		C–H···O
C34_i–H···O41			3.592		C–H···O
C29–H···(N2–C6)			3.252		C–H···π
C29–H···(N2–C3)			3.450		C–H···π
C29–H···N2			3.418		C–H···π
C29–H···(C3–C4)			3.532		C–H···π
C29–H···(C4–C5)			3.413		C–H···π
C29–H···(C5–C6)			3.210		C–H···π
C30_iii–H···(N20–C21)			3.349		C–H···π
C30_iii–H···(N20–C24)			3.574		C–H···π
C30_iii–H···N20			3.566		C–H···π
C30_iii–H···(C21–C22)			3.207		C–H···π
C30_iii–H···(C22–C23)			3.388		C–H···π
C30_iii–H···(C23–C24)			3.583		C–H···π
C43_i–H···(N20–C21)			3.477		C–H···π
C43_i–H···(N20–C24)			3.615		C–H···π
C43_i–H···N20			3.690		C–H···π
C43_i–H···(C21–C22)			3.201		C–H···π
C43_i–H···(C22–C23)			3.177		C–H···π
C43_i–H···(C23–C24)			3.430		C–H···π
C4_i–H···(N20–C24)			3.616		C–H···π
C4_i–H···N20			3.823		C–H···π
C4_i–H···(C23–C24)			3.817		C–H···π
C26_i–H···(N20–C21)			3.806		C–H···π
C26_i–H···(N20–C24)			3.571		C–H···π
C26_i–H···N20			3.482		C–H···π
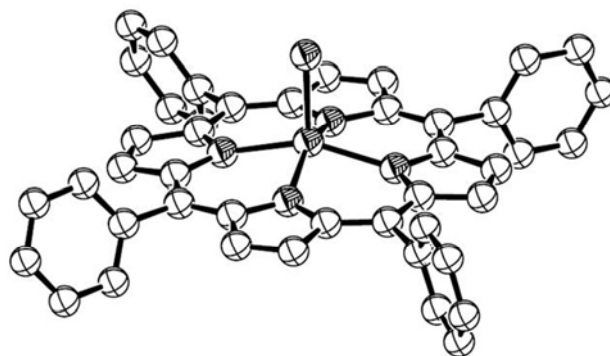
Figure A1 Perspective diagram of the molecular structure of Fe(TPP)Cl.
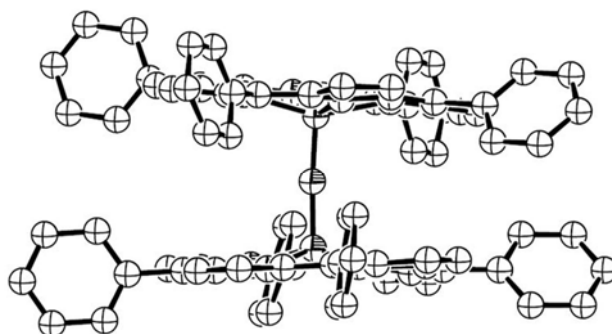
Figure A2 Perspective diagram of the molecular structure of [Fe(TPP)]$_2$O.
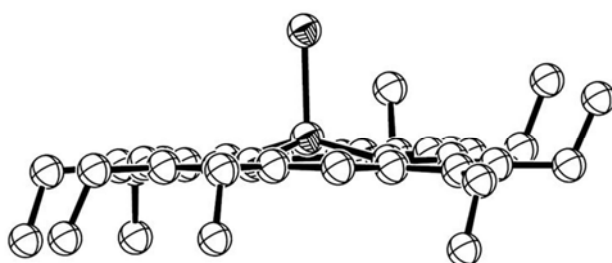
Figure A3 Perspective diagram of the molecular structure of Fe(OEP)Cl.
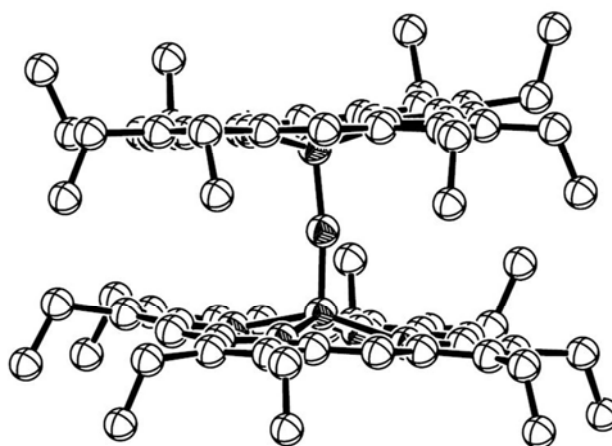
Figure A4 Perspective diagram of the molecular structure of triclinic [Fe(OEP)]$_2$O.
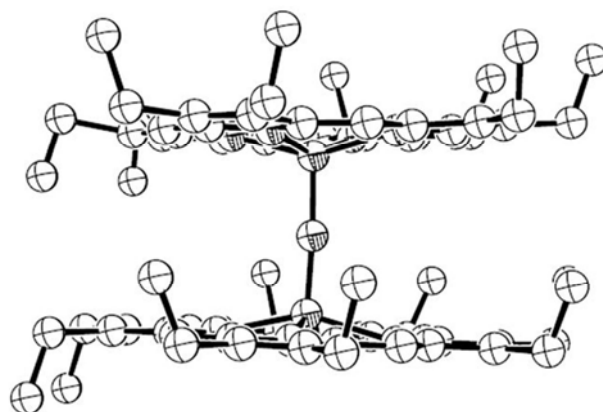
Figure A5 Perspective diagram of the molecular structure of monoclinic [Fe(OEP)]$_2$O.
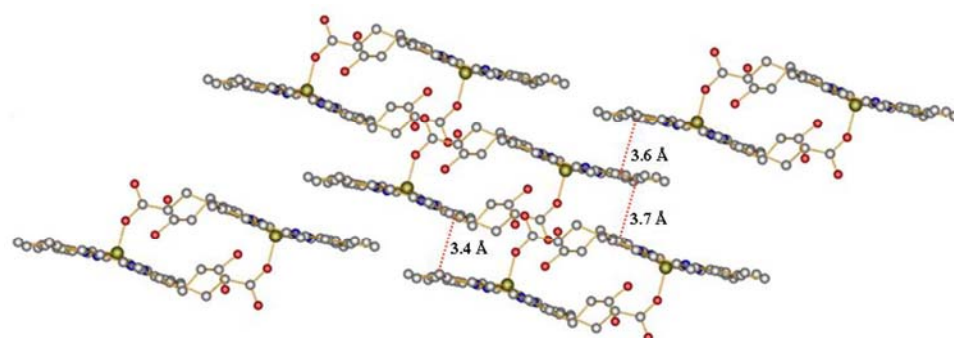
Figure A6 β-hematin molecules in the crystal structure showing the closest porphyrin plane to porphyrin plane contact distances.

APPENDIX B

SUPPORTING INFORMATION CHPATER V

Table B1 Observed Raman bands (cm^{-1}), Assignments, Symmetry Terms, and Local Coordinates for Picric Acid at 413, 514, 633, 782, and 830 nm Excitation.

Picric acid					local coordinate
413	**514**	**633**	**782**	**830**	
1632	1632	1633	1633	1636	CC ring str
	1614		1610	1613	ν(NO)$_2$asym
1562	1563	1563			
1531	1532	1532	1530	1534	
1344	1344	1346	1345	1348	ν(NO)$_2$sym
1280	1280	1281	1278	1280	ν(NO)$_2$sym
1179	1178	1178	1177	1179	sym CN str
1092	1092	1092	1088	1090	
942	942	944	940	941	
832	832	832	830	831	δ(NO)$_2$ in-plane (scissoring)

Table B2 Calculated Raman Bands (cm^{-1}) for Selected Vibrational Modes of Picric Acid at 2 Levels: B3LYP/6-311+G*.

Band position/cm^{-1} a scale	IR int/ km mol^{-1}	Raman activity/A^{4}u^{-1}	Band assignment
768.6	43.8	2.1	HO out of plane def
814.6	0.3	22.8	in plane ring def + d (ONO) sym
812.2	2.3	3.8	d (ONO) para (+ in plane ring def)
906.2	64.9	5.0	ortho CN antisym str
927.7	31.9	15.7	para CN str (+ other 2)
940.5	17.5	1.1	CH out of plane (sym)
948.8	0.8	2.1	CH out of plane (anti)
1068.5	88.0	3.0	CH in plane bend (clap)
1150.5	44.2	9.7	CH&OH in plane bend (clock)
1163.4	16.7	33.3	sym CN str (all 3)
1283.9	157.7	139.9	NO$_2$ str (H-bonded ortho) + OH & CH bends
1295.7	102.1	22.7	OH & CH bends

Table B3 Observed Raman Bands (cm^{-1}), Assignments, Symmetry Terms, and Local Coordinates for Fe(OEP)picrate at 413, 514, 633, 782, and 830 nm Excitation.

Fe(OEP)picrate					assignment	symmetry	local coordinate
413	514	633	782	830			
1631	1630	1626	1629	1632	ν_{10}	B_{1g}	$\nu(C_\alpha C_m)_{asym}$
			1607	1609			ring CC str (pic)
			1607	1609			$\nu(NO)_{2asym}$
1580			1577	1579	ν_2	A_{1g}	$\nu(C_\beta C_\beta)$
	1570				ν_{19}	A_{2g}	$\nu(C_\alpha C_m)_{asym}$
	1558	1558	1556	1558	ν_{11}	B_{1g}	$\nu(C_\beta C_\beta)$
1495	1492		1495	1496	ν_3	A_{1g}	$\nu(C_\alpha C_m)_{sym}$
	1456	1453	1454	1458	ν_{28}	B_{2g}	$\nu(C_\alpha C_m)_{sym}$
	1404	1402			ν_{29}	B_{2g}	ν(pyr quarter-ring)
					ν_{20}	A_{2g}	ν(pyr quarter-ring)
1377	1376	1376	1375	1378	ν_4	A_{1g}	ν(pyr half-ring)$_{sym}$
1333	1334	1335	1333	1336			$\nu(NO)_{2sym}$
1315	1308	1311			ν_{21}	A_{2g}	$\delta(C_mH)$
		1274	1276	1279			ethyl
1261				1261	$\nu_5+\nu_9$	A_{1g}	$\delta(C_\beta C1)_{sym}$
1213	1212	1211	1210	1213	ν_{13}	B_{1g}	$\delta(C_mH)$
			1171	1173			sym CN str (pic)
	1155	1154			ν_{30}	B_{2g}	ν(pyr half-ring)$_{asym}$
1131		1135			$\nu_6+\nu_8$	A_{1g}	$\nu(C_\alpha-C_\beta)_{sym} + \nu(Fe-N)$
	1125		1126	1126	ν_{22}	A_{2g}	ν(pyr half-ring)$_{asym}$
		1054	1057	1057	ν_{23}	A_{2g}	$\nu(C_\beta C1)_{asym}$
1024	1025	1024	1025	1026	ν_5	A_{1g}	$\nu(C_\beta C1)_{sym}$
	962	962	961	963	$\nu_{32}+\nu_{35}$	A_{1g}	δ(porph def) + δ(pyr transl)
869		861					ethyl
				822			$\delta(ONO)_{sym}$ (pic)
802		799	801	802	ν_6	A_{1g}	ν(pyr breathing)
	786	783	785	787	ν_{32}	B_{2g}	δ(pyr def)$_{asym}$
				766	ν_{47}	E_u	ν(pyr breathing)
755	752	752	751	752	ν_{15}	B_{1g}	ν(pyr breathing)
				722			
672	672	673	671	671	ν_7	A_{1g}	δ(pyr def)$_{sym}$
				507			
			474				
461		464		464			δ(pyr fold)?
			456				
398	40	400	400	400			$\nu(Fe-O)$
			353	352			
344		345		341			
	332			329			$\nu(Fe-N)$
		268(1)	266(1)	264(2)			?

Table B4 Calculated Raman Bands (cm^{-1}) for Fe(OEP)picrate Performing a B3LYP/6-31+G*.

Band position (cm^{-1})	Band assignment
411.8	Fe–O str
831.9	d (ONO) sym
933.6	ortho CN antisym str
963.7	CH out of plane (s) + para CN
956.8	CH out of plane (sym)
961.4	CH out of plane (anti)
1106.7	CH in plane bend (clap)
1204.4	CH in plane wag
1199.7	sym CN str (all 3)
1339.4	kekule ring str?
1367.0	CO str & CH in plane clap
1385.4	NO str (para mosty)
1392.0	NO str (antisym ortho)
1404.6	NO str (all 3 sym) + haem
1401.9	CH in plane clap + haem
1521.3	CO str & CH in plane clap

Table B5 The Intermolecular Hydrogen Bond Interactions in Fe(OEP)picrate Monoclinic *C2/c*.

D–H···A	D–H (Å)	H···A (Å)	D···A (Å)	<D–H···A>	Type of interaction
C31_i–H31b_i···O1	0.970	3.025	3.766	134.19	C–H···O
C21_i–H21a_i···O2	0.970	3.074	3.662	120.37	C–H···O
C22_i–H22b_i···O2	0.960	2.761	3.408	125.37	C–H···O
C5_i–H5_i···O3	0.930	3.005	3.416	108.55	C–H···O
C31_i–H31a_i···O4a	0.970	2.683	3.477	139.44	C–H···O
C41_i–H41a_i···O4a	0.970	2.452	3.252	139.70	C–H···O
C42_i–H42a_i···O4a	0.960	3.105	3.357	96.78	C–H···O
C42_i–H42b_i···O4a	0.960	3.193	3.357	91.42	C–H···O
C12_iii–H12a_iii···O5a	0.960	2.702	3.278	112.34	C–H···O
C42_i–H42b_i···O5a	0.960	2.814	3.539	133.00	C–H···O
C21_ii–H21b_ii···O5a	0.970	3.104	3.745	127.34	C–H···O
C22_ii–H22b_ii···O5a	0.960	3.022	3.528	114.10	C–H···O
C3_i–H3_i···O6	0.930	2.903	3.333	109.66	C–H···O
C3_i–H3_i···O7	0.930	2.587	3.416	148.76	C–H···O
C31_ii–H31a_ii···O7	0.970	2.863	3.325	110.20	C–H···O
C32_ii–H32b_ii···O7	0.960	2.603	3.340	133.82	C–H···O

Table B5 (Continued)

D–H···A	D–H (Å)	H···A (Å)	D···A (Å)	\<D–H···A\>	Type of interaction
C81_i–H81b_i···(N2–Ca4)	0.970	2.860	3.476	122.24	C–H···π
C81_i–H81b_i···N2	0.970	3.033	3.604	118.98	C–H···N
C81_i–H81b_i···(Ca4–Cb4)	0.970	2.853	3.626	137.24	C–H···π
C31_ii–H31b_ii···(N2–Ca3)	0.970	2.934	3.622	128.89	C–H···π
C31_ii–H31b_ii···N2	0.970	3.066	3.740	127.86	C–H···N

Table B6 The Intramolecular Hydrogen Bond Interactions in Fe(OEP)picrate

Monoclinic *C2/c*

D–H···A	D–H (Å)	H···A (Å)	D···A (Å)	\<D–H···A\>	Type of interaction
C82–H82a···O3	0.960	2.612	3.513	156.54	C–H···O
C5–H5···O3	0.929	2.450	2.717	96.52	C–H···O
C52–H52a···O6	0.960	2.903	3.352	109.77	C–H···O
C52–H52c···O6	0.960	3.033	3.352	101.04	C–H···O
C62–H62c···O6	0.960	2.767	3.327	117.94	C–H···O
C5–H5···O6	0.930	2.408	2.696	97.77	C–H···O

APPENDIX C

GLOSSARY

exciton: an electron-hole pair which can be tightly coupled and residing in a confined portion of space (Frenkel exciton) or can be delocalized over larger regions (Wannier-Mott exciton)

cytochrome: any of a group of proteins, each with an iron-containing heme group, that form part of the electron transport chain in mitochondria and chloroplasts. Electrons are transferred by reversible changes in the iron atom between the reduced iron(II) and oxidized iron(III) states.

cytochrome P450: the generic name applied to a large superfamily of hemoprotein, mixed-function oxidase that metobolize a structurally diverse group of exogenous and endogenous organic substrates. The name is derived from the prominent absorption band observed at 450 nm following reduction of the heme iron and its coordination with carbon monoxide.

delocalized bonding: the term is used to describe a system wherein the π bonds encompass more than two atoms

F_{430}: a yellow, nonfluorescent compound present in methanogenic bacteria, the factor contains nickel porphinoid present in all methanogenic bacteria. It is a component of methyl-coenzyme M methylreductase of *Methanobacterium thermoautotrophicum*, named factor 430 (F_{430}) because of an absorption maximum at 430 nm.

heme (haem): an iron-containing molecule that binds with proteins as a cofactor or prosthetic group to form the hemoproteins. These are hemoglobin, myoglobin, and the cytochromes. Essentially, heme comprises a porphyrin with its four nitrogen atoms holding the iron(II) atom as a chelate. This iron can reversibly bind oxygen (as in hemoglobin and myoglobin) or (as in the cytochromes) conduct electrons by conversion between the iron(II) and iron(III) series.

heme proteins: proteins that contains prosthetic groups based on iron protopoprhyrin IX or a few closely related macrocycles

peroxidase: an enzyme that catalyzes the oxidation of an organic or inorganic substrate by hydrogen peroxide

supramolecular: referring to a discrete entity containing two or more molecules/ions associated by intermolecular forces (such as hydrogen bonding, coordination chemistry, and electrostatic interactions) in a specific geometric arrangement)

CURRICULUM VITAE

RATCHADAPORN PUNTHAROD

BORN: 20 July 1975, Lampang, Thailand

CITIZENSHIP: Thai

MARITAL STATUS: Single

EDUCATION:

Ph.D. Student, Suranaree University of Technology, Nakhon Ratchasima, Thailand (Dec 2004–Mar 2009), M. Sc., Chemistry, Chiangmai University (Jun 2001–Mar 2004), and B. Sc., Chemistry, Chiangmai University, Chiangmai Thailand (Jun 1997–Mar 2001).

RELEVANT EXPERIENCE:

Research at Biospectroscopy Center, Monash University (Oct 2006–Oct 2007 and May–July 2008) and Synchrotron-FTIR, Hsinchu Science Park, Taiwan (9 Nov–11 Nov 2007).

PUBLICATIONS AND CONFERENCE PROCEEDINGS:

1. **Acta Cryst.** (2008). A64, C457. 2. Proceeding on 34th Congress on Science and Technology of Thailand 2008. 3. Proceeding on 33rd Congress on Science and Technology of Thailand 2007. 4. Proceeding of 1 st SUT Graduate Conference 2007. 5. **Acta Cryst.** (2005). A61, C306.

SCHOLARSHIP:

The Office of the Commission of Higher Education, Thailand (2005–2008).